Can tidal evolution lead to close-in planetary bodies around white dwarfs II: volcanism and transits

Yuqi Li,[1]★ Amy Bonsor,[1] and Oliver Shorttle[1,2]
[1]Institute of Astronomy, University of Cambridge, Madingley Road, Cambridge, CB3 0HA, UK
[2]Department of Earth Sciences, University of Cambridge, Downing Street, Cambridge, CB2 3EQ, UK

arXiv:2506.20316v1 [astro-ph.EP] 25 Jun 2025

Accepted XXX. Received YYY; in original form ZZZ

ABSTRACT

Planetary material accreted by white dwarfs provides unique insights regarding exoplanetary composition. The evolutionary pathways of planetary bodies around white dwarfs are crucial to understanding the presence of close-in planetary material, observed in the form of pollutants in the atmospheres of white dwarfs and planetary material transiting white dwarfs. Periodic transits around white dwarfs potentially reveal the existence of close-in planetary bodies undergoing dust production. Tidal interactions can bring planetesimals that have been gravitationally perturbed onto long-period highly eccentric orbits around white dwarfs towards shorter orbital periods and smaller eccentricities. Tidal interactions may also induce melting and volcanism in these planetesimals, potentially being a mechanism for dust production, the result of which may be seen in transit. Tidally induced volcanism may be triggered in a wide parameter space: for a 100 km-sized rocky planetesimals perturbed to a pericentre distance $\lesssim 0.01$ AU ($\gtrsim$ twice its Roche limit), both on long-period (~ 100 day) highly eccentric orbits and short-period (~ 10 hr) near circular orbits. We comment on the potential link between the resultant volcanic ejecta and observed optical transits.

Key words: white dwarfs – planets and satellites: general – planets and satellites: dynamical evolution and stability – planet–star interactions

1 INTRODUCTION

Around 10%–50% of white dwarfs are contaminated with planetary material (Zuckerman et al. 2003, 2010; Koester et al. 2014; Wilson et al. 2019; O'Brien et al. 2023, 2024; Manser et al. 2024), revealing the existence of close-in planetary bodies and offering insight into the composition of these bodies..

The leading theory of the accretion planetary material onto the white dwarf is tidal disruption of gravitationally perturbed planetesimals. As the host star loses a large fraction of its mass towards the white dwarf phase, the planetary system orbiting the host star becomes less gravitationally stable due to the weakening gravitational attraction from the host star and hence an expanding gravitationally instability zone around planetary bodies (Veras 2016). Planetary bodies that are initially stable may begin to alter each other's orbits via mechanisms such as scattering, mean motion resonances and secular chaos (Bonsor & Wyatt 2012; Bonsor et al. 2012; Mustill et al. 2018; O'Connor et al. 2022; Veras et al. 2023; Rodet & Lai 2024). During (potentially successive) perturbations, some of the planetary bodies are ejected to the outer planetary system and some of them enter the Roche limit, where they are stripped by differential tidal force (Veras et al. 2014). After tidal disruption, the planetary debris can be accreted onto the white dwarf under various mechanisms, for instance, Poynting-Robertson (PR) effect, gas drag, and the Yarkovsky effect (Rafikov 2011a,b; Bochkarev & Rafikov 2011; Metzger et al. 2012; Veras et al. 2015; Veras 2020; Malamud et al. 2021; Veras et al. 2022).

Accretion can be observed indirectly, through dusty material (infrared excess) and gas (circumstellar emission features) around the white dwarf (Zuckerman & Becklin 1987; Becklin et al. 2005; Kilic et al. 2005, 2006; Gänsicke et al. 2007; Jura et al. 2007; Farihi et al. 2009; Jura et al. 2009; Farihi et al. 2010; Melis et al. 2010; Xu et al. 2015; Farihi 2016; Bonsor et al. 2017; Xu et al. 2020; Lai et al. 2021; Wang et al. 2023; Rogers et al. 2024).

On the other hand, there is a growing number of systems with planetary materials occultating white dwarfs being detected (Guidry et al. 2021), some of which reveal periodicity in the light curves:

- the 4.5 hour periodic signals around white dwarf WD 1145+017 (Vanderburg et al. 2015),
- the 107.2 day period around ZTF J0139+5245 (Vanderbosch et al. 2020),
- the 9.937 hr and 11.2 hr periods around ZTF J0328-1219 (Vanderbosch et al. 2021),
- the 25.02 hr period around WD 1054-226 (Farihi et al. 2022).

The transiting features of the most well-studied system WD 1145+017 are summarized below (Vanderburg et al. 2015; Gänsicke et al. 2016; Rappaport et al. 2016; Croll et al. 2017; Gary et al. 2017):

- Long-lasting primary periodic signal ~ 4.5 hr.
- Shorter-lived secondary periodic signals (4.490–4.495 hr) near the primary.

★ E-mail: yl817@cam.ac.uk

© 2025 The Authors

- Variable wavelength-independent transit depths, up to ~ 60%.
- Asymmetric and noisy transit light curves.
- Longer transit duration (~ 5 min) relative to that of an intact planetesimal-sized body.

These features are consistent with a disintegrating body (due to, e.g., sublimation, partial tidal disruption) transiting the white dwarf (Kawahara et al. 2013; van Lieshout et al. 2014; Rappaport et al. 2014; Sanchis-Ojeda et al. 2015; Vanderburg et al. 2015; van Lieshout et al. 2016; Rappaport et al. 2016; Veras et al. 2017; Duvvuri et al. 2020). A potential orbital evolution pathway of such a close-in body could be tidal evolution (Veras et al. 2019; Veras & Fuller 2019, 2020; O'Connor & Lai 2020).

The classical view of tidal interaction is that differential tidal force exerted by the primary raises tidal bulges on the secondary (and vice versa). The tidal bulges lag behind the equipotential surface due to internal friction, perturbing the orbital evolution of the system (Hut 1981; Levrard et al. 2007; Leconte et al. 2010; Matsumura et al. 2010; Bolmont et al. 2011; Heller et al. 2011; Beaugé & Nesvorný 2012; Hansen 2012; Glanz et al. 2022; Rozner et al. 2022; Lu et al. 2023).

Tidal evolution is usually accompanied with dissipation of orbital energy as heat, which is referred to as tidal heating. Tidal heating is a plausible cause for the active volcanism on Io in the Solar System (McEwen et al. 1998; Rathbun et al. 2002; Spencer et al. 2007; Lopes & Williams 2015; Tyler et al. 2015; Rathbun et al. 2018; Kervazo et al. 2022; Davies et al. 2024; Seligman et al. 2024), and is a potential explanation for the formation of hot/inflated Jupiters (Miller et al. 2009; Ibgui et al. 2010; Leconte et al. 2010; Dong et al. 2021; Rozner et al. 2022; Glanz et al. 2022; Vick et al. 2023). Meanwhile, Seligman et al. 2024 investigates the mechanism where runaway melting of exoplanetary bodies undergoing tidal heating can trigger volcanism. Considering the enormous amount of orbital energy dissipated during the evolution process of a planetesimal perturbed onto highly eccentric orbits and subsequently circularized onto a close-in orbit around white dwarfs, it is reasonable to question whether tidal circularization of planetesimals around white dwarfs is accompanied with active volcanism.

In our paper I (Li et al. 2025), we model the orbital period of planetesimals undergoing tidal evolution around white dwarfs, showing that the resultant orbital period distribution will peak at short-period (nearly) circularized orbits (~ 10 hour–1 day), with a rising tail towards long-period highly eccentric orbits (~ 100 day) and a probability valley in-between.

In this paper, we qualitatively investigate a scenario where planetesimals barely perturbed outside the Roche limit undergo rapid tidal evolution, shrinking their orbital semi-major axis and eccentricity. The orbital decay is accompanied by tidal heating that triggers melting and volcanism. Dust ejected from volcanically active planetesimals is initially sufficiently opaque to block the observed star light and leads to transits seen in the optical. Similar to the disk formed under tidal disruption, volcanic dust can be accreted by the white dwarf (e.g., under PR drag). In exploring this model, this paper::

- predicts the planetesimals and their orbital parameters where tidally induced volcanism could be active;
- compares predictions for the features of transits originating from tidally induced volcanism to observations, focusing on the range of secondary drift periods, transit duration, transit depth and phase shift;
- compares the frequency of tidally induced volcanism and its contributions to white dwarf pollutants to those of tidal disruption.

The paper starts by summarizing the model for tidal heating (Section 2.1) and the conditions required for volcanism (Section 2.2.1). By predicting the ejection speed for volcanic ejecta (Section 2.2.2), the subsequent orbit of volcanically ejected material is computed and used to predict features of the transits (Section 2.3). Our results highlight that which planetesimals are volcanically active and the epochs during their evolution when this activity occurs 3.1. The fate of the volcanic ejecta, focusing on the range of orbital periods and orbital inclinations, is presented in Section 3.2. We then discuss the limitations in our model in Section 4.1, including the tidal, thermal modeling (Section 4.1.1, Section 4.1.2), Section 4.1.3 and Section 4.1.4) and the orbital evolution of the ejecta (Section 4.1.5 and Section 4.1.6). In Section 4.2, we compare the model predictions to observations, focusing on WD 1145+017. Finally, we discuss other potential transit-related scenarios accompanied with tidally induced volcanism in Section 4.3, together with other models proposed to explaining transits (Section 4.4) and in Section 5, we summarize our results.

2 METHOD

In this study, we qualitatively study a scenario in which volcanism is induced by tidal interactions after planetesimals are gravitationally perturbed onto highly eccentric orbits around the white dwarf. These planetesimals narrowly avoid tidal disruption, but experience strong tidal interactions. During tidal evolution, the orbital semi-major axis of the planetesimal decays, with the decaying orbital energy deposited as heat inside the planetesimal. Under intense tidal heating, the planetesimals may melt and undergo volcanism. The erupted volcanic dust blocks the white dwarf and leads to transit.

We present our model that is divided into two parts, 1. tidal evolution, volcanism of the planetesimal and 2. the subsequent orbit dispersion of the ejecta, in this section. For the planetesimal, we: 1. follow the orbital decay of the planetesimal under the constant time lag (CTL) model to obtain the accompanied tidal heating (Section 2.1), and 2. compare between heating and cooling of the planetesimal undergoing tidal evolution to deduce whether and for what parameters volcanism can be triggered and maintained (Section 2.2.1). For the volcanic ejecta, we estimate the ejection speed range (Section 2.2.2), from which we deduce the orbit dispersion of the ejecta relative to that of the planetesimal (Section 2.3).

The definitions of symbols and the corresponding fiducial values (if any) are listed in Table 1.

2.1 Tidal heating

As a planetesimal on a highly eccentric orbit around a white dwarf undergoes tidal evolution, its semi-major axis decays, and the damped orbital energy is deposited inside the body. The tidal energy deposition rate $\frac{dE_t}{dt}$ and semi-major axis decay rate ($\frac{da}{dt}$) are related by:

$$\frac{dE_t}{dt} = -\frac{GM_pM_*}{2a^2}\frac{da}{dt}, \tag{1}$$

where we neglect the rotational energy variations, which are orders of magnitude smaller than their counterparts of orbital energy, and we only consider the contributions from planetesimal tide induced by the white dwarf, which dominates the orbital evolution of the system. The inputs required for computing $\frac{da}{dt}$ are the properties of the white dwarf-planetesimal system (e.g., tidal response T_p in Table 1) and the initial orbit (initial pericentre q_0, initial apocentre Q_0).

Symbols	Definition	fiducial value
M_*	white dwarf mass	$0.6\,M_\odot$
R_*	white dwarf radius	$0.01\,R_\odot$
L_*	white dwarf luminosity	
t_0	cooling age of the white dwarf at the start of tidal evolution	100 Myr
M_p	planetesimal mass	
R_p	planetesimal radius	100 km
ρ_p	planetesimal bulk density	$3000\,\mathrm{kg/m^3}$
k_2	potential love number of degree 2	
Δt	constant time lag	
K_p	$K_p = 3k_2\Delta t$	1000 s
T_p	$T_p = \frac{K_p(M_p+M_*)M_*R_p^5}{M_p} \approx \frac{K_p M_*^2 R_p^5}{M_p}$	
I	moment of inertia	
σ_+	ultimate tensile strength	0.1 MPa
C_p	$C_p = \frac{I}{M_p R_p^2}$	$\frac{2}{5}$
t	tidal evolution time	
e	eccentricity	
a	semi-major axis	
q	pericentre distance	
q_0	initial pericentre distance	
Q	apocentre distance	
Q_0	initial apocentre distance	3 AU
r	radial distance from the host star	
r_{Roche}	Roche limit	
τ	orbital period	
ω_p	planetesimal spin	
$\bar{v}_{orb}$	orbital velocity	
v_k	local keplerian speed of circular orbit	
n	mean motion, $n = \sqrt{\frac{G(M_p+M_*)}{a^3}} \approx \sqrt{\frac{GM_*}{a^3}}$	
J	specific orbital angular momentum	
ϵ	specific orbital energy	
f	true anomaly	
E	eccentric anomaly	
γ	angle between velocity and radial vector	
ω	argument of pericentre	
c_p	planetesimal specific heat capacity	$1000\,\mathrm{J/(K\cdot kg)}$
κ	thermal conductivity	$3\,\mathrm{W/(m\cdot K)}$
α_d	thermal diffusivity	
f_m	radial position of magma reservoir in the unit of R_p	0.9
ϵ_e	emissivity	1
A_B	albedo	0
Nu	Nusselt number	1
E_t	tidal energy	
T	Temperature	
T_s	(time-averaged) equilibrium surface temperature	
T_c	critical temperature of melting	2000 K
ΔT_c	temperature representation of melting energy	3000 K
Q_l	heat loss	
n_0	mass fraction of volcanic gas	
μ_m	mean molecular weight	
$\bar{u}_{eject}$	volcanic ejection velocity	
$\bar{v}_{tot}$	total velocity of ejecta	
v_{esc}	escape speed	
θ	polar angle	
ϕ	azimuthal angle	

Table 1. Definitions of the symbols and the choice of fiducial values. $M_* = 0.6\,M_\odot$ is the peak of the observed white dwarf mass distribution (Kepler et al. 2007; Tremblay et al. 2016; Kepler et al. 2017). t_0 quantifies the time taken to perturb planetesimals onto highly eccentric orbits (Mustill et al. 2018). c_p and κ are identical to those in Ricard et al. 2009; Lichtenberg et al. 2021. T_c is chosen to be the silicates liquidus temperature (Scheinberg et al. 2015; Johansen et al. 2023). σ_+ is chosen to be the lower bound for meteorites samples (Pohl & Britt 2020). K_p is converted from tidal dissipation for typical rocky bodies (Lambeck 1977; Neron de Surgy & Laskar 1997; Bolmont et al. 2011; Noyelles et al. 2014; Clausen & Tilgner 2015; Barnes 2017; Rufu & Canup 2020; Bolmont et al. 2020; Sánchez et al. 2020; Bagheri et al. 2022).

To obtain the tidal heating rate $\frac{dE_t}{dt}$, the key is to compute the orbital evolution rate of the planetesimal. Under the CTL model, where the planetesimal around the white dwarf reaches pseudo-synchronization and spin-orbit alignment rapidly and that the orbital angular momentum is conserved during tidal evolution, the coupled tidal evolutionary equations can be reduced to those regarding semi-major axis ($\frac{da}{dt}$) and eccentricity ($\frac{de}{dt}$) (Hut 1981; Levrard et al. 2007; Leconte et al. 2010; Matsumura et al. 2010; Bolmont et al. 2011; Heller et al. 2011; Beaugé & Nesvorný 2012; Hansen 2012; Glanz et al. 2022; Rozner et al. 2022; Lu et al. 2023):

$$\frac{da}{dt} = -7GT_p\left(\frac{2q_0Q_0}{q_0+Q_0}\right)^{-7} e^2(1-e^2)^{-\frac{1}{2}}F(e). \tag{2}$$

$$\frac{de}{dt} = -\frac{7}{2}GT_p\left(\frac{2q_0Q_0}{q_0+Q_0}\right)^{-8} e(1-e^2)^{\frac{3}{2}}F(e), \tag{3}$$

where T_p is a white dwarf-planetesimal system relevant constant (see Table 1) modulating the tidal evolution rate, $F(e)$ is:

$$F(e) = \frac{1+\frac{45}{14}e^2+8e^4+\frac{685}{224}e^6+\frac{255}{448}e^8+\frac{25}{1792}e^{10}}{1+3e^2+\frac{3}{8}e^4}. \tag{4}$$

We can further eliminate the terms regarding semi-major axis a using conservation of orbital angular momentum:

$$a(1-e^2) = \frac{2q_0Q_0}{q_0+Q_0}, \tag{5}$$

such that $\frac{dE_t}{dt}$ (Eq.1) under the CTL model can be reduced to an equation of single variable, eccentricity e:

$$\frac{dE_t}{dt} = -GM_pM_*e\left(\frac{2q_0Q_0}{q_0+Q_0}\right)^{-1}\frac{de}{dt}, \tag{6}$$

whose maximum is at $e \approx 0.735$ whose presence is a natural consequence of the competition between the increase in the term $\frac{1}{a^2}$ and the decrease in the term $\left|\frac{da}{dt}\right|$ during tidal evolution in Eq.1.

Eq.2 and Eq.6 indicate that a planetesimal starting at a smaller q_0 evolves much faster, and hence, is heated up much more rapidly under the CTL model. However, a planetesimal undergoing long term tidal evolution and volcanic activities must avoid tidal disruption, setting the minimum pericentre distance a planetesimal can reach–the Roche limit (r_{Roche}). Under tidal interactions, r_{Roche} for a pseudo-synchronously rotating planetesimal that is spherical and rigid in the limit of $r_{Roche} \ll Q_0$ can be approximated as (Li et al. 2025):

$$r_{Roche} \approx \left(\frac{3.36125GM_*}{\frac{4}{3}\pi G\rho_p + \frac{3\sigma_+}{4\rho_pR_p^2}}\right)^{\frac{1}{3}}. \tag{7}$$

2.2 Volcanism

With the tidal heating rate quantified, in this section, we propose two simple criteria for volcanism (Section 2.2.1) and estimate the possible range of volcanic ejection speed (Section 2.2.2).

2.2.1 *Conditions for volcanism*

Based on the tidal evolution track and the accompanied tidal heating, we investigate whether and under what conditions volcanism can be triggered and maintained. We acknowledge that accurate modeling of tidal heating and volcanism is nontrivial and requires proper coupling among tidal, thermal and rheological evolution (see Section 4.1). However, for the purpose of qualitative study, we incorporate two simple conditions for volcanism:

- melting happening faster than cooling (initiation),
- heating rate being faster than cooling rate (maintenance).

We quantitatively investigate the first condition (initiation) by comparing the time taken for melting (t_{melt}) to the time taken for cooling (t_{cool}) at the start of tidal evolution, $t = 0$. The melting timescale, t_{melt}, is given by:

$$t_{melt} \sim \frac{c_pM_p\Delta T_c}{\dot{E}_{t,0}}, \tag{8}$$

where we use the fact that for a highly eccentric orbit, $\frac{dE_t}{dt}(t = t_{melt}) \approx \frac{dE_t}{dt}(t = 0)$ (see Appendix A). The energy required for melting is given by the multiplication of specific heat capacity (c_p), planetesimal mass (M_p) and an temperature representation of melting energy (ΔT_c), $c_pM_p\Delta T_c$. We choose $\Delta T_c = 3000$ K as the fiducial value (see Appendix B).

The cooling timescale, t_{cool}, is approximated by the diffusion timescale scaled by the Nusselt number (Nu ≥ 1), the ratio of total heat loss rate (excluding heat loss due to volcanism) to conductive heat loss rate:

$$t_{cool} \sim \frac{R_p^2\rho_pc_p}{\pi^2\kappa\mathrm{Nu}}, \tag{9}$$

with κ the thermal conductivity. In this study, we focus on the limiting case where heat loss only occurs via conduction as a planetesimal undergoing tidally induced volcanism should usually preserve a solid mantle (see Section 4.1.2) where conduction is the dominant heat transport mechanism (Nu = 1; an estimation of Nu for convection through a solid-like crust with melt is presented in Appendix C, where we show that Nu $\lesssim 10$ usually holds).

The ratio of melting timescale to cooling timescale, $\frac{t_{melt}}{t_{cool}}$, can be approximated as (see Appendix A):

$$\frac{t_{melt}}{t_{cool}} \sim 0.5\mathrm{Nu}\frac{1000\,\mathrm{s}}{K_p}\frac{\kappa}{3\,\mathrm{W/(m\cdot K)}}\frac{\Delta T_c}{3000\,\mathrm{K}} \times\left(\frac{0.6\,M_\odot}{M_*}\right)^3\left(\frac{100\,\mathrm{km}}{R_p}\right)^4\left(\frac{q_0}{0.01\,\mathrm{AU}}\right)^{7.5}\left(\frac{Q_0}{3\,\mathrm{AU}}\right)^{1.5}. \tag{10}$$

We assume that melting occurs for $\frac{t_{melt}}{t_{cool}} < 1$ (melting being faster than cooling), with the critical parameters determined by the boundary $\frac{t_{melt}}{t_{cool}} = 1$. Most importantly, due to the rapid decay of tidal heating rate with the increase in the initial pericentre distance q_0 (see Section 2.1), the critical initial peicentre distance above which melting is slower than cooling ($q_{0,crit}$) is:

$$q_{0,crit} \sim 0.011\,\mathrm{AU} \times\left(\frac{1}{\mathrm{Nu}}\frac{K_p}{1000\,\mathrm{s}}\frac{3\,\mathrm{W/(m\cdot K)}}{\kappa}\frac{3000\,\mathrm{K}}{\Delta T_c}\right)^{\frac{2}{15}} \times\left(\frac{M_*}{M_\odot}\right)^{\frac{2}{5}}\left(\frac{R_p}{100\,\mathrm{km}}\right)^{\frac{8}{15}}\left(\frac{3\,\mathrm{AU}}{Q_0}\right)^{\frac{1}{5}}. \tag{11}$$

The strong dependence of tidal heating rate on q_0 indicates that for a fixed characteristic cooling time, a small decrease in q_0 will move from a regime where heating and cooling are comparable to heating dominant regime, making the details of cooling model less important (see Appendix D for alternative models with consistent results).

To quantify the second condition (maintenance), we compare the heat loss rate $\dot{Q}_l$ to the tidal power $\dot{E}_t$. $\dot{Q}_l$ is approximated as heat loss via steady-state conduction scaled by the Nusselt number Nu′ (see Appendix E):

$$\dot{Q}_l = 4\pi\kappa \mathrm{Nu}' \frac{f_m}{1-f_m} R_p (T_c - T_s), \tag{12}$$

where f_m is the position of the melt reservoir in the unit of planetesimal size (above which conduction is the dominant heat transport mechanism). We apply a fiducial value of 0.9 when necessary, while keeping it a free parameter in equations, considering the large uncertainties (see Appendix F). We use Nu′ as a reminder that heat loss after melting quantified by Nu′ is not necessarily the same as its counterpart during melting, quantified by Nu in Eq.10. Similar to the melting process, we consider the limiting case where $\mathrm{Nu}' = 1$. $T(x = f_m R_p) = T_c$ is the critical temperature of melting, $T(x = R_p) = T_s$ is the time-averaged surface temperature of the planetesimal given by (Quirrenbach 2022):

$$T_s = \left[\frac{L_*(1-A_B)}{16\pi\epsilon_e\sigma a^2}\right]^{\frac{1}{4}} \frac{2\sqrt{1+e}}{\pi} E_2\left(\frac{2e}{1+e}\right), \tag{13}$$

where E_2 is the complete elliptic integral of the second kind, and $E_2\left(\frac{2e}{1+e}\right) \to 1$, $T_s \to \frac{2\sqrt{2}}{\pi}\left[\frac{L_*(1-A_B)}{16\pi\epsilon\sigma a^2}\right]^{\frac{1}{4}}$ as $e \to 1$.

T_s is a function of white dwarf luminosity, which we will approximate as (Mestel 1952):

$$L_*(t) \approx 3.26 L_\odot \frac{M_*}{0.6 M_\odot}\left(0.1 + \frac{t_0 + t}{\mathrm{Myr}}\right)^{-1.18}, \tag{14}$$

where t_0 is the cooling age of the white dwarf at the start of tidal evolution ($t = 0$).

Similarly, by setting the ratio of tidal power to heat loss rate $\frac{\dot{E}_t}{\dot{Q}_l} = 1$, one can constrain the parameter space where tidal power exceeds heat loss of cooling and hence volcanism can occur. A conservative estimation (due to the initially increasing tidal power along the tidal evolution track) for the critical initial pericentre distance below which melting can be maintained $q'_{0,crit}$ is (see Appendix E):

$$\begin{aligned} q'_{0,crit} &\sim 0.014\,\mathrm{AU} \\ &\times \left(\frac{1}{\mathrm{Nu}'}\frac{K_p}{1000\,\mathrm{s}}\frac{3\,\mathrm{W/(m\cdot K)}}{\kappa}\frac{2000\,\mathrm{K}}{T_c}\frac{1-f_m}{f_m}\right)^{\frac{2}{15}} \\ &\times \left(\frac{M_*}{0.6\,M_\odot}\right)^{\frac{2}{5}}\left(\frac{R_p}{100\,\mathrm{km}}\right)^{\frac{8}{15}}\left(\frac{3\,\mathrm{AU}}{Q_0}\right)^{\frac{1}{5}} \\ &\sim 1.2 q_{0,crit}\left(\frac{\mathrm{Nu}}{\mathrm{Nu}'}\frac{1-f_m}{f_m}\frac{\Delta T_c}{T_c}\right)^{\frac{2}{15}}, \end{aligned} \tag{15}$$

where we use the fact that $(T_c - T_{s,0})^{-\frac{2}{15}} \approx T_c^{-\frac{2}{15}}$ usually applies ($T_{s,0} \approx T_s(a = \frac{Q_0}{2}, e = 1)$). Meanwhile, there is no simple scaling relation when $T_s(t)$ is non-negligible due to its dependence on other free parameters (for instance, q_0 and e). However, one can obtain the corresponding upper/lower bounds of the critical values (which is a conservative estimation of the parameter space) by using the inequality $T_c > T_c - T_s$. For instance, the upper bound of the critical eccentricity below which volcanism can no longer be maintained is (see Appendix E):

$$\begin{aligned} e'_{crit} &\lesssim 0.001 \\ &\times \left(\mathrm{Nu}'\frac{1000\,\mathrm{s}}{K_p}\frac{\kappa}{3\,\mathrm{W/(m\cdot K)}}\frac{T_c}{2000\,\mathrm{K}}\frac{f_m}{1-f_m}\right)^{\frac{1}{2}} \\ &\times \left(\frac{M_\odot}{M_*}\right)^{\frac{3}{2}}\left(\frac{100\,\mathrm{km}}{R_p}\right)^{2}\left(\frac{q_0}{0.005\,\mathrm{AU}}\right)^{\frac{9}{2}}. \end{aligned} \tag{16}$$

2.2.2 *Volcanic ejection speed*

In the tidally induced volcanism scenario we consider in this study, the volcanic ejecta is considered to cause the transits. To understand whether the transit features originate from tidally induced volcanism, one needs to know the orbit of the ejecta, which is dependent on the ejection velocity. We approximate the volcanic ejection speed ($u_{ejection}$) using the conduit model (Woods & Bower 1995; Colucci et al. 2014; Macedonio et al. 2005) as (see Appendix G):

$$u_{eject} \sim \sqrt{n_0 RT} \approx 3000\sqrt{\frac{n_0}{\mu_m}\frac{T}{1000\,\mathrm{K}}}\,\mathrm{m/s}, \tag{17}$$

where n_0 is the mass fraction of gas in the flow with specific gas constant R and mean molecular wright μ_m, T is the temperature of flow. When substituting $n_0 \sim 0.01$–0.1 (Woods & Bower 1995), $\mu \sim 10$ (typical rocky planet volcanic gas Renggli et al. 2017; Liggins et al. 2023) and $T \sim 1000\,\mathrm{K}$ (critical temperature of melting Lesher & Spera 2015; Scheinberg et al. 2015; Johansen et al. 2023), u_{eject} is of the order of magnitude 100 m/s, broadly consistent with the numerical simulations in Woods & Bower 1995; Macedonio et al. 2005; Colucci et al. 2014 and the observations (Steinberg & Babenko 1978; Geissler et al. 1999). Accounting for the uncertainties in the analytical model and free parameters, we choose $u_{ejection} = 10\,\mathrm{m/s}$–$1000\,\mathrm{m/s}$, with the upper limit matching the observations of Io's volcanism (McEwen & Soderblom 1983; Lopes & Williams 2015).

2.3 Orbit dispersion of volcanic ejecta

Volcanically active planetesimals spew out dust and gas. If sufficient dust is ejected, it will initially be opaque and produce optical transits of the white dwarf. The subsequent orbits of the ejecta after ejection is, thus, crucial to the predicted features of the transits, including dispersion in orbital periods, as well as transit depth and duration.

In this section, we focus solely on the dust ejected and leaving the planetesimal (ejection speed greater than escape speed of the planetesimal $u_{eject} > v_{esc}$), assuming that initially the dust evolves purely dynamically and dominated by the gravity of the white dwarf, with an initial velocity kick induced as it is released. We note here that this ignores other processes that may be important, including mutual interactions, gravitational perturbations due to the planetesimal, radiation and magnetic forces (see Section 4.1.5).

In this section, we outline a method to compute the orbital parameters of the ejecta as a function of the orbit of the planetesimal, where the ejecta is launched on the surface of the planetesimal, and the ejection velocity. The assumption is that when dust leaves the planetesimal its future trajectory is only influenced by the gravity of the star, such that its initial conditions determine its trajectory, which

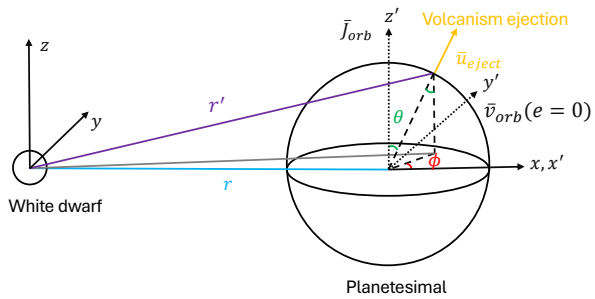

Figure 1. The coordinate system used to solve for the final orbit of the ejecta. The sketch is not to scale.

deviates from the planetesimal's orbit. We also neglect the back reaction of volcanic ejection on the planetesimal's orbit (see Appendix I).

2.3.1 *Computations of orbital parameters of the ejecta*

First, based on the variation of specific energy, we compute the variation of orbital semi-major axis/period of the ejecta relative to the planetesimal. In the heliocentric frame of the white dwarf, the specific energy of the planetesimal is given by:

$$\epsilon_p = -\frac{GM_*}{2a} = -\frac{GM_*}{r} + \frac{1}{2}v_{orb}^2, \tag{18}$$

while the specific energy of the ejecta is:

$$\epsilon' = -\frac{GM_*}{2a'} = -\frac{GM_*}{r'} - \frac{GM_p}{R_p} + \frac{1}{2}{v_{tot}}^2, \tag{19}$$

where $v_{orb} = \sqrt{GM_*\left(\frac{2}{r} - \frac{1}{a}\right)}$ is the orbital speed of the planetesimal with an orbital semi-major axis a at distance r from the white dwarf, r' is the distance between the ejecta at eruption to the white dwarf and v_{tot} is the total speed of the ejecta (a combination of orbital velocity, spin velocity and ejection velocity).

The relation between the semi-major axis of the ejecta a' and its counterpart of the planetesimal a is hence:

$$\begin{aligned}\frac{1}{a'} &= \frac{1}{a} - 2\left(\frac{1}{r} - \frac{1}{r'}\right) + \frac{2M_p}{M_* R_p} - \frac{v_{tot}^2 - v_{orb}^2}{GM_*} \\ &= \frac{2}{r'} + \frac{2M_p}{M_* R_p} - \frac{v_{tot}^2}{GM_*}.\end{aligned} \tag{20}$$

To solve for a', we define a heliocentric Cartesian coordinate system where (see Fig.1):

- the x-axis aligns with the radial vector from the white dwarf to the planetesimal,
- the y-axis aligns with the velocity vector the planetesimal would have if it is on a circular orbit,
- the z-axis aligns with the orbital angular momentum vector of the planetesimal,

We further define a spherical polar coordinate system centred at the planetesimal with respect to a new Cartesian coordinate system (x', y', z'), obtained by shifting the origin of the Cartesian coordinate (x, y, z) defined above to $(r, 0, 0)$ (such that $x' = x - r$, $y' = y$, $z' = z$). We use the polar angle θ and azimuthal angle ϕ to define the position/direction of volcanic ejection where (see Fig.1):

- θ is the polar angle from the z' axis to the ejecta,
- ϕ is the azimuthal angle from the x' axis to the ejecta's projection onto the x'–y' (orbital/equatorial) plane of the planetesimal.

Hence, the orbital velocity of the planetesimal is:

$$\bar{v}_{orb} = v_{orb}\begin{bmatrix}\cos\gamma \\ \sin\gamma \\ 0\end{bmatrix}, \tag{21}$$

with γ the angle between the radial vector from the white dwarf to the planetesimal and the velocity vector of the planetesimal such that $\sin\gamma = \sqrt{\frac{a^2(1-e^2)}{r(2a-r)}}$, $\cos\gamma = \sqrt{1-\sin^2\gamma}\,\frac{\sin f}{|\sin f|}$.

The velocity given to the ejected mass due to the spin of the planetesimal is:

$$\bar{v}_{spin} = \omega_p R_p \begin{bmatrix}-\sin\theta\sin\phi \\ \sin\theta\cos\phi \\ 0\end{bmatrix}, \tag{22}$$

where ω_p is the spin of the planetesimal, which is given by the pseudo-synchronous spin rate:

$$\omega_p = S\frac{1 + \frac{15}{2}e^2 + \frac{45}{8}e^4 + \frac{5}{16}e^6}{\left(1 + 3e^2 + \frac{3}{8}e^4\right)}\sqrt{GM_*}\left(\frac{2q_0Q_0}{q_0 + Q_0}\right)^{-\frac{3}{2}}, \tag{23}$$

with S quantifying the direction of the planetesimal's spin relative to its orbit, which is 1 for prograde orbits and -1 for retrograde orbits.

The ejection velocity, which is assumed to be parallel to the radial vector from the centre of the planetesimal to the position of ejection on the surface of the planetesimal is:

$$\bar{u}_{eject} = u_{eject}\begin{bmatrix}\sin\theta\cos\phi \\ \sin\theta\sin\phi \\ \cos\theta\end{bmatrix}, \tag{24}$$

where ϕ and θ are the azimuthal angle and polar angle quantifying the position of mass ejection on the surface of the planetesimal (where $\theta = \frac{\pi}{2}$ is the equator of the planetesimal/orbital plane, $\phi = 0$ aligns with the x-axis). The positional vector of the ejecta in the white dwarf frame $\bar{r}'$ is:

$$\bar{r}' = \begin{bmatrix}r + R_p\sin\theta\cos\phi \\ R_p\sin\theta\sin\phi \\ R_p\cos\theta\end{bmatrix}. \tag{25}$$

The velocity of the ejecta $\bar{v}_{tot} = \bar{v}_{orb} + \bar{v}_{spin} + \bar{u}_{eject}$ is:

$$\bar{v}_{tot} = \begin{bmatrix}v_{orb}\cos\gamma - \omega_p R_p\sin\theta\sin\phi + u_{eject}\sin\theta\cos\phi \\ v_{orb}\sin\gamma + \omega_p R_p\sin\theta\cos\phi + u_{eject}\sin\theta\sin\phi \\ u_{eject}\cos\theta\end{bmatrix}, \tag{26}$$

We can now solve for the orbital semi-major axis of the ejecta using Eq.20.

Second, based on the orbital angular momentum of the ejecta $\bar{J}' \approx \bar{r}' \times \bar{v}_{tot}$, one can solve for the orbital inclination i' of the ejecta:

$$i' = \arctan\left(\frac{\sqrt{J_x'^2 + J_y'^2}}{J_z'}\right)\frac{\cos\theta}{|\cos\theta|}, \tag{27}$$

where the last term $\frac{\cos\theta}{|\cos\theta|}$ defines the direction of the tilt.

Finally, we approximate the orbital eccentricity vector (whose magnitude is the eccentricity) of the ejecta via:

$$\bar{e}' = \frac{v_{tot}^2 \bar{r}' - (\bar{v}_{tot} \cdot \bar{r}')\bar{v}_{tot}}{GM_*} - \frac{\bar{r}'}{r'}. \tag{28}$$

2.3.2 *Near circular orbit approximations and extremes*

We show in our paper I that if the transits around WD 1145+017 (4.5 hr period) and ZTF J0328-1219 (9.937 hr and 11.2 hr period) originate from planetesimals undergoing tidal evolution, the planetesimals are most likely on near circular orbits. Furthermore, we show that tidal evolution may intrinsically lead to a pile-up of planetesimals on short-period near circular orbits, which together with a potentially higher transit probability, making them more likely to be identified by observations. These short-period planetesimals are also ideal targets for periodicity measurements (easier to constrain orbital periods using dedicated high-speed photometry) and dynamical studies (more constrained initial pericentre distance and tidal circularization timescale) (Li et al. 2025). Therefore, it is valuable to consider the special case where the transiting volcanically active planetesimal is on a near circular orbit (see Appendix H for generalization to moderately eccentric orbit).

In terms of the observations, we are mainly interested in the orbital period ($\Delta\tau$)/semi-major axis (Δa) dispersion and orbital plane dispersion (inclination i') of the ejecta relative to the planetesimal, which translate to the range of drift periods/transit duration and transit depth, respectively.

We note that $\Delta\tau$ and i' are effectively equal to their circular-orbit counterparts regardless of the true anomaly for a near circular orbit ($e \lesssim 0.01$) and it is reasonable to approximate the geometry as a circular orbit (see Appendix H).

The calculations of Δa and i' can be greatly simplified assuming $e \to 0$ by using the facts that:

- $\frac{v_{spin}}{v_{orb}} \ll 1$,
- $\frac{u_{eject}}{v_{orb}} \ll 1$
- $\frac{R_p}{a} \ll 1$,
- $\frac{2M_p a}{M_* R_p} = \frac{v_{esc}^2}{v_{orb}^2} < \frac{u_{eject}^2}{v_{orb}^2}$.

As a result, we may limit the calculations to the first-order terms in $\frac{v_{spin}}{v_{orb}}$, $\frac{u_{eject}}{v_{orb}}$ and $\frac{R_p}{a}$. Note that due to the multiplications with the trigonometry functions, the magnitude of the first-order terms can be reduced to that of their second-order counterparts for some θ and ϕ. We will neglect these second-order effects in the derivations.

The first order approximation for $\Delta a = a' - a$ is:

$$\frac{\Delta a}{a} \approx 2\sin\theta \left[(1+S)\frac{R_p}{a}\cos\phi + \frac{u_{eject}}{v_{orb}}\sin\phi\right]. \tag{29}$$

The corresponding orbital period dispersion of the ejecta relative to the orbital period of the planetesimal $\Delta\tau$ is:

$$\frac{\Delta\tau}{\tau} \approx \frac{3}{2}\frac{\Delta a}{a}. \tag{30}$$

Eq.29 approaches 0 (but not exactly 0 due to the higher-order contributions we neglect) at $\sin\theta = 0$ (poles). The extremes of $\frac{\Delta\tau}{\tau}$ present at $\theta = \frac{\pi}{2}$ (equator) and $\phi = \arctan\frac{\frac{u_{eject}}{v_{orb}}}{\frac{R_p}{a} + \frac{\omega_p R_p}{v_{orb}}} = \arctan\frac{u_{eject} a^{\frac{3}{2}}}{\sqrt{GM_*}(1+S)R_p}$, with the extremes being:

$$\frac{\Delta\tau_\pm}{\tau} \approx \pm 3\sqrt{\frac{u_{eject}^2}{v_{orb}^2} + (1+S)^2\frac{R_p^2}{a^2}}, \tag{31}$$

which gives the maximum period drift/maximum phase-shift rate of the ejecta relative to the planetesimal.

The first-order approximation for the orbital angular momentum of the ejecta $\bar{J}'$ is:

$$\begin{aligned}\bar{J}' \approx & -R_p v_{orb}\cos\theta\hat{i} - u_{eject} a\cos\theta\hat{j} \\ & + (a v_{orb} + \omega_p R_p a\sin\theta\cos\phi + a u_{eject}\sin\theta\sin\phi \\ & + R_p v_{orb}\sin\theta\cos\phi)\hat{k},\end{aligned} \tag{32}$$

from which one can approximate the tilt of the ejecta's orbital plane to the planetesimal's orbital plane, orbital inclination i' as:

$$i' \approx \cos\theta\sqrt{\frac{u_{eject}^2}{v_{orb}^2} + \frac{R_p^2}{a^2}}, \tag{33}$$

which approaches 0 at $\cos\theta = 0$ (equator) and whose extremes present at $\cos\theta = \pm 1$ (poles), with the extremes being:

$$i'_\pm \approx \pm\sqrt{\frac{u_{eject}^2}{v_{orb}^2} + \frac{R_p^2}{a^2}}, \tag{34}$$

which gives the maximum extent of the ejecta perpendicular to the orbital plane of the planetesimal.

Although there seems to be no dependence on planetesimal density in the equations, one should be cautious that the analytical model assumes that the ejecta is instantaneously unbound to the planetesimal/bound to the white dwarf such that the ejecta's orbit is torqued negligibly by the planetesimal (see Section 4.1.5 for the viability of this assumption). Therefore, the analytical model is expected to converge to the real case at higher ejection speed for a planetesimal with a higher density.

3 RESULTS

3.1 Is volcanism active?

This section determines whether or not planetesimals perturbed close to a white dwarf become volcanically active. We consider planetesimals sufficiently close to suffer strong tidal interactions, but insufficiently close to be tidally disrupted. Based on the model presented in Section 2.2.1, the initial pericentre, q_0 of the planetesimal is the key parameter.

First, in Fig.2 (all 3 panels have identical axes), we follow the tidal evolution tracks of planetesimals starting at a common apocentre distance (parameters listed in Table 1) and different pericentre distances ranging from 0.00456 AU (Roche limit) to 0.02 AU. Note that Fig.2 is a snapshot in parameter space where all the free parameters except for q_0 (the dominant factor) are fixed. Each sample planetesimal evolves horizontally across the figure (as is indicated by the arrow in the upper-left panel, representing the increase in time elapsed after the planetesimal arrives at q_0, t), decreasing orbital eccentricity (e,

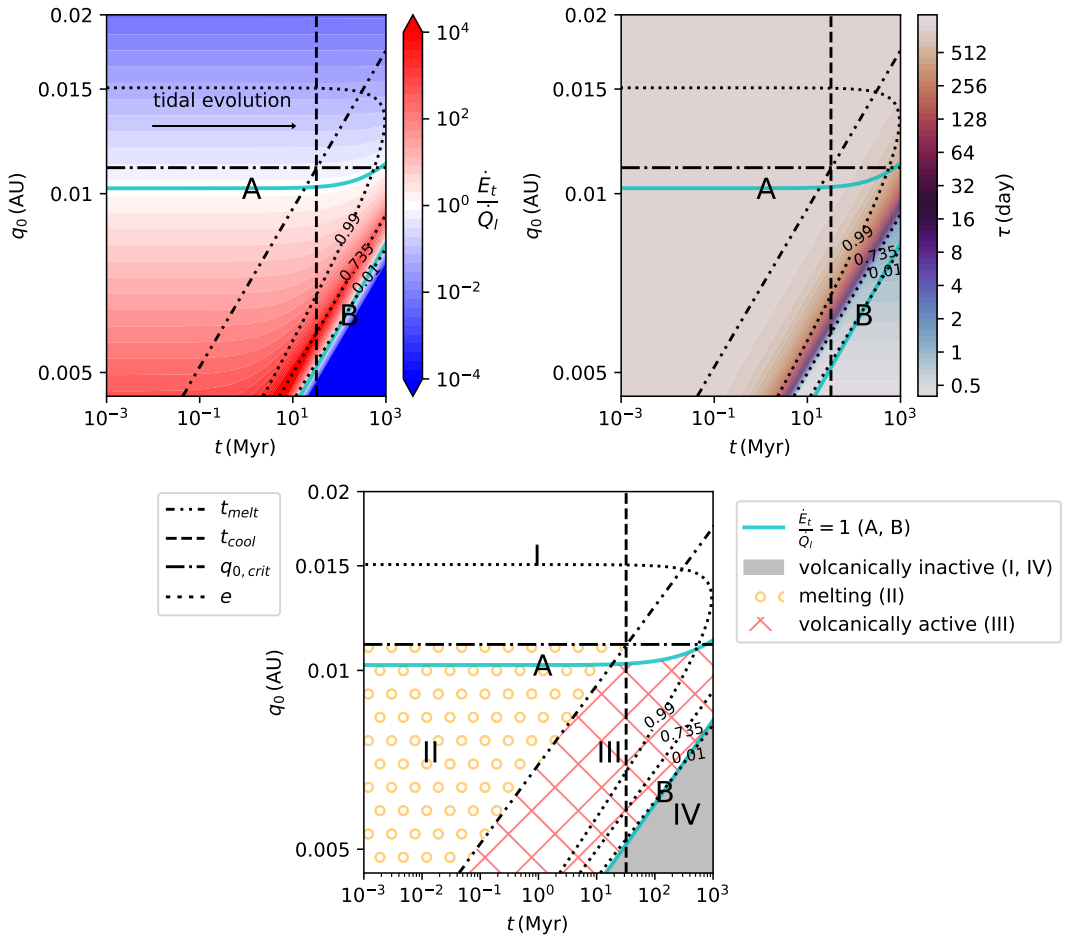

Figure 2. The contour plot of the ratio of tidal power to steady state heat loss rate (upper-left panel), orbital period (upper-right panel), and a highlight of which planetesimal (q_0) and when (t, e) are volcanically active (lower panel). The dashdotdotted, dashed and dashdot lines are the melting timescale, cooling timescale and the critical initial pericentre distance of melting. The dotted contour lines are the orbital eccentricities. Other free parameters are identical to those listed in Table 1.

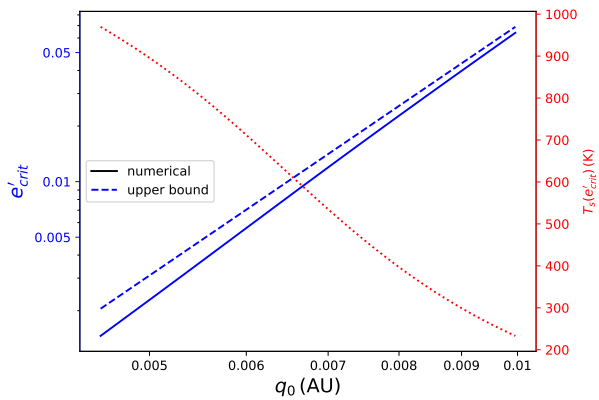

Figure 3. The critical eccentricity (e'_{crit}) below which volcanism cannot be maintained computed numerically (using Eq.6 and Eq.12, solid line, left axis) together with the time-averaged equilibrium temperature at $e = e'_{crit}$ (dotted line, right axis), and the analytical upper bound of $e = e'_{crit}$ (Eq.16, dashed line, left axis). The free parameters are identical to those in Table 1.

the dotted contour lines) and orbital period (τ, contours in the upper-right panel). Meanwhile, orbital energy is dissipated as heat inside the planetesimal, until the planetesimal's orbit circularizes, where tidal evolution ceases. Contours on the upper two panels plot the ratio of tidal power to cooling rate ($\frac{\dot{E}_t}{\dot{Q}_l}$, upper-left panel) and orbital period of the planetesimal (τ, upper-right panel). The lower panels highlight which planetesimal (q_0) undergoes active volcanism and when (t, e).

The physical meanings of the lines in Fig.2 are summarized below:

- Dashdotdotted line: melting time (t_{melt}), time required for melting from the start of tidal evolution.
- Dashed line: cooling time (t_{cool}), time required to transport the tidal energy outside the planetesimal.
- Dashdot line: the critical initial pericentre distance for melting ($q_{0,crit}$, Eq.11), where melting time is equal to the cooling time ($t_{melt} = t_{cool}$), above which the planetesimal cannot melt under tidal heating.
- Solid (cyan) line A: the contour line where tidal power equal to cooling rate at high e ($\frac{\dot{E}_t}{\dot{Q}_l} = 1$, high e), above which the melt cannot be maintained due to the rapidly decaying tidal evolution rate arising from large q_0. The intersection of A with the y-axis ($t = 0$) defines the critical initial pericentre distance for melt maintenance, below which tidal power exceeds cooling rate at $t = 0$, the start of tidal evolution ($q'_{0,crit}$, Eq.15).

- Solid (cyan) line B: the contour line where tidal power equal to cooling rate at low eccentricity ($\frac{\dot{E}_t}{\dot{Q}_l} = 1$, low e), below which the melt cannot be maintained due to the diminishing tidal heating rate when the planetesimal approaches tidal circularization state. An optimistic estimation of the orbital eccentricity along B, e'_{crit} is given by Eq.16.

The potential volcanically active regime is region III (cross-hatched) in the lower panel of Fig.2, spanning from long-period highly eccentric orbit to short-period near circular orbit. The physical processes in regions I–IV in the lower panel of Fig.2 are summarized below:

- I: volcanically inactive ($\tau \gtrsim 1$ yr, $e \sim 1$), above A ($\sim q'_{0,crit}$) or $q_{0,crit}$, whichever is lower, volcanism is inactive as the planetesimal is not close enough to the white dwarf for strong tidal interactions to induce/maintain melt.
- II: melting ($\tau \gtrsim 1$ yr, $e \sim 1$), bounded by $q_{0,crit} \sim 0.011$ AU and t_{melt}, the planetesimal potentially undergoes melting.
- III: volcanically active ($\tau \sim 10$ hour–1 yr, $e \sim 0.001$–1), bounded by A or $q_{0,crit}$, whichever is lower, t_{melt} and B, the planetesimal is potentially melted and volcanism is active.
- IV: volcanically inactive ($\tau \sim 10$ hour–1 day, $e \sim 0$–0.01), below B, volcanism is inactive due to the slowing down tidal heating being insufficient to keep the melt from crystallization as the planetesimal approaches tidal circularization.

In the remainder of this section, we take a detailed look at the conditions required for volcanism including the parameter dependence.

3.1.1 Conditions for melting

First, we investigate the conditions required for melting: melting being faster than cooling ($t_{melt} < t_{cool}$). In Fig.2, melting is considered possible if a horizontal line representing the time evolution of a planetesimal intersects the solid line t_{melt} before it intersects the dashed line t_{cool}. Due to the rapidly decreasing tidal evolution rate with q_0, t_{melt} increases rapidly with q_0 ($t_{melt} \propto q_0^{7.5}$), such that a planetesimal starting at a larger q_0 melts much slower. The maximum q_0 where melting is possible is given by the q_0 where $t_{melt} = t_{cool}$, which is represented by the dashdot line. The numerically computed $q_{0,crit} \approx 0.011$ AU is in agreement with its analytical counterpart Eq.11. Based on Eq.11 and setting $q_{0,crit}$ equal to the Roche limit ($r_{Roche} = 0.00456$ AU) where the planetesimal undergoes the most intense tidal heating, we can deduce the conditions that rule out tidally induced volcanism:

$$\mathrm{Nu}\frac{1000\,\mathrm{s}}{K_p}\frac{\kappa}{3\,\mathrm{W/(m\cdot K)}}\frac{\Delta T_c}{3000\,\mathrm{K}} \times\left(\frac{0.6\,M_\odot}{M_*}\right)^3\left(\frac{100\,\mathrm{km}}{R_p}\right)^4\left(\frac{Q_0}{3\,\mathrm{AU}}\right)^{1.5} \gtrsim 700, \tag{35}$$

which, when varying single parameter, translates to:

- $K_p \lesssim 1$ s,
- $R_p \lesssim 20$ km,
- $Q_0 \gtrsim 200$ AU,

while other conditions (e.g., $M_* \lesssim 0.07\,M_\odot$, $\kappa \gtrsim 2000\,\mathrm{W/(m\cdot K)}$, $\Delta T_c \gtrsim 2\times10^6$ K, Nu $\gtrsim 700$) are likely non-physical. Note that the obtained size constraint above (and that in the following section) is a tidal heating constraint rather than a geological constraint. We conduct similar analysis for different cooling models in Appendix D and find very similar constraints (except for a much larger Q_0 required to rule out tidally induced melting). We conclude that there exists a parameter space for tidally induced melting and it is possible for a planetesimal to form a magma ocean, serving as the reservoir of volcanism.

3.1.2 Conditions for melt maintenance

Second, once the planetesimal is melted under tidal heating, we investigate whether the tidal power, despite maintaining this melt, can further supply volcanic eruption. We do this by comparing the tidal power ($\dot{E}_t$) to the cooling rate through a solid crust above the melt ($\dot{Q}_l$), where $\dot{Q}_l > \dot{E}_t$ means that volcanism is suppressed due to insufficient tidal power.

We plot the ratio of the tidal power to the cooling rate $\frac{\dot{E}_t}{\dot{Q}_l}$ in the upper-left panel of Fig.2. For each planetesimal evolving horizontally across the figure, $\frac{\dot{E}_t}{\dot{Q}_l}$ initially increases with time, t, reaching its maximum around $e \sim 0.7$ ($\tau \sim 10$ day, not exactly at $e = 0.735$ due to the dependence of $\dot{Q}_l$ on e), and then decreases with time t, towards 0 as the planetesimal approaches circularization. At identical orbital eccentricity (along the dotted contour lines), a planetesimal with smaller q_0 tends to undergo more intense heating. We stress that due to the complexities in tidal-thermal-rheological coupling, $\frac{\dot{E}_t}{\dot{Q}_l}$ in Fig.2 only serves as a condition for volcanism for a planetesimal at a given snapshot in time instead of being an accurate prediction for the orbital parameters where volcanism is most active (see Section 4.1.1).

The regime where $\frac{\dot{E}_t}{\dot{Q}_l} > 1$ is bounded by A (tidal power equal to cooling rate high e) and B (tidal power equal to cooling rate low e), where the tidal power drops below the steady-state cooling rate.

Bound A starts horizontal, while shifts towards larger q_0 at later times, indicating that planetesimals that started on orbits with relatively large pericentres (q_0) and do not fulfill the condition for volcanism may become volcanically active at a later tidal evolution stage due to the initial increasing trend of tidal power with tidal evolution ($e \gtrsim 0.735$). A conservative estimation for A and for the q_0 required to maintain melt is $q_0 \lesssim q'_{0,crit}$ (Eq.15), with $q'_{0,crit}$ around 0.010 AU under the fiducial parameters. Similarly, using Eq.15 and placing the planetesimal at its Roche limit ($r_{Roche} = 0.00456$ AU), we deduce that tidally induced volcanism is impossible if:

$$\mathrm{Nu}'\frac{1000\,\mathrm{s}}{K_p}\frac{\kappa}{3\,\mathrm{W/(m\cdot K)}}\frac{T_c}{2000\,\mathrm{K}}\frac{f_m}{1-f_m} \times\left(\frac{0.6\,M_\odot}{M_*}\right)^3\left(\frac{100\,\mathrm{km}}{R_p}\right)^4\left(\frac{Q_0}{3\,\mathrm{AU}}\right)^{1.5} \gtrsim 3700, \tag{36}$$

where $\frac{f_m}{1-f_m} = 9$ under the fiducial parameter $f_m = 0.9$.

Assuming that only one free parameter is varied with others kept at their fiducial values, tidally induced-volcanism is ruled out if:

- $K_p \lesssim 1$ s,
- $R_p \lesssim 20$ km,
- $Q_0 \gtrsim 150$ AU,
- $f_m \gtrsim 0.9997$,

which is similar to the parameter space where melting is impossible. Therefore, we may conclude that tidally induced volcanism is a possible scenario from an energy point of view.

Meanwhile, on a near circular orbit, a planetesimals with $q_0 \lesssim 0.007$ AU can remain volcanically active (see the overlap of bound

B with the contour line $e = 0.01$). With the decrease of q_0, volcanism tends to cease at smaller eccentricities e, which is shown more explicitly in Fig.3, where the numerically computed e'_{crit} (solid blue line), circularized below which tidal heating is insufficient to support volcanism, increases from ~ 0.002 at $q_0 \sim 0.005$ AU to ~ 0.07 at $q_0 \sim 0.01$ AU. The dashed blue line in Fig.3 is the analytical upper bound of (Eq.16), which is generally of the same order of magnitude as the numerical results and whose fractional error decreases with the increase in q_0/decrease in $T_s(e = e'_{crit})$.

3.1.3 *Where to expect active volcanism*

Tidally induced volcanism is a potential scenario for planetesimals perturbed close to the white dwarf. Volcanism can occur if the planetesimal initially reaches a small pericentre, $q_0 \lesssim 0.01$ AU (with the parameter dependence given by Eq.11 and Eq.15), unless the planetesimal is small ($R_p \lesssim 20$ km) and/or possesses a weak tidal response ($\gtrsim 1000$ times weaker than the fiducial value). A planetesimal perturbed to a small pericentre distance may become volcanically active at an early tidal evolution stage on long-period highly eccentric orbits ($\tau \sim 1$ yr, $e \sim 1$). Meanwhile, tidal heating may remain sufficient to support volcanism up to short-period near circular orbits ($\tau \sim 10$ hr, $e \sim 0$), with the minimum eccentricity where tidal heating exceeds cooling approximated by Eq.16. From an energy perspective, a larger planetesimal with a smaller initial pericentre distance undergoes more intense tidal heating, and may remain volcanically active to smaller orbital eccentricities and orbital periods.

3.2 Ejecta from a planetesimal on a near circular orbit

In this section, we first compute the orbital period dispersion (dispersion in the orbital plane) and inclination (dispersion perpendicular to the orbital plane) of the ejecta based on Eq.20 and Eq.27 for a planetesimal with $R_p = 100$ km on a 4.5 hr orbit around WD 1145+017. A planetesimal circularized to such a short-period orbit without undergoing tidal disruption must have an ultimate tensile strength in the range of iron meteorites ($\gtrsim 100$ MPa, Li et al. 2025). Therefore, we assume this planetesimal to be iron-rich and we use $\rho_p = 6000\,\mathrm{kg/m^3}$ instead of the fiducial value $\rho_p = 3000\,\mathrm{kg/m^3}$. According to Eq.16, this planetesimal may still undergo active volcanism until $e \lesssim 0.001$ even when accounting for the much higher thermal conductivity of iron-rich bodies (Opeil et al. 2010; Noyes et al. 2022). In Fig.4, we plot the orbital period dispersion $\Delta\tau$ (left panel) and the orbital inclination i' (right panel) for a fixed ejection speed of 500 m/s as a function of ejection angle (θ, ϕ). In Fig.5, we plot the maximum of $|\Delta\tau|$, $\Delta\tau_{extreme}$, left panel) and the maximum i', $i'_{extreme}$ (right panel) for a range of ejection speed (u_{eject} =100–1000 m/s) and planetesimal size (R_p = 100–200 km). The key points are summarized below:

- The orbit of the ejecta remains close to that of the planetesimal: the orbital period dispersion remains $\lesssim 0.1\%$ of the orbital period (a phase shift of $\lesssim 0.02\pi$ per orbit relative to the planetesimal) and the orbital inclination of the ejecta is below ~ 0.003 (Fig.5, but note that the maximum z coordinate of the ejecta may reach ~ 2500 km $\gg R_p$; see Section 4.2.1 for discussion).
- The first-order approximations in Section 2.3.2 are in perfect agreement with the results obtained by solving the complete equations Eq.20 and Eq.27.
- For an ejection speed of 500 m/s, the extremes of $\Delta\tau$, $\Delta\tau_\pm \approx \pm 0.022$ hr (phase shift of $\sim 0.01\pi$ per orbit), occurs at $\theta = \frac{\pi}{2}$ (equator), $\phi \approx 0.451\pi$ and $\phi = 1.451\pi$ (nearly parallel/anti-parallel to the keplerian orbital velocity), as is indicated by the crosses in the left panel of Fig.4.
- $\Delta\tau$ is greatly suppressed as $\theta \to 0$ and π (poles), as is predicted by Eq.29 (Fig.4, left panel).
- $\Delta\tau$ approaches 0 near $\phi = \pi$ and 2π, where the contributions from the term $\frac{u_{eject}}{v_{orb}}$ is suppressed by the trigonometry function $\cos\phi$ in Eq.29, as $\frac{u_{eject}}{v_{orb}}$ is much larger than $\frac{R_p}{a}$ for the parameters we consider in this section (Fig.4, left panel). For longer-period near circular orbits (decrease in v_{orb} and increase in a), $\frac{u_{eject}}{v_{orb}}$ becomes more dominant, making $\Delta\tau$ and i' less sensitive to planetesimal size.
- For an ejection speed of 500 m/s, it is not rare to reach $|\Delta\tau| \sim 0.01$ hr, the observed range of drift periods around WD 1145+017 (Rappaport et al. 2016), as is indicated by the contour lines in the left panel of Fig.4.
- The maximum/minimum of $i' \approx \pm 0.0016$ (corresponding to a maximum z coordinate of ~ 1000 km) occurs when the volcanism eruption is at the poles of the planetesimals ($\theta = 0, \pi$) and approaches 0 when eruption is at the equator of the planetesimal ($\theta = \frac{\pi}{2}$), as is predicted by Eq.33 (Fig.4, right panel).
- i' is insensitive to ϕ for near circular orbit (Fig.4, right panel).
- The maximum of $|i'|$ (ejection at poles) corresponds to the minimum of $|\Delta\tau|$ (~ 0), and vice versa (Fig.4).
- The maximum orbital period dispersion and inclination increases with planetesimal size and volcanic ejection speed, with the latter usually being dominant (Fig.5).

According to Fig.5, although the discrete secondary periods of the order of magnitude 0.01 hr around WD 1145+017 (Rappaport et al. 2016) can be explained by volcanism, volcanism can hardly account for the six orbital periods, A–F (A being the 4.5 hr period that is dominant/primary), derived from K2 data ranging from 4.5 to 4.9 hr (Vanderburg et al. 2015). Conversely, if the 4.5–4.9 hr period range originates from orbit dispersion from a single planetesimal, an ejection speed $\gtrsim 10000$ m/s is required. Therefore, the existence of orbital periods B, C, D, E and F (if not being false positives) may imply the existence of multiple bodies/more energetic dynamical processes (e.g., collisions, early stage tidal disruption of a large parent body and subsequent tidal circularization of its constituents). With the proof of accuracy for the first-order approximations in Section 2.3.2, we can deduce the maximum orbital period dispersion for the 9.937 hr and 11.2 hr periods around ZTF J0328-1219 with $M_* = 0.731\,M_\odot$ (Vanderbosch et al. 2021) assuming (near) circular orbit. We find out that $\Delta\tau \lesssim 0.1$ hr, which hardly explains the two observed orbital period dispersion > 1 hr using a single planetesimal. Therefore, the two periodic signals around ZTF J0328-1219 potentially corresponds to distinct bodies. As eccentricity can promote orbital dispersion (see Section 4.1.6), we further test the case where $e = 0.01$ for WD 1145+017 and $e = 0.2$ for ZTF J0328-1219 (based on Fig.11 of Li et al. 2025). We find out that these eccentricities remain insufficient to explain the 4.5 hr–4.9 hr period in K2 data for WD 1145+017 and the 9.937 hr and 11.2 hr periods for ZTF J0328-1219, emphasizing the preference for multiple-body scenarios.

4 DISCUSSION

Motivated by the observed periodic transits around a small sub-set of white dwarfs, potentially linked to close-in disintegrating planetary bodies, we explore the fate of the planetary bodies orbiting white dwarfs. We study a scenario where planetesimals perturbed just outside the Roche limit undergo rapid tidal evolution, ending up on various orbits closer to the white dwarf (Li et al. 2025). Dur-

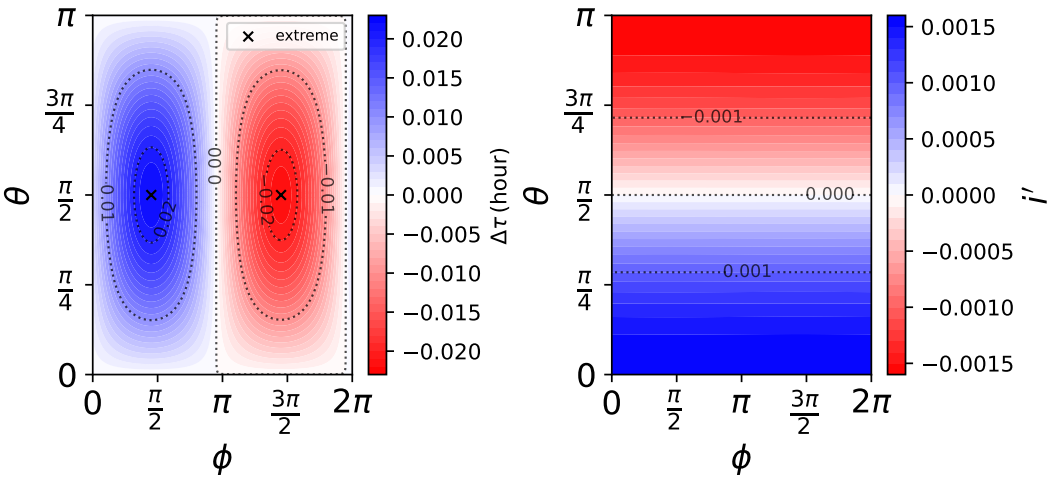

Figure 4. The orbital period (left panel) and orbital inclination (right panel) of the volcanic ejecta with ejection speed 500 m/s launched at different positions of the planetesimal surface relative to the 4.5 hr orbital period of the planetesimal on a (near) circular orbit around a 0.6 $M_\odot$ white dwarf. The planetesimal is assumed to have a density of $\rho_p = 6000\,\mathrm{kg/m^3}$. The crosses in the left panel are the analytically predicted extremes (Section 2.3.2).

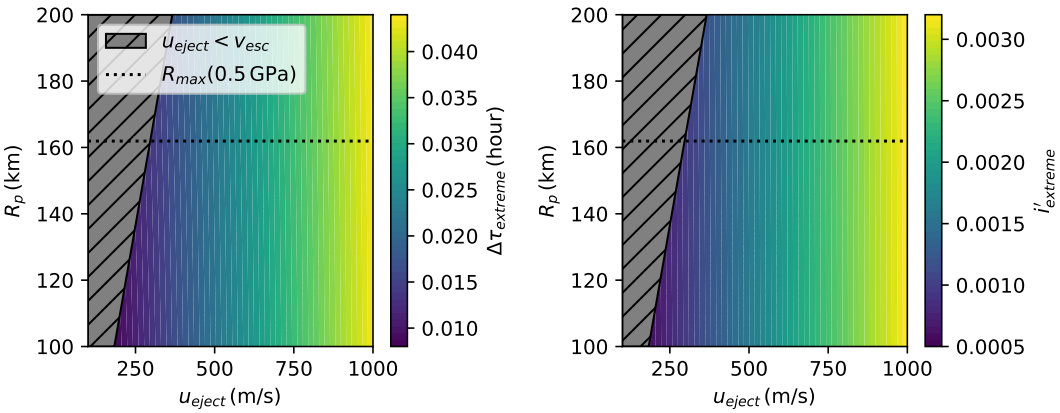

Figure 5. The maximum orbital period dispersion ($\Delta\tau_{extreme}$, left panel) and the extent perpendicular to the orbital plane/along the z axis ($\Delta z_{extreme}$ right panel) from the planetesimal on a 4.5 hr (near) circular orbit around a 0.6 $M_\odot$ white dwarf for different ejection speeds and planetesimal sizes. The density of the planetesimal is $\rho_p = 6000\,\mathrm{kg/m^3}$. The shaded area corresponds to the parameter space where the ejection speed is less than the escape speed. The dotted line is the maximum radius a planetesimal could have without undergoing tidal disruption for a tensile strength of 500 MPa (~ upper limit of measured meteorites Ostrowski & Bryson 2019; Pohl & Britt 2020).

ing the orbital decay/circularization, the accompanied tidal heating of the planetesimal potentially triggers volcanism, with the erupted dust being a possible origin of transits.

In this section, we firstly discuss the limitations of the model regarding the tidally induced volcanism scenario (Section 4.1), starting with the tidal and thermal modeling (Section 4.1.1, Section 4.1.2), Section 4.1.3 and Section 4.1.4), followed by additional orbital perturbations to the volcanism ejecta (Section 4.1.5) and tidally induced volcanism on eccentric orbits (Section 4.1.6). Then, we apply our model to observations in Section 4.2, focusing on WD 1145+017, via the mass loss rate during volcanism (Section 4.2.2), the resultant transit depth, duration and phase shift of primary transit (Section 4.2.1). Then, we predict the frequency of tidally induced volcanism and its contributions to white dwarf pollutants (Section 4.2.3). Finally, we briefly discuss other transit-related physical processes accompanied with the tidally induced volcanism scenario (Section 4.3) and other existing models explaining transits (Section 4.4).

4.1 Model limitations

4.1.1 Tidal, thermal and rheological coupling

In this paper, we only consider the conditions required for volcanism from an energy pointy of view, by comparing tidal heating to cooling at a given snapshot in time. In reality, volcanism and tidal evolution are much more complex. Volcanism of planetesimals may be accompanied with thermal processes such as melting and advection, and hence, alterations of the planetesimal's properties, for instance, rheology, composition, mass and radius. As a result, both the tidal evolution and thermal evolution of the planetesimal are affected.

We utilize the CTL model to simulate the orbital evolution of the planetesimal and the resultant heat deposition. Under the CTL model, the tidal evolution rate is modulated by $T_p = \frac{K_p M_*^2 R_p^5}{M_p} \propto \frac{K_p R_p^2}{\rho_p}$ (Table 1), which is assumed to remain constant along the tidal evolution track. In reality, planetesimal size (R_p) and density (ρ_p)

can both vary under volcanism eruptions. Furthermore, variations in rheology during melting and volcanism can alter the tidal response of the planetesimal (K_p).

On the other hand, the dissipation of planetary bodies under tide (e.g., usually quantified by the tidal quality factor Q or the multiplicity of potential love number and constant time lag $K_p = 3k_2\Delta t$ in this study) is poorly constrained and model-dependent. In section 3.1, we show that unless the tidal evolution is more than 2–3 orders of magnitude slower than the model prediction, there remains a possibility of tidally induced volcanism. In other words, tidally induced volcanism is not rare in terms of the parameter space. However, we are unable to predict the fraction of exoplanetary bodies lying in the volcanically active regime. There may exist a population of planetesimals that disfavour the tidal circularization scenario, due to, for instance, lacking bodies with strong tidal response (e.g., no large-sized bodies, difficulty in raising tidal bulges), gravitational perturbations being too strong such that planetesimals can hardly undergo long-term tidal evolution (e.g., ejection), gravitational perturbation being too weak such that planetesimals are hardly perturbed close enough to the white dwarf for strong tidal interactions.

Furthermore, the CTL model fixes the rheological dependence of tidal response (proportional to tidal forcing frequency), such that the summed tidal dissipation efficiency of all forcing frequencies can be characterized by a single proportionality constant along the tidal evolution track (e.g., K_p in this study). In reality, tidal dissipation efficiency (and its dependence on the forcing frequency) and the tidal energy distribution inside the body are closely correlated with the rheology of the body, which is altered during melting and the accompanied compositional and structural variations (Tobie et al. 2005; Beuthe 2013; Makarov & Efroimsky 2013; Noyelles et al. 2014; Storch & Lai 2014; Zahnle et al. 2015; Boué & Efroimsky 2019; Veras et al. 2019; Vick et al. 2023; Seligman et al. 2024). How tidal interactions are altered during melting/volcanism depends on the applied tidal model and the properties of the planetary body. For instance, under the viscoelastic tidal model, as the thickness of the solid mantle decreases during melting, some planetesimals (given the proper rheology, rigidity, relaxation frequency, etc.) may undergo a runaway process where tidal dissipation efficiency increases before saturation (Seligman et al. 2024). Meanwhile, the tidal evolution rate may be further enhanced in the presence of a magma ocean, whose dynamics and rheology differ from that of a solid (Tyler et al. 2015; Farhat et al. 2025). Another important consequence of a rheology dependent tidal response is that a stable pseudo-synchronous rotation state may not persist, adding uncertainties to the Roche limit of the planetesimal (Makarov & Efroimsky 2013; Storch & Lai 2014; O'Connor & Lai 2020; Vick & Lai 2020). Moreover, high-eccentricity tidal interactions, which mainly occur near the pericentre, may possess distinct dynamics from their low-eccentricity counterparts (for instance, chaotic and non-chaotic dynamical tides studied for gas giants and stars which potentially lead to more efficient tidal dissipation and hence more rapid tidal heating; see Appendix S for details), thus requiring separate, but self-consistent, modeling (Press & Teukolsky 1977; Moe & Kratter 2018; Veras & Fuller 2019; Vick et al. 2019; Veras & Fuller 2020; Glanz et al. 2022; Rozner et al. 2022).

Despite uncertainties in tidal evolution that may prevent or promote tidally induced volcanism from an energy prospect, long-term volcanic activities may also be disfavoured for certain planetesimals even if sufficient tidal power is provided. For instance, there may exist planetesimals: 1. that undergo thermal disruption (e.g., due to thermal stress), 2. that maintain the equilibrium between heating and cooling without undergoing volcanism (for instance, via more efficient cooling, or suppressing tidal evolution in response to more intense tidal heating), 3. that lack volcanic gas/consume the volcanic gas rapidly to provide excess pressure for eruption and 4. that undergo runaway volcanism, losing a considerable amount of mass, suppressing tidal evolution at an early tidal evolution stage. On the other hand, the conditions for tidally induced volcanism may be much easier to achieve than what we assume, without the need of a shallow magma ocean (Park et al. 2025).

Finally, the orbital parameters where a planetesimal is volcanically active (e.g., the boundaries between melting and volcanism/II and III in Fig.2) are potentially sensitive to the thermal modeling (see Appendix D), including the heat transport mechanisms and tidal energy distribution. For instance, efficient cooling/tidal energy partially damped near the surface and lost rapidly may slow down the propagation of melt, shifting the volcanically active stage of the planetesimal to a later tidal evolution stage. On the other hand, if tidal energy is preferentially distributed at the position where the shallow magma ocean for volcanism is formed, or a shallow magma ocean is not the necessary condition for volcanism (Park et al. 2025), the volcanically active stage may be brought to an earlier tidal evolution stage.

To properly model the tidally induced volcanism, a model coupling both solid and fluid tidal interactions, thermal and rheological evolution of the planetesimal is required.

4.1.2 Surface melting/sublimation

The deposition and transport of tidal energy results in additional heat flux through the surface, hence increasing the surface temperature of the planetesimal. Furthermore, stellar irradiation may lead to high surface temperature, especially for the day side of tidally locked planetesimals. We find that tidal heating and/or stellar irradiation rarely lead to melting/sublimation of the planetesimal's surface, unless the planetesimal is perturbed sufficiently close-to/within the typical Roche limit of a rocky body ($\sim$ 0.004 AU) and circularize rapidly at an early white dwarf cooling age (see Appendix L). Hence we do not consider planetesimals that undergoes surface melting/sublimation as a common representative of the planetesimal population. Furthermore, volcanism may be greatly suppressed for planetesimals whose surfaces undergo melting/sublimation under intense tidal heating, which requires concentration of tidal energy at the surface and is associated with much more rapid cooling (cooling through sublimation and/or enhanced thermal emission). Therefore, the planetesimal undergoing tidally induced volcanism should usually preserve a solid mantle where cooling through conduction is dominant.

4.1.3 Thermal properties of planetesimals

The thermal properties of planetesimals is crucial in determining when they melt and how fast they cool. In this work, we parameterize the energy required for melting in terms of the a constant specific heat capacity, c_p and ΔT_c, a temperature representation of melting energy computed using the properties of forsterite (see Appendix B). Meanwhile, the cooling process in the presence of a shallow melt reservoir is parameterized using a constant thermal conductivity κ. For a range of reasonable values for these parameters (different mineralogy), and accounting for the corresponding temperature dependence, we find that our chosen fiducial values (Table 1) leads to a conservative estimation for volcanism to occur. Accounting for the uncertainties of the thermal properties, the critical initial pericentre distance of melting $q_{0,crit}$ (Eq.11) may maximally increase by

$\approx 20\%$, and the critical initial pericentre distance for maintaining the melt at high eccentricity $q'_{0,crit}$ (Eq.15) may maximally increase by $\approx 10\%$ (see Appendix K).

On the other hand, additional heat loss channel quantified by Nu, for instance, convection, may suppress the parameter space of volcanism. In the limiting case where Nu = 10 for convection in melt-bearing solid layer (see Appendix C), $q_{0,crit}$ and $q'_{0,crit}$ may maximally reduce by $\sim 25\%$, which is comparable to the potential maximum increase above.

Therefore, we do not expect that the thermal properties of the planetesimal and the potential convective cooling can suppress the parameter space of tidally induced volcanism significantly.

4.1.4 The Roche limit of planetesimals

This work assumes that planetesimals are perturbed from an outer planetary belt onto highly eccentric orbits around the white dwarf. If they are perturbed too close at the pericentres, they are torn apart by the differential tidal forces. This work focuses on planetesimals that avoid being torn apart, such that their orbits can evolve under tide. The Roche limit (Eq.7) provides a useful representation for how close a planetesimal can come to the white dwarf without being tidally disrupted.

The Roche limit is a function of planetesimal properties such as tensile strength, shape and density. We assume that the planetesimal is spherical and rigid, where it is strongest against tidal disruption. In this case, a strength-less planetesimal with the density similar to that of Solar System ordinary chondrites can circularize to a $\lesssim 10$ hr orbit without undergoing tidal disruption, while a planetesimal with $R_p \sim 100$ km must be of the tensile strength to Solar System iron meteorites to avoid tidal disruption if it is tidally circularized to a 4.5 hr orbital period (Li et al. 2025). However, as is the case for Solar System asteroids, planetesimals are better described by ellipsoid rather than spheres (Mommert et al. 2018), potentially making them weaker to tidal disruption (Davidsson 1999; Li et al. 2025). On the other hand, the tensile strength of planetesimals may weaken with an increase in planetesimal size (scale effect, Ahles et al. 2021), and the tensile strength may also alter significantly during thermal evolution (Pohl & Britt 2020). All these effects, together with the spin evolution of the planetesimal under tidal interactions (Section 4.1.1), add uncertainties to the estimation of the Roche limit of a planetesimal, with the deformation and scale effect tending to increase the Roche limit (hence reducing the allowed initial pericentre distance space for tidally induced volcanism) and the effects of the thermal evolution, spin evolution being uncertain.

4.1.5 Orbital perturbations

In Section 2.3, we compute the orbital period dispersion of the ejecta analytically, neglecting additional effects such as the gravitational effect of the planetesimal, mutual interactions of the ejecta, general relativistic effect and radiation forces. In this section, we further investigates some of these effects.

First, we consider the gravitational effect of the planetesimal. The simulations using Rebound (including GR effect, Rein & Liu 2012) give qualitatively similar results as the analytical expression (fractional error $\lesssim 5\%$ for $u_{eject} = 500$ m/s, with the error decreases with the increase in u_{eject}. The exceptions (large fractional error) concentrate in a narrow parameter space of ejection angle (θ, ϕ) where $\Delta\tau \to 0$ in Fig.4. Within this narrow parameter space, the ejecta remains close to the planetesimal, continuously being perturbed and with a higher risk of collisions (see Appendix M). Accounting for the very limited parameter space where the analytical model loses accuracy and the consistency in the parameter dependence between the analytical and numerical results, it is generally reasonable to apply the analytical model even when accounting for the planetesimal.

Second, we consider the effect of stellar irradiation on the orbital evolution of the ejecta, with the radiation pressure and Poynting Robertson (PR) drag being the dominant perturbations for dust.

The radiation pressure effectively leads to a reduced mass of the star, $M_*(1-\beta)$, as seen from the ejecta, with β the fraction of radiation to gravitational force (Wyatt & Whipple 1950). As a result, the ejecta moves at sub-keplerian speed and has a slightly longer orbital period and lower GR precession rate than its counterpart with keplerian speed at the same orbit (see Appendix M).

On the other hand, the PR drag leads to the loss of angular momentum of the ejecta orbiting the white dwarf. As a result, the ejecta drifts inwards, altering the parameter space where collisions between the ejecta and the planetesimal occur (see Appendix M). The orbital-averaged semi-major axis and eccentricity evolutionary equations under PR drag are (Wyatt & Whipple 1950; Veras et al. 2015, 2022):

$$\frac{da}{dt} = -\frac{3(Q_{abs} + Q_{ref})(2 + 3e^2)L_*}{16\pi c^2 D\rho a(1-e^2)^{\frac{3}{2}}}, \tag{37}$$

$$\frac{de}{dt} = -\frac{15(Q_{abs} + Q_{ref})eL_*}{32\pi c^2 D\rho a^2\sqrt{(1-e^2)}}, \tag{38}$$

where Q_{abs} is the absorption coefficient, Q_{ref} is the reflection coefficient (albedo), D and ρ are radius and density of the particle. We assume that $Q_{abs} + Q_{ref} = 1$.

The PR accretion timescale (timescale of accreting onto the white dwarf) of a particle on a near circular orbit is:

$$t_{PR} \sim 8\,\mathrm{yr} \times \left(\frac{M_*}{0.6\,M_\odot}\right)^{\frac{2}{3}} \frac{0.01\,L_\odot}{L_*} \frac{D}{1\,\mu\mathrm{m}} \frac{\rho}{3000\,\mathrm{kg/m^3}} \left(\frac{\tau}{4.5\,\mathrm{hr}}\right)^{\frac{4}{3}} \frac{\Delta\tau}{\tau}. \tag{39}$$

The long-lived drift periods around WD 1145+017 is observed to have an orbital decay timescale over 1000 yr (Rappaport et al. 2016). Assuming that PR drag contributes to the orbital decay, we find out that at least some of the transiting particles are larger than 100 μm, not violating the typical size distribution of volcanism ejecta (Butwin et al. 2019; Osman et al. 2020). Meanwhile, some of the dips only last for weeks (Rappaport et al. 2016), potentially due to the removal of small particles under PR drag. For instance, for $\frac{\Delta\tau}{\tau} = 0.002$ (from the orbital period of the planetesimal to the shortest observed drift period), t_{PR} is ~ 10 day for micron-sized particles (hence we do not violate the lower bound for the particle size deduced from wavelength-independent transit light curves, $\sim 0.5\,\mu$m Alonso et al. 2016).

Based on the analytical model, we can broadly predict the dispersion of the dust. However, the long-term evolution of the ejecta involves rich dynamics. To properly model the evolution of volcanism ejecta, and hence the transit light curve, one should account for the orbital perturbations due to the planetesimal and radiation, and additionally, the mutual interactions among the volcanism ejecta (e.g., gas-dust interactions) and the magnetic perturbations that may become relevant in the presence of hot plasmas from volcanism/sublimation.

System	Mass ($M_\odot$)	Peiord	Predicted eccentricity
ZTF J0139+5245	0.52	107.2 day	~ 0.98
WD 1054–226	0.62	25 hour	~ 0.4

Table 2. A list of the properties of the observed transiting systems potentially correspond to eccentric orbits (Vanderbosch et al. 2020; Farihi et al. 2022), together with the predicted orbital eccentricity (Li et al. 2025).

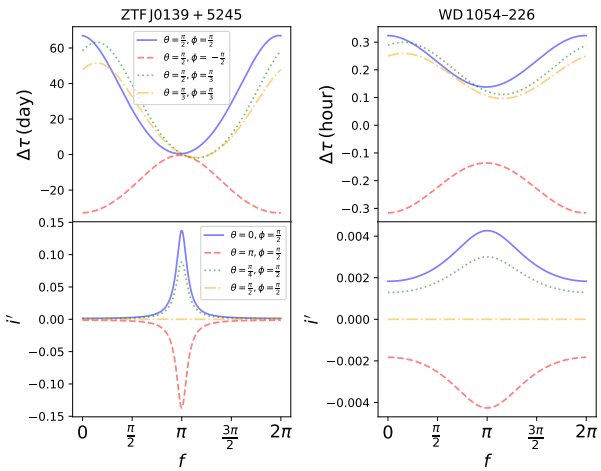

Figure 6. The orbit dispersion (upper panel: period, lower panel: inclination) relative to the planetesimal around ZTF J0139+5245 (left panel) and WD 1054-226 (right panel), respectively, as a function of true anomaly for four sets of ejection angles. The ejection speed is assumed to be 500 m/s with the white dwarf mass and transit periods given in Table 2 (other free parameters identical to Table 1).

4.1.6 Volcanism ejecta of planetesimals on eccentric orbits

In Section 3.2, we mainly focus on volcanism ejection from a planetesimal on a near circular orbit. However, we show that volcanism can equivalently occur on a highly eccentric orbit in Section 3.1, potentially corresponding to the moderate/long-period transits observed around white dwarfs. In this section, based on the two transiting systems ZTF J0139+5245 and WD 1054-226 (parameters listed in Table 2), we discuss the orbit dispersion of the ejecta from a planetesimal on a eccentric orbit (see Appendix H for analytical approximations for moderately eccentric orbit).

In Fig.6, we plot the predicted orbital period dispersion $\Delta\tau$ (upper panel) and inclination i' (lower panel) (computed using the analytical model, which generally agrees with N body simulations) for ZTF J0139+5245 (left panel) and WD 1054-226 (right panel) for ejection at different true anomalies f with a fixed ejection speed of 500 m/s. The key points are summarized below:

- The orbit dispersion is greatly enhanced by orbital eccentricity, up to $\sim 60\%$ in τ and up to 0.15 for i' for ZTF J0139+5245.
- The orbit dispersion is sensitive to the true anomaly for highly eccentric orbits, with the period dispersion more enhanced near the pericentre and inclination more enhanced near the apocentre.
- With the decrease in orbital eccentricity, the orbit dispersion gradually converges to the that of the planetesimal. This is the case for WD 1054-226, with the orbital period dispersion declines to $\lesssim 1\%$ of the orbital period of the planetesimal and inclination decays to $\lesssim 0.004$.

For highly eccentric orbits, the orbit of the volcanism ejecta may seem irrelevant to that of the parent body due to the much larger orbit dispersion compared to near circular orbits. Hence, for long-period dust cloud-like transits, unless multiple transits with identical periods are verified, it is hard to tell whether the observed periodic signal is an indication of the orbital period of a planetary body. Although the theoretical maximum of the transit depth is much higher for highly eccentric orbits (see Appendix O), one must be cautious whether the much more dispersed ejecta remains optically thick.

4.2 Does volcanism lead to transit and pollutants?

In the previous sections we illustrate that tidally induced volcanism is possible from an energy point of view and can occur in planetesimals with a wide variety of orbits (Section 3.1). If we directly link the observed periods for the transiting material to volcanically active planetesimals, there is broad agreement (Li et al. 2025).

In this work, we speculate that dust ejected from volcanically active planetesimals is initially sufficiently opaque to block light from the star. In this section, we discuss the features of the light curves that would result from volcanically active planetesimals orbiting white dwarfs.

In Section 3.2, we show that for a planetesimal on (near) circular orbit, volcanism can lead to dust spanning a narrow range of orbital periods and inclinations centered around those of the planetesimal (primary transits correlated with the planetesimal). On the other hand, a large amount of dust launched with small dispersion in ejection velocity may be interpreted as a secondary transit. We show that the predicted orbital period dispersion is able to cover the secondary drift periods around WD 1145+017 for a ejection speed of $\sim 500\,\mathrm{m/s}$ (Section 3.2).

The remaining questions are: 1. whether volcanism can explain other transiting features (e.g., phase shift of primary transits, variability/dust across the orbit, the observed transit depth and transit duration), and 2. the contributions of volcanism to white dwarf pollutants, which we will discuss in this section.

4.2.1 Transit features

Due to the distinct orbital parameters the ejecta could have relative to the planetesimal, (a fraction of) the ejecta leave the planetesimal and diffuse away. In this section, we will show that volcanic ejection can broadly explain the transit depth, transit duration, and the observed 180° phase-shift of the transits for WD 1145+017 based on the analytical expressions in Section 2.3.2.

The maximum transit depth $\frac{\Delta L}{L}$ assuming a rectangular region of dust with infinite width and a height of $2\Delta z$ is given by:

$$\frac{\Delta L}{L} = \frac{2\sin\theta_z\cos\theta_z + 2\theta_z}{\pi}, \tag{40}$$

where $\theta_z = \arcsin\left(\frac{\Delta z}{R_*}\right)$. The maximum of Δz due to volcanism ejection is a function of maximum orbital inclination, which, for a near circular orbit, is (Eq.34):

$$\Delta z_{max} = a\sin i'_{max} \approx a\sqrt{\frac{R_p^2}{a^2} + \frac{u_{eject}^2}{v_{orb}^2}}. \tag{41}$$

The orbital period dispersion of the ejecta relative to the planetesimal leads to the formation of leading (shorter-period) and trailing

(longer-period) tails, which are phase shifted relative to the planetesimal in the opposite direction, gradually filling the orbit of the planetesimal. As a result, the transit light curve will gradually become noisy over the orbital phases, and the theoretical maximum of the transit duration increases with time. Ultimately, the leading tail will catch up the trailing tail, when the dust spans over the orbit and mutual interactions among the ejecta may become significant (see Appendix O for an illustration of this scenario). The maximum transit duration for volcanism ejecta (before the leading tail catches up the trailing tail) is given by (Tingley & Sackett 2005; Burke 2008):

$$\begin{aligned} t_{transit,max} &\approx \left(\frac{\Delta\tau_+}{\tau} - \frac{\Delta\tau_-}{\tau}\right) t + \frac{R_*\tau}{\pi a} \\ &\approx 6t\sqrt{\frac{u_{eject}^2 a}{GM_*} + (1+S)^2\frac{R_p^2}{a^2}} + \frac{R_*\tau}{\pi a}, \end{aligned} \tag{42}$$

where $\frac{\Delta\tau_\pm}{\tau}$ is given by Eq.31 and t is the time elapsed after the ejection.

On the other hand, the time taken for the leading tail to catch up the trailing tail (t_{catch}) can be estimated via:

$$\begin{aligned} t_{catch} &\approx \tau\left(\frac{\Delta\tau_+}{\tau} - \frac{\Delta_-}{\tau}\right)^{-1} \\ &\approx \frac{\tau}{6\sqrt{\frac{u_{eject}^2 a}{GM_*} + (1+S)^2\frac{R_p^2}{a^2}}}. \end{aligned} \tag{43}$$

For WD 1145+017, we have $\left(\frac{\Delta L}{L}\right)_{max} \sim 50\%$ ($\Delta z_{max} \sim 2500$ km), $t_{transit,max} \sim 0.02t + 40$ s, and $t_{catch} \sim 50\tau \sim 9$ day (see Appendix O for numerical simulations).

In comparison to the K2 data, where the transit duration is 4 min and the transit depth is 8% (undiluted, Vanderburg et al. 2015), the maximum transit depth of our model is well above the observed value. The minimum time to reach the observed transit duration after volcanism is ~ 3 hr. On the other hand, follow-up ground based observations show much deeper transit depth, up to 50% (Vanderburg et al. 2015; Gänsicke et al. 2016; Rappaport et al. 2016; Vanderburg & Rappaport 2018), reaching the upper bound of our model. According to t_{catch}, we predict self-interactions among the volcanism ejecta after ~ 9 day, potentially leading to observable features out of phase from the planetesimal (starting near 180°, see Appendix O), roughly in agreement with the observed phase shift (appeared ≈ 1 week later, Vanderburg et al. 2015). If we constrain the volcanism ejection speed based on the time interval for observing transits with 180° phase shift $u_{eject,max} \gtrsim 1300$ m/s, we find out $\Delta z_{max} \gtrsim 3000$ km and $\left(\frac{\Delta L}{L}\right)_{max} \gtrsim 60\%$. If the maximum ejection speed exceeds ~ 2500 m/s, the dust is able to cover the whole white dwarf ($\Delta z \geq R_*$).

Tidally induced volcanism can broadly recover the observed transit features around WD 1145+017, with the observed transit depth close to the theoretical maximum, potentially suggesting an underestimation of the orbit dispersion, either due to an underestimation of volcanic ejection speed or the existence of other dynamical processes (e.g., sublimation, mutual interactions, magnetic forces, production of density waves/vortex Taddeucci et al. 2021 in an evolved disk composed of previous volcanic ejecta by new ejections). A detailed modeling of the ejecta constrained by the observations of the dust/gas disks (e.g., infrared excess, emission features) is required to better understand its evolution and the corresponding transit features.

4.2.2 *Dust production rate from volcanism*

The dust ejected from volcanic activity may not only result in to optical transits, but can also be accreted by the white dwarf. In this section we show that the maximum possible mass loss rate from volcanism, neglecting any geological control, and accretion efficiency, is sufficient to explain the observed accretion rates seen for WD 1145+017 for a 100 km-sized planetesimal. Clearly, we do not anticipate that planetesimals lose mass at this maximum rate throughout their lifetime, but instead discuss late in this section the stochastic nature of the process that enables the planetesimal to survive the long-term tidal evolution.

During volcanism ejection, the thermal energy of the ejecta is lost to the environment (cooling via advection). The tidal heating must be sufficient to sustain this rate of heat loss. The heat loss rate due to ejection $\dot{Q}_e$ can be approximated as:

$$\dot{Q}_e = \frac{1}{2}\dot{m}u_{eject}^2 + \dot{m}c_p\Delta T_c, \tag{44}$$

The maximum volcanic mass loss rate can be estimated by setting $\dot{Q}_e$ equal to the difference between the tidal power ($\dot{E}_t$, Eq.6) and the non-volcanic heat loss rate ($\dot{Q}_l$, Eq.12) (the energy required for fracture is usually negligible as is shown in Appendix J):

$$\dot{m} = \frac{\dot{E}_t - \dot{Q}_l}{\frac{1}{2}u_{eject}^2 + c_p\Delta T_c}. \tag{45}$$

where the denominator is usually dominated by the thermal energy term $c_p\Delta T_c$ and for a high dust production rate, the numerator is dominated by $\dot{E}_t$. Hence, we may approximate the maximum mass loss rate via (see Appendix N for numerical results):

$$\begin{aligned} \dot{m}_{max} &\sim \frac{\dot{E}_t}{c_p\Delta T_c} \\ &\sim 2\times10^8\,\mathrm{g/s}\frac{K_p}{1000\,\mathrm{s}}\left(\frac{M_*}{0.6\,M_\odot}\right)^3\left(\frac{R_p}{100\,\mathrm{km}}\right)^5\left(\frac{e}{0.01}\right)^2 \\ &\times\left(\frac{0.005\,\mathrm{AU}}{q_0}\right)^9\left(\frac{1000\,\mathrm{J/(K\cdot kg)}}{c_p}\right)\left(\frac{3000\,\mathrm{K}}{\Delta T_c}\right), \end{aligned} \tag{46}$$

with the dominant factor being q_0 followed by R_p. We acknowledge that is nonphysical for $\dot{m}_{max}$ to exceed the ejection-speed limited mass loss rate, $4\pi R_p^2\rho u_{eject}$ (with ρ the vent exit density). For the parameters we consider in this section, $4\pi R_p^2\rho u_{eject}$ is orders of magnitude larger than the range of mass loss rate limited by tidal power, even when taking the minimum ejection speed, 10 m/s.

For a planetesimal with a radius of 100 km on a 4.5 hr period ($q_0 = 0.0027$ AU) around WD 1145+017 with an eccentricity of 0.01. $\dot{m}_{max}$ is $\sim 5\times10^{10}$ g/s, one order of magnitude larger than the predicted value based on transits, 8×10^9 g/s (note that this value is uncertain and model-dependent Vanderburg et al. 2015) and slightly larger than the accretion rate of WD 1145+017, 4.3×10^{10} g/s (Xu et al. 2016). Setting $\dot{m}_{max} = 8\times10^9$ g/s, we find a lower limit of planetesimal radius ~ 70 km to explain the transit around WD 1145+017 via tidally induced volcanism. Under the mass loss rate of 8×10^9 g/s and 4.3×10^{10} g/s, the planetesimal with $R_p = 100$ km and $\rho_p = 6000$ kg/m^3 will lose 10% of its mass in $\sim 10^4$ yr and $\sim 2\times10^3$ yr, respectively, much longer than the observation span of this system. Hence, volcanism is a possible explanation for transits, and can potentially contribute to white dwarf pollutants.

Conversely, for a strength-less rocky planetesimal ($\rho_p \lesssim$

4000 kg/m^3 Pohl & Britt 2020 and hence Roche limit $\gtrsim$ 0.00415 AU) to reach a dust production rate of 8×10^9 g/s, the planetesimal must be larger than $\sim$ 150 km. For a planetesimal with a radius of 800 km (above which the escape speed exceeds the maximum volcanic ejection speed), the planetesimal must be perturbed within $\sim$ 0.01 AU to reach a dust production rate of 8×10^9 g/s.

If volcanism is the origin of transits corresponding to short-period near circular orbit, problems remain on whether the planetesimal still have sufficient amount of gas and silicate melts to supply volcanism eruption at the end of its tidal evolution stage. To explain tidally induced volcanism that leads to transits on near circular orbits, either mass loss during tidally induced volcanism is much less efficient than the theoretical maximum, or tidally induced volcanism preferentially occurs at a late tidal evolution stage for some planetesimals. Some potential scenarios include:

- High speed volcanic ejection (beyond the escape speed) with a large amount of material erupted is of low possibility, such that high mass loss rate cadences are discrete and of limited lifetime. The planetesimal can recycle a large fraction of its volcanic products back to its interior and re-triggering volcanism eruption after the corresponding geological timescale. The true accumulated mass loss of the planetesimal is much smaller compared to its counterpart integrated using the theoretical maximum mass loss rate.
- The planetesimal starts massive and only the extremely high speed ejection can contribute to mass loss. Mass loss starts slow as only the extremely high speed eruption can produce volcanic products escaping from the planetesimal. High mass loss rate may only become relevant at a late tidal evolution stage when the planetesimal loses a fraction of its mass, reducing its escape speed to a certain degree.
- Cooling may be efficient enough to delay the the propagation of melt reservoir towards the surface such that volcanism from a shallow melt reservoir only occurs at a late tidal evolution stage (see Section 4.1 and Appendix D).

4.2.3 *Frequency of tidally induced volcanism and signatures in white dwarf pollutants*

In this study, we focus on a population of planetesimals gravitationally perturbed close to the white dwarf (just outside the Roche limit). Meanwhile, planetesimals can be perturbed within the Roche limit, where they undergo tidal disruption and subsequent accretion onto the white dwarf, which is the leading theory for white dwarf pollution. Both processes can occur simultaneously. Similar to the debris formed from tidal disruption, volcanic ejecta can be accreted onto the white dwarf, via, for instance, PR drag (Section 4.1.5). As a result, tidally induced volcanism provides an additional channel of white dwarf pollutants. In this section, we compare between the frequency and mass contributions of tidal disruption and tidally induced volcanism ($\frac{N_{volcanism}}{N_{disruption}}$, $\frac{M_{volcanism}}{M_{disruption}}$).

We investigate a simple model based on the following assumptions:

- A size distribution of planetesimals with a probability density function $P(R_p) \propto R_p^{\beta}$, from $R_{p,min} = 10$ km to $R_{p,max} = 1000$ km (Dohnanyi 1969; Gáspár et al. 2012; Pan & Schlichting 2012; Simon et al. 2016, 2017).
- An uniform planetesimal density distribution between 3000 kg/m^3 and 6000 kg/m^3.
- An initial pericentre distribution with a probability density function $P(q_0) \propto q_0^{\alpha}$.
- A K_p ($3k_2\Delta t$ which quantifies the tidal dissipation efficiency) distribution where $\log_{10} \frac{K_p}{1\,\mathrm{s}}$ uniformly distributes between 0 and 4 (the lower limit is given by the measured value of gas giant Fellay et al. 2023 and the upper limit is arbitrarily chosen to be an order of magnitude larger than the fiducial value).
- A Roche limit (r_{Roche}) distribution that is uniform between 0.003 AU and 0.005 AU (estimated using the property range of Solar System ordinary chondrites Pohl & Britt 2020).
- A planetesimal potentially undergoes volcanism when $r_{Roche} < q_0 < q'_{0,crit}$, with $q'_{0,crit} = 0.01\,\mathrm{AU} \left(\frac{K_p}{1000\,\mathrm{s}}\right)^{\frac{2}{15}} \left(\frac{R_p}{100\,\mathrm{km}}\right)^{\frac{8}{15}}$ and when the tidal escaping timescale $\tau_{e,tide} = 5\frac{r_H M_p q_0^{7.5}}{G K_p M_*^2 R_p^5 Q_0^{0.5}}$ (with r_H the Hill radius of a 10 Earth mass planet at 3 AU, Appendix P) is smaller than the 'outward' perturbation timescale τ_p such that $\log_{10} \frac{\tau_p}{1\,\mathrm{Myr}}$ uniformly distributed between between -3 to 3.
- A distribution of the fraction of planetesimal mass accreted by the white dwarf during tidally induced volcanism $f_{m,v} \frac{\max(0, 1000\,\mathrm{m/s} - v_{esc})}{1000\,\mathrm{m/s} - 10\,\mathrm{m/s}}$ (accounting for the lower probability of mass loss for a higher escape speed) where $\log_{10} f_{m,v}$ uniformly distributes between -4 and -1.
- An accretion efficiency of tidal disruption 0.5 (arbitrary choice, accounting for the fact that the debris disk can be continuously perturbed by the planet that perturbed the planetesimal in the first instance, with some of the fragments ejected and some stable against accretion).

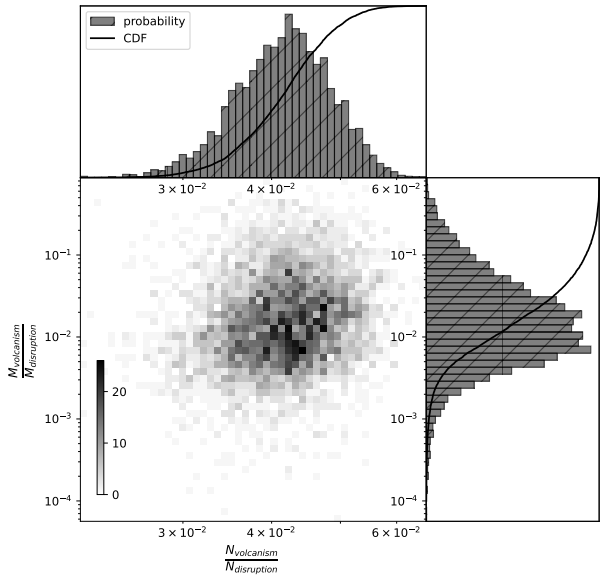

Figure 7. The simulated distribution for the frequency (x-axis) and accreted mass (y-axis) ratio of tidally induced volcanism relative to tidal disruption for $\alpha = 1$ and $\beta = -4$ and 5000 systems (each system contains 200000 sample planetesimals). Middle panel: 2D density map in frequency ratio-mass ratio space. Upper panel: probability distribution (bar chart) and the cumulative distribution (CDF, line) for frequency ratio. Right panel: same as upper panel, but for accrerted mass ratio. The probability distributions and the density map are plotted on the logarithmic scale.

We simulate the frequency and pollutant mass ratio of tidally induced volcanism to that to tidal disruption, assuming $\alpha = 1$ (an arbitrary choice accounting for the lower possibility of perturb a planetesimal closer to the white dwarf Rodet & Lai 2024), with a larger α making tidally induced volcanism more preferred) and $\beta = -4$ (Dohnanyi 1969; Gáspár et al. 2012; Pan & Schlichting 2012), with a larger β making tidally induced volcanism more preferred. We plot

the simulated distribution of $\frac{N_{volcanism}}{N_{disruption}}$ and $\frac{M_{volcanism}}{M_{disruption}}$ on the logarithmic scale (order of magnitude comparison) in Fig.7. Under our model, tidal disruption is usually more than 10 times more frequent than tidally induced volcanism. Compared to the frequency ratio, the ratio of mass delivery of volcanism to that of tidal disruption spans a much wider order of magnitude (10^{-4}–1).

Note that we minimize the free parameters required for simulations and hence neglect various complexities in the tidal disruption-tidally induced volcanism scenario, for instance, the correlation between planetesimal size/density and tensile strength, volcanic ejection speed, the geological constraints on volcanism, the dynamics of tidally disrupted disks. Furthermore, many of the free parameters/distributions remain poorly constrained. The computations of mass ratio $\frac{M_{volcanism}}{M_{disruption}}$ involves more assumptions and are hence less certain compared to the frequency ratio $\frac{N_{volcanism}}{N_{disruption}}$. The occurrence of tidally induced volcanism is not a sufficient condition for transits, as other conditions, for instance, transit probability, dust production rate, must be accounted for.

The volcanic activities we are familiar with, for instance, the volcanism on Io and Earth, are silicate volcanism. Assuming this is the case for exoplanetary bodies, tidally induced volcanism will shift the white dwarf pollutants towards mantle-rich. On the other hand, as is discussed in Abrahams & Nimmo 2019; Johnson et al. 2020, for a differentiated planetesimal with thin/no rocky mantle, a top-down solidification of the iron core can result in significant pressure growth in the iron magma ocean, which in turn induces dike formation and eruptions. The quiescent duration of Iron volcanism is controlled by strain accumulation during solidification. The time interval between two iron volcanism active periods, according to the calculations of Abrahams & Nimmo 2019 for a 100 km planetesimal is of the order of magnitude 1000 yr, which is unlikely the major cause of successive transit-active periods within a short time-span (unless the volcanism is long-lasting), for instance, those of WD 1145+017.

We are yet unable to confirm whether tidally induced volcanism tends to enhance the total mass delivered to the white dwarf. On one hand, tidally induced volcanism expands the pericentre distance range where the planetary material can be accreted by the white dwarf, and save planetesimals from being ejected from the system. On the other hand, the efficiency of mass delivery for tidal disruption and tidally induced volcanism remains unknown, and could be much higher for tidal disruption.

4.3 The importance of additional processes

Tidally induced volcanism does not occur in isolation. There are many other accompany physical processes, some of which may enhance the observed signatures, whilst other disrupt them.

First, general relativistic precession is important both for the planetsimals' orbit and for the orbit of dust released. The precession period of a planetesimal avoiding tidal disruption is usually too long for observations ($\gtrsim$ 100 yr for the planetesimal around WD 1145+017, see Appendix Q). On the other hand, a precessing accretion disk much closer to the white dwarf ($\lesssim 0.1\,R_{\odot}$, where sublimation may play a major role) may mimic a $\sim$ 100 day transit period.

Second, collisions among tidally evolving planetesimals may both lead to transit (dust production, trigger volcanism by inducing stress, producing fracture, and supplying heat) and prevent long-term transits (destructive collisions). We estimate the collision rate of tidally evolving planetesimals (see Appendix R), finding out that less than one collision is expected per Myr under our model. Collisions for planetesimals undergoing tidal evolution are mostly destructive (high encounter speed), ruling out collision-induced volcanism. Therefore, although occasional destructive collisions may produce a high level of dust, we do not consider collisions among planetesimals a major cause of transits due to its low frequency. However, we acknowledge the possibility that a planetesimal may interact with an existing disk directly (collisions) or indirectly (gravitational perturbations), triggering disk activities that may be observed as transits, with the periodicity of disk activities potentially correlated with the orbital period of the planetesimal.

Third, tidally induced volcanism is usually accompanied with planetesimal property variations, potentially altering the strength and rheology of the planetesimal, thus changing the conditions of tidal disruption. As a result, tidal disruption may be re-triggered under the action of tidal interactions and volcanism, due to spin-up and/or weakening strength.

Fourth, if the planetesimal undergoes rapid tidal circularization when the white dwarf remains luminous, the tidal flux and/or stellar irradiation may be strong enough to cause surface melting/sublimation (although not a common representative of the population, see Section 4.1.2) (Vanderburg et al. 2015). With volcanism changing the surface condition of dust particles (e.g., more loosely detached), sublimation may enhance the escape of volcanic dust from the planetesimal and/or the formation of dust coma. Sublimation and volcanism can equivalently lead to high speed ejecta leaving the planetesimal.

Notably, assuming a Maxwell-Boltzmann distribution of sublimated forsterite, the speed distribution effectively truncates at $\sim$ 1000 m/s for the irradiation experienced by the planetesimal around WD 1145+017, thus making sublimation degenerate with tidally induced volcanism in terms of the ejection speed. The key differences between sublimation and tidally induced volcanism might be the stochasticity (with tidally induced volcanism being more stochastic in the magnitude of emission and ejection velocity while sublimation being more continuous), the correlation with stellar irradiation (with sublimation require strong stellar irradiation and hence strong positive correlation between incident irradiation and the presence of transits/transit depth/activity level), and the lifetime of the secondary transits (distinct dynamics due to different particle sizes). On the other hand, tidally induced volcanism may possess intrinsic periodicity in activities (nearly constant interval between two volcanically active periods) controlled by, for instance, the magma chamber refilling time (Dobretsov 2015).

The tidally induced volcanism scenario is complex, involving various physics. However, these processes are unlikely to diminish/outweigh the features of tidally induced volcanism.

4.4 Different models for the origin of transits

Tidally induced volcanism described in this paper provides a self-consistent explanation for planetesimals to both arrive at the observed transit periods (tidal decay) and to produce the transits (volcanism).

Meanwhile, there exist other models to explain transits and are not necessarily exclusive to tidally induced volcanism:

- Sublimation under sufficient irradiation (Vanderburg et al. 2015).
- Fragments leaving the planetesimal at L1 point undergoing further sublimation (Rappaport et al. 2016).
- Partial tidal disruption of a differentiated planetesimal's mantle (Veras et al. 2017; Duvvuri et al. 2020).
- Rotational fission of triaxial planetesimal due to exchange of

spin and orbital angular momentum, potentially undergoing rotational fission (Veras et al. 2020).

Each theory has their specific constraints on the properties of the planetesimal and/or white dwarf while the probability of lying in the parameter space of a given model remains mystery. For instance, tidally induced volcanism requires a planetesimal composition/rheology where strong tidal interactions are induced and volcanism is favoured, with the conditions essential for other theories, e.g., strong stellar irradiation for sublimation, not necessary. Meanwhile, different theories may lead to distinct interpretations of the transit features. For instance, partial tidal disruption and sublimation are more inclined to continuous processes, thus requiring further modeling for the stochastic nature of the observed transits if not of observational origin (e.g., the large variability, presence and disappearance of transits around WD 1145+017). Compared to more energetic processes such as sublimation and tidally induced volcanism, partial tidal disruption and rotational fission leads to smaller orbit dispersion (see Veras et al. 2017, 2020 for the filling time), hence requiring additional dispersion mechanisms when dealing with large transit depth. On the other hand, similar to the case of Io, high temperature processes such as sublimation and tidally induced volcanism may produce plasma, where the white dwarf magnetic field can alter the subsequent orbital evolution of the ejecta, which must be accounted for when matching the model to observations. Finally, all theories listed above, including tidally induced volcanism, are more inclined to increase the silicate abundances of white dwarf pollutants (a mantle/crust–core mass loss sequence).

There exist various mechanisms to explain the transits around white dwarfs, potentially with distinct parameter space preferences, characteristic features, and may work concurrently (see Section 4.3).

5 CONCLUSIONS

Evolution of planetary systems around white dwarfs are crucial for understanding the arrival of planetary material onto the white dwarf. Transits of a handful of polluted white dwarfs reveal the rich dynamics of clos-in planetary material.

In this work, we propose a scenario where large planetesimals gravitationally perturbed just outside the Roche limit potentially undergo rapid tidal evolution, where orbital decay, circularization and tidal heating take place. Tidal heating may trigger volcanism, on orbits ranging from long-period highly eccentric orbits to short-period near circular orbits. Tidally induced volcanism, although potentially less common than tidal disruption ($\lesssim 10\%$), may lead to dramatic observable signatures like transits, where the ejected dust that is initially optically thick blocks the white dwarf. Tidally induced volcanism may work alongside with tidal disruption in delivering planetary material to the white dwarf, increasing the abundances of mantle-rich material in white dwarf pollutants. This model can broadly match the transit duration, transit depth, 180° phase shift of the primary transit of WD 1145+017, as well as the range of secondary transits. On the other hand, to match the predicted mass loss rate required for transits around WD 1145+017, a large body ($R_p \gtrsim 100$ km) is required. This model predicts short-period transits (hour–day) are more concentrated on a single orbital period, whilst longer-period (days–hundreds of days) transits could have much higher dispersion in the orbital period. However, more comprehensive modelings for the thermal, rheological, tidal evolution of the planetesimal as well as the evolution of volcanic ejecta are required for a better understanding of this scenario.

ACKNOWLEDGEMENTS

AB acknowledges the support of a Royal Society University Research Fellowship, URF\R1\211421. YL acknowledges the support of a STFC studentship.

DATA AVAILABILITY

Codes and data used in this work are available upon reasonable request to the author, Yuqi Li.

REFERENCES

Abrahams J. N. H., Nimmo F., 2019, Geophys. Res. Lett., 46, 5055
Ahles A. A., Emery J. D., Dunand D. C., 2021, Acta Astronautica, 189, 465
Alonso R., Rappaport S., Deeg H. J., Palle E., 2016, A&A, 589, L6
Bagheri A., et al., 2022, Advances in Geophysics, 63, 231
Barnes R., 2017, Celestial Mechanics and Dynamical Astronomy, 129, 509
Beaugé C., Nesvorný D., 2012, ApJ, 751, 119
Becklin E. E., Farihi J., Jura M., Song I., Weinberger A. J., Zuckerman B., 2005, ApJ, 632, L119
Beuthe M., 2013, Icarus, 223, 308
Bochkarev K. V., Rafikov R. R., 2011, ApJ, 741, 36
Bolmont E., Raymond S. N., Leconte J., 2011, A&A, 535, A94
Bolmont E., Demory B. O., Blanco-Cuaresma S., Agol E., Grimm S. L., Auclair-Desrotour P., Selsis F., Leleu A., 2020, A&A, 635, A117
Bonsor A., Wyatt M. C., 2012, MNRAS, 420, 2990
Bonsor A., Augereau J. C., Thébault P., 2012, A&A, 548, A104
Bonsor A., Farihi J., Wyatt M. C., van Lieshout R., 2017, MNRAS, 468, 154
Boué G., Efroimsky M., 2019, Celestial Mechanics and Dynamical Astronomy, 131, 30
Burke C. J., 2008, ApJ, 679, 1566
Butwin M. K., von Löwis S., Pfeffer M. A., Thorsteinsson T., 2019, Journal of Aerosol Science, 128, 99
Clausen N., Tilgner A., 2015, A&A, 584, A60
Colucci S., de' Michieli Vitturi M., Neri A., Palladino D., 2014, Earth and Planetary Science Letters, 404, 98
Croll B., et al., 2017, ApJ, 836, 82
Davidsson B. J. R., 1999, Icarus, 142, 525
Davies A. G., Perry J. E., Williams D. A., Nelson D. M., 2024, Nature Astronomy, 8, 94
Dobretsov N., 2015, Russian Geology and Geophysics, 56, 1663
Dohnanyi J. S., 1969, J. Geophys. Res., 74, 2531
Dong J., et al., 2021, ApJ, 920, L16
Duvvuri G. M., Redfield S., Veras D., 2020, ApJ, 893, 166
Farhat M., Auclair-Desrotour P., Boué G., Lichtenberg T., Laskar J., 2025, ApJ, 979, 133
Farihi J., 2016, New Astron. Rev., 71, 9
Farihi J., Jura M., Zuckerman B., 2009, ApJ, 694, 805
Farihi J., Jura M., Lee J. E., Zuckerman B., 2010, ApJ, 714, 1386
Farihi J., et al., 2022, MNRAS, 511, 1647
Fellay L., Pezzotti C., Buldgen G., Eggenberger P., Bolmont E., 2023, A&A, 669, A2
Gänsicke B. T., Marsh T. R., Southworth J., 2007, MNRAS, 380, L35
Gänsicke B. T., et al., 2016, ApJ, 818, L7
Gary B. L., Rappaport S., Kaye T. G., Alonso R., Hambschs F. J., 2017, MNRAS, 465, 3267
Gáspár A., Psaltis D., Rieke G. H., Özel F., 2012, ApJ, 754, 74
Geissler P. E., McEwen A. S., Ip W., Belton M. J. S., Johnson T. V., Smyth W. H., Ingersoll A. P., 1999, Science, 285, 870
Glanz H., Rozner M., Perets H. B., Grishin E., 2022, ApJ, 931, 11
Guidry J. A., et al., 2021, ApJ, 912, 125
Hansen B. M. S., 2012, ApJ, 757, 6
Heller R., Leconte J., Barnes R., 2011, A&A, 528, A27
Hut P., 1981, A&A, 99, 126
Ibgui L., Burrows A., Spiegel D. S., 2010, ApJ, 713, 751

Johansen A., Ronnet T., Schiller M., Deng Z., Bizzarro M., 2023, A&A, 671, A74
Johnson B. C., Sori M. M., Evans A. J., 2020, Nature Astronomy, 4, 41
Jura M., Farihi J., Zuckerman B., 2007, ApJ, 663, 1285
Jura M., Farihi J., Zuckerman B., 2009, AJ, 137, 3191
Kawahara H., Hirano T., Kurosaki K., Ito Y., Ikoma M., 2013, ApJ, 776, L6
Kepler S. O., Kleinman S. J., Nitta A., Koester D., Castanheira B. G., Giovannini O., Costa A. F. M., Althaus L., 2007, MNRAS, 375, 1315
Kepler S. O., Koester D., Romero A. D., Ourique G., Pelisoli I., 2017, in Tremblay P. E., Gaensicke B., Marsh T., eds, Astronomical Society of the Pacific Conference Series Vol. 509, 20th European White Dwarf Workshop. p. 421 (arXiv:1610.00371), doi:10.48550/arXiv.1610.00371
Kervazo M., Tobie G., Choblet G., Dumoulin C., Běhounková M., 2022, Icarus, 373, 114737
Kilic M., von Hippel T., Leggett S. K., Winget D. E., 2005, ApJ, 632, L115
Kilic M., von Hippel T., Leggett S. K., Winget D. E., 2006, ApJ, 646, 474
Koester D., Gänsicke B. T., Farihi J., 2014, A&A, 566, A34
Lai S., et al., 2021, ApJ, 920, 156
Lambeck K., 1977, Philosophical Transactions of the Royal Society of London Series A, 287, 545
Leconte J., Chabrier G., Baraffe I., Levrard B., 2010, A&A, 516, A64
Lesher C. E., Spera F. J., 2015, in Sigurdsson H., ed., , The Encyclopedia of Volcanoes (Second Edition), second edition edn, Academic Press, Amsterdam, pp 113–141, doi:https://doi.org/10.1016/B978-0-12-385938-9.00005-5, https://www.sciencedirect.com/science/article/pii/B9780123859389000055
Levrard B., Correia A. C. M., Chabrier G., Baraffe I., Selsis F., Laskar J., 2007, A&A, 462, L5
Li Y., Bonsor A., Shorttle O., Rogers L. K., 2025, Monthly Notices of the Royal Astronomical Society, 537, 2214
Lichtenberg T., Drążkowska J., Schönbächler M., Golabek G. J., Hands T. O., 2021, Science, 371, 365
Liggins P., Jordan S., Rimmer P. B., Shorttle O., 2023, Journal of Geophysical Research (Planets), 128, e2022JE007528
Lopes R. M., Williams D. A., 2015, in Sigurdsson H., ed., , The Encyclopedia of Volcanoes (Second Edition), second edition edn, Academic Press, Amsterdam, pp 747–762, doi:https://doi.org/10.1016/B978-0-12-385938-9.00043-2, https://www.sciencedirect.com/science/article/pii/B9780123859389000432
Lu T., Rein H., Tamayo D., Hadden S., Mardling R., Millholland S. C., Laughlin G., 2023, ApJ, 948, 41
Macedonio G., Neri A., Martì J., Folch A., 2005, Journal of Volcanology and Geothermal Research, 143, 153
Makarov V. V., Efroimsky M., 2013, ApJ, 764, 27
Malamud U., Grishin E., Brouwers M., 2021, MNRAS, 501, 3806
Manser C. J., et al., 2024, MNRAS, 531, L27
Matsumura S., Peale S. J., Rasio F. A., 2010, ApJ, 725, 1995
McEwen A. S., Soderblom L. A., 1983, Icarus, 55, 191
McEwen A. S., et al., 1998, Science, 281, 87
Melis C., Jura M., Albert L., Klein B., Zuckerman B., 2010, ApJ, 722, 1078
Mestel L., 1952, MNRAS, 112, 583
Metzger B. D., Rafikov R. R., Bochkarev K. V., 2012, MNRAS, 423, 505
Miller N., Fortney J. J., Jackson B., 2009, ApJ, 702, 1413
Moe M., Kratter K. M., 2018, ApJ, 854, 44
Mommert M., McNeill A., Trilling D. E., Moskovitz N., Delbo' M., 2018, AJ, 156, 139
Mustill A. J., Villaver E., Veras D., Gänsicke B. T., Bonsor A., 2018, MNRAS, 476, 3939
Neron de Surgy O., Laskar J., 1997, A&A, 318, 975
Noyelles B., Frouard J., Makarov V. V., Efroimsky M., 2014, Icarus, 241, 26
Noyes C. S., Consolmagno G. J., Macke R. J., Britt D. T., Opeil C. P., 2022, Meteoritics & Planetary Science, 57, 1706
O'Brien M. W., et al., 2023, MNRAS, 518, 3055
O'Brien M. W., et al., 2024, MNRAS, 527, 8687
O'Connor C. E., Lai D., 2020, MNRAS, 498, 4005
O'Connor C. E., Teyssandier J., Lai D., 2022, MNRAS, 513, 4178
Opeil C., Consolmagno G., Britt D., 2010, Icarus, 208, 449
Osman S., Beckett F., Rust A., Snee E., 2020, Atmosphere, 11
Ostrowski D., Bryson K., 2019, Planet. Space Sci., 165, 148
Pan M., Schlichting H. E., 2012, ApJ, 747, 113
Park R., et al., 2025, Nature, 638, 69
Pohl L., Britt D. T., 2020, Meteoritics & Planetary Science, 55, 962
Press W. H., Teukolsky S. A., 1977, ApJ, 213, 183
Quirrenbach A., 2022, Research Notes of the American Astronomical Society, 6, 56
Rafikov R. R., 2011a, MNRAS, 416, L55
Rafikov R. R., 2011b, ApJ, 732, L3
Rappaport S., Barclay T., DeVore J., Rowe J., Sanchis-Ojeda R., Still M., 2014, ApJ, 784, 40
Rappaport S., Gary B. L., Kaye T., Vanderburg A., Croll B., Benni P., Foote J., 2016, MNRAS, 458, 3904
Rathbun J. A., Spencer J. R., Davies A. G., Howell R. R., Wilson L., 2002, Geophys. Res. Lett., 29, 1443
Rathbun J. A., Lopes R. M. C., Spencer J. R., 2018, AJ, 156, 207
Rein H., Liu S. F., 2012, A&A, 537, A128
Renggli C., King P., Henley R., Norman M., 2017, Geochimica et Cosmochimica Acta, 206, 296
Ricard Y., Šrámek O., Dubuffet F., 2009, Earth and Planetary Science Letters, 284, 144
Rodet L., Lai D., 2024, MNRAS, 527, 11664
Rogers L. K., et al., 2024, MNRAS, 527, 6038
Rozner M., Glanz H., Perets H. B., Grishin E., 2022, ApJ, 931, 10
Rufu R., Canup R. M., 2020, Journal of Geophysical Research (Planets), 125, e06312
Sánchez M. B., de Elía G. C., Downes J. J., 2020, A&A, 637, A78
Sanchis-Ojeda R., et al., 2015, ApJ, 812, 112
Scheinberg A., Fu R. R., Elkins-Tanton L. T., Weiss B. P., 2015, in Michel P., DeMeo F. E., Bottke W. F., eds, , Asteroids IV. University of Arizona Press, pp 533–552, doi:10.2458/azu_uapress_9780816532131-ch028
Seligman D. Z., et al., 2024, ApJ, 961, 22
Simon J. B., Armitage P. J., Li R., Youdin A. N., 2016, ApJ, 822, 55
Simon J. B., Armitage P. J., Youdin A. N., Li R., 2017, ApJ, 847, L12
Spencer J. R., et al., 2007, Science, 318, 240
Steinberg G., Babenko J., 1978, Journal of Volcanology and Geothermal Research, 3, 89
Storch N. I., Lai D., 2014, MNRAS, 438, 1526
Taddeucci J., et al., 2021, Geophysical Research Letters, 48, e2021GL092899
Tingley B., Sackett P. D., 2005, ApJ, 627, 1011
Tobie G., Mocquet A., Sotin C., 2005, Icarus, 177, 534
Tremblay P. E., Cummings J., Kalirai J. S., Gänsicke B. T., Gentile-Fusillo N., Raddi R., 2016, MNRAS, 461, 2100
Tyler R. H., Henning W. G., Hamilton C. W., 2015, ApJS, 218, 22
Vanderbosch Z., et al., 2020, ApJ, 897, 171
Vanderbosch Z. P., et al., 2021, ApJ, 917, 41
Vanderburg A., Rappaport S. A., 2018, in Deeg H. J., Belmonte J. A., eds, , Handbook of Exoplanets. Springer International Publishing, p. 37, doi:10.1007/978-3-319-55333-7_37
Vanderburg A., et al., 2015, Nature, 526, 546
Veras D., 2016, Royal Society Open Science, 3, 150571
Veras D., 2020, MNRAS, 493, 4692
Veras D., Fuller J., 2019, MNRAS, 489, 2941
Veras D., Fuller J., 2020, MNRAS, 492, 6059
Veras D., Leinhardt Z. M., Bonsor A., Gänsicke B. T., 2014, MNRAS, 445, 2244
Veras D., Leinhardt Z. M., Eggl S., Gänsicke B. T., 2015, MNRAS, 451, 3453
Veras D., Carter P. J., Leinhardt Z. M., Gänsicke B. T., 2017, MNRAS, 465, 1008
Veras D., et al., 2019, MNRAS, 486, 3831
Veras D., McDonald C. H., Makarov V. V., 2020, MNRAS, 492, 5291
Veras D., Birader Y., Zaman U., 2022, MNRAS, 510, 3379
Veras D., Georgakarakos N., Dobbs-Dixon I., 2023, MNRAS, 518, 4537
Vick M., Lai D., 2020, MNRAS, 496, 3767
Vick M., Lai D., Anderson K. R., 2019, MNRAS, 484, 5645
Vick M., Su Y., Lai D., 2023, ApJ, 943, L13
Wang L., Zhang X., Wang J., Zhang Z.-X., Fang T., Gu W.-M., Guo J., Jiang X., 2023, ApJ, 944, 23

Wilson T. G., Farihi J., Gänsicke B. T., Swan A., 2019, MNRAS, 487, 133
Woods A. W., Bower S. M., 1995, Earth and Planetary Science Letters, 131, 189
Wyatt S. P., Whipple F. L., 1950, ApJ, 111, 134
Xu S., Jura M., Pantoja B., Klein B., Zuckerman B., Su K. Y. L., Meng H. Y. A., 2015, ApJ, 806, L5
Xu S., Jura M., Dufour P., Zuckerman B., 2016, ApJ, 816, L22
Xu S., Lai S., Dennihy E., 2020, ApJ, 902, 127
Zahnle K. J., Lupu R., Dobrovolskis A., Sleep N. H., 2015, Earth and Planetary Science Letters, 427, 74
Zuckerman B., Becklin E. E., 1987, Nature, 330, 138
Zuckerman B., Koester D., Reid I. N., Hünsch M., 2003, ApJ, 596, 477
Zuckerman B., Melis C., Klein B., Koester D., Jura M., 2010, ApJ, 722, 725
van Lieshout R., Min M., Dominik C., 2014, A&A, 572, A76
van Lieshout R., et al., 2016, A&A, 596, A32

This paper has been typeset from a TEX/LATEX file prepared by the author.

Appendices

Yuqi Li

June 26, 2025

A Orbital energy dissipation

We expand the tidal power $\dot{E}_t$ at high and low eccentricities for $\frac{q_0}{Q_0} \to 0$:

$$\frac{dE_t}{dt}(e \to 1) \approx 0.19819 G^2 M_p M_* T_p q_0^{-7.5} Q_0^{-1.5}, \tag{A1}$$

$$\frac{dE_t}{dt}(e \to 0) \approx 0.006836 G^2 M_p M_* T_p q_0^{-9} e^2. \tag{A2}$$

Along the tidal evolution track, the maximum of tidal power ($\frac{dE_t}{dt}$) is determined by that of $e^2(1-e^2)^{\frac{3}{2}}F(e)$, at $e = e_{max} \approx 0.735$:

$$\frac{dE_t}{dt}(e = e_{max}) \approx 0.002363 M_p M_* T_p q_0^{-9}. \tag{A3}$$

The accumulated tidal energy when a planetesimal starting at (q_0, Q_0) ($e_0 = \frac{Q_0 - q_0}{Q_0 + q_0}$) reaches an eccentricity e is given by:

$$\Delta E_t = \frac{G M_p M_* (q_0 + Q_0)}{4 q_0 Q_0} \left[\left(\frac{Q_0 - q_0}{Q_0 + q_0} \right)^2 - e^2 \right]. \tag{A4}$$

We approximate the energy required for melting as $c_p M_p \Delta T_c$, such that $e_0 - e \sim (e_0 - e)e_0 < e_0^2 - e^2 = \frac{4 q_0 Q_0}{q_0 + Q_0} \frac{c_p \Delta T_c}{G M_*} \sim 2 \times 10^{-4} \frac{q_0}{0.01\,\mathrm{AU}} \frac{c_p}{1000\,\mathrm{J/(K{\cdot}kg)}} \frac{\Delta T_c}{3000\,\mathrm{K}} \frac{0.6\,M_\odot}{M_*}$. Hence, eccentricity decay is negligible as the accumulated tidal energy reaches the melting energy for the parameters we consider. It is reasonable to approximate the melting time t_{melt} using:

$$t_{melt} \sim \frac{c_p M_p \Delta T_c}{\dot{E}_{t,0}}. \tag{A5}$$

The cooling timescale t_{cool} is approximated by the diffusion timescale scaled by the Nusselt number (Nu, the ratio of total heat loss rate to conductive heat loss rate):

$$t_{cool} \sim \frac{R_p^2}{\pi^2 \alpha_d \mathrm{Nu}} \sim \frac{R_p^2 \rho_p c_p}{\pi^2 \kappa \mathrm{Nu}}. \tag{A6}$$

$\frac{t_{melt}}{t_{cool}}$ can hence be approximated as:

$$\frac{t_{melt}}{t_{cool}} \sim 208.6 \frac{\kappa \mathrm{Nu} \Delta T_c q_0^{7.5} Q_0^{1.5}}{G^2 K_p M_*^3 R_p^4}. \tag{A7}$$

B Critical energy of melting

In this section, we estimate the temperature representation of the melting energy with respect to a fixed specific heat capacity c_p, ΔT_c, such that $\bar{c}_p M_p \Delta T_c$ is the critical energy of melting (we will refer to the constant specific capacity as $\bar{c}_p$ in this section). For a temperature dependent heat capacity, $c_p(T)$, a specific enthalpy of fusion Δh_f, and a critical temperature of melting T_c, we have:

$$\Delta T_c = \frac{\int_{T_0}^{T_c} c_p(T) dT + \Delta h_f}{\bar{c}_p}, \tag{B1}$$

where T_0 is the initial temperature of the planetesimal. We use the empirical relation of $c_p(T)$ for forsterite (Gillet et al., 1991):

$$c_p(T) = -2863 + 528 \ln T + \frac{623 \times 10^3}{T} - \frac{184 \times 10^6}{T^2} + \frac{180 \times 10^8}{T^3}, \tag{B2}$$

with the heat capacity in SI unit (J/(K·kg)). Note that the empirical relation has a minimum at $T \approx 206\,\mathrm{K}$, which may not be physical. Hence, we assume that $c_p(T < 206\,\mathrm{K}) = c_p(T = 206\,\mathrm{K})$. We find out that $\Delta T_c \sim 3000\,\mathrm{K}$ for $T_c \sim 2000\,\mathrm{K}$, $50\,\mathrm{K} \lesssim T_0 \lesssim 500\,\mathrm{K}$ and $\Delta h_f \sim 1000\,\mathrm{kJ/kg}$ (Lesher & Spera, 2015). The lower and upper limits of investigation for T_0 are the equilibrium temperatures a planetesimal would have if it is on a highly eccentric orbit when the host star just enters its white dwarf phase and at a cooling age $\sim 100\,\mathrm{Myr}$ (with other parameters identical to those in Table 1 in the main text).

C The Nusselt number

We use the Nusselt number Nu to quantify the total heat loss (excluding heat loss during volcanism) to conductive heat loss ratio. We constrain the range of Nu by considering parameterized convection in a partially melted solid-like mantle whose viscosity is reduced in the presence of liquid melt, with the Nusselt number given by (Solomatov, 2007; Lebrun et al., 2013; Zahnle et al., 2015):

$$\mathrm{Nu} = 0.089\mathrm{Ra}^{\frac{1}{3}}, \tag{C1}$$

with Ra the Raleigh number:

$$\mathrm{Ra} = \frac{\beta g \Delta T l^3}{\alpha_t \nu}, \tag{C2}$$

where β is the coefficient of thermal expansion, g is the gravity, ΔT is the surface temperature-critical temperature contrast, l is the length scale of convection, α_t is the thermal diffusivity, ν is the kinematic viscosity. We apply $\beta = 5 \times 10^{-5}\,\mathrm{K}^{-1}$, $\alpha_t \sim 10^{-6}\,\mathrm{m}^2/\mathrm{s}$, $\Delta T \sim 1000\,\mathrm{K}$, $gl^3 \sim \frac{4}{3}\pi G R_p^4 (1 - f_m)^3 \rho_p$. We further apply the parameterized viscosity for melt-bearing solid (Solomatov, 2007; Lebrun et al., 2013; Zahnle et al., 2015):

$$\nu = \nu_s e^{-\alpha_\nu \phi}, \tag{C3}$$

where $\nu_s \sim 10^{15}\,\mathrm{m/s}^2$, $\alpha_\nu = 26$–31. We consider the limiting case where the melt fraction ϕ of the crust just reaches the critical value $\phi \sim 0.4$, with the maximum Nu given by:

$$\begin{aligned}\mathrm{Nu} = 100 &\left(\frac{\beta}{5 \times 10^{-5}\,\mathrm{K}^{-1}} \frac{\Delta T}{2000\,\mathrm{K}} \frac{1 \times 10^{-6}\,\mathrm{m}^2/\mathrm{s}}{\alpha_t} \frac{4 \times 10^9\,\mathrm{m/s}^2}{\nu}\right)^{\frac{1}{3}} \\ &\times \left(\frac{\rho_p}{3000\,\mathrm{kg/m}^3}\right)^{\frac{1}{3}} \left(\frac{R_p}{100\,\mathrm{km}}\right)^{\frac{4}{3}} (1 - f_m),\end{aligned} \tag{C4}$$

which indicates that $\mathrm{Nu} \lesssim 10$ under the fiducial parameters and Nu can hardly exceed 100 even in the extreme case where the conduction length scale and convection length scale both equal to the size of the planetesimal.

We acknowledge that there exist other scaling relations for the Nusselt number, with which we will compare (Reese et al., 1999, 2005; Clausen & Tilgner, 2015):

$$\mathrm{Nu} = A\theta^B \mathrm{Ra}^C, \tag{C5}$$

where we apply $\theta \sim \frac{4 \times 10^4\,\mathrm{K}}{T_c^2}\Delta T$. Two sets of (A, B, C) are investigated, $(0.67, -\frac{4}{3}, \frac{1}{3})$ and $(2.51, -1.2, 0.2)$, giving slightly smaller Nu than its counterpart obtained by parametrized convection.

Hence, in the majority of the cases we have $\log_{10} \mathrm{Nu} \sim 0$–$1$.

D Alternative models for the condition of melting

The condition of melting can be quantified as the accumulated heat (tidal heating subtracted by cooling) exceeding the melting energy within the timescale we consider (1 Gyr). To quantify the cooling rate, we use the simple relation:

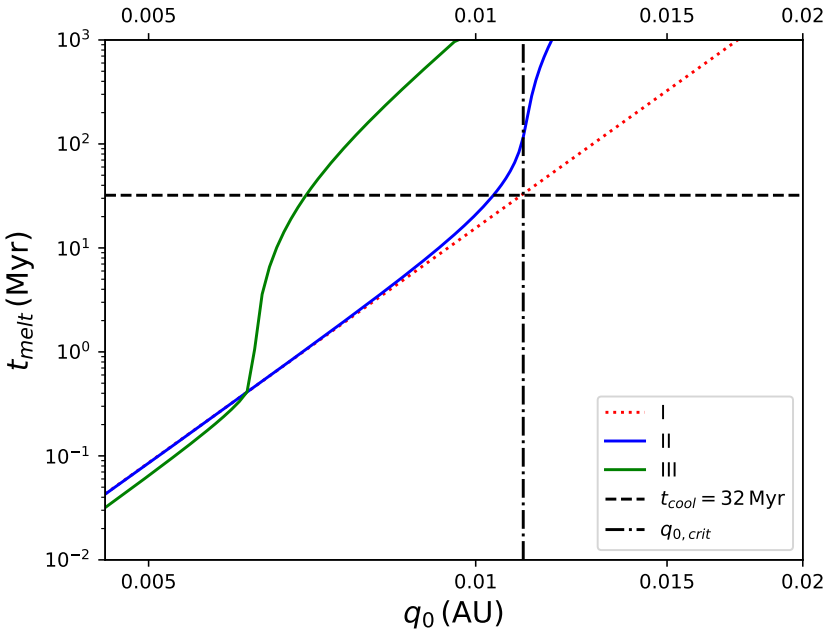

Figure D1: A comparison of the predicted melting timescale using the model presented in this section (II: blue solid line, III: green solid line) and the model in Section 2.2.1 (I, red dotted line). The critical initial pericentre distance of melting are given by the q_0 at the intersections of the lines with $t = 1$ Gyr (~ 0.0096 AU and 0.0121 AU) for model II and III, and the q_0 at the intersection of the red dotted line and $t = t_{cool}$ (~ 0.011 AU, dashdot line) for model I.

$$\dot{E}_{acc} = \dot{E}_t - \frac{E_{acc}}{t_{cool}}. \tag{D1}$$

We will consider two models of t_{cool}, model II (maximum diffusion length):

$$t_{cool} \sim \frac{R_p^2 \rho_p c_p}{\pi^2 \kappa}, \tag{D2}$$

and model III (minimum diffusion length):

$$t_{cool} \sim \frac{\left[R_p - \left(\frac{3}{4\pi\rho_p}\frac{E_{acc}}{c_p \Delta T_c}\right)^{\frac{1}{3}}\right]^2 \rho_p c_p}{\pi^2 \kappa}. \tag{D3}$$

The model in Section 2.2.1 is model I.

For melting to occur, we require that $(E_{acc})_{max} \geq c_p M_p \Delta T_c$ for model II and $(E_{acc})_{max} \geq c_p f_m^3 M_p \Delta T_c$ for model III (to avoid singularity). The corresponding melting timescale satisfies $E_{acc}(t_{melt}) = c_p M_p \Delta T_c$ and $E_{acc}(t_{melt}) = c_p f_m^3 M_p \Delta T_c$, respectively. The critical initial pericentre distance of melting $q_{0,crit}$ for model II and III is defined by the q_0 where $t_{melt} = 1$ Gyr.

We compute t_{melt} numerically and compare to model I in Fig.D1, showing that $q_{0,crit}$ computed using model II and III, ~ 0.0096 AU and ~ 0.0121 AU, are generally consistent with that of model I, ~ 0.0111 AU. However, non-negligible differences in t_{melt} may present, especially towards large q_0, where tidal heating is less dominant and the cooling model matters more. Although all of our models are for qualitative purpose only, there is a generally agreement on the critical initial pericentre distance of melting $q_{0,crit} \sim 0.01$ AU due to the strong dependence of tidal evolution on q_0 (a small change in q_0 could move the planetesimal from a cooling-dominant regime to heating dominant regime).

Model II and III generally predicts a larger parameter space for melting ($K_p \lesssim 1$ s and $R_p \lesssim 20$ km, while much larger Q_0 to rule out tidally induced melting when varying single parameter) as we no longer require melting to occur at the early tidal evolution stage before reaching the cooling timescale as is in model I.

E Cooling through a spherical shell

Assuming that the temperature profile of the planetesimal reaches a steady state where $T_c(x = f_m R_p)$ at the transition from solidus to liquidus behaviour and $T(x = R_p) = T_s$ at the surface, the radial thermal diffusion equation reduces to:

$$\kappa x^2 \frac{dT}{dx} = C, \tag{E1}$$

which, for a constant κ (can be understood as using $\bar{\kappa} = \left| \frac{\int_{T_c}^{T_s} \kappa(T) dT}{T_s - T_c} \right|$) gives:

$$T = \frac{f_m R_p}{x(1-f_m)}(T_c - T_s) + \frac{T_s - f_m T_c}{1 - f_m}, \tag{E2}$$

and the corresponding heat loss rate is:

$$\dot{Q}_l = -\kappa \mathrm{Nu}' 4\pi x^2 \frac{dT}{dx} = 4\pi\kappa \mathrm{Nu}' \frac{f_m}{1-f_m} R_p (T_c - T_s), \tag{E3}$$

where $\mathrm{Nu}' \geq 1$ is the Nusselt number accounting for additional heat loss (the 'prime' is used to remind that melting and volcanism are distinct thermal processes).

At $e \to e_0 \to 1$, the ratio of tidal power to heat loss rate ($\frac{\dot{E}_t}{\dot{Q}_l}$) is:

$$\frac{\dot{E}_t}{\dot{Q}_l} \sim 0.01577 \frac{G^2 K_p M_*^3 R_p^4}{\kappa \mathrm{Nu}' (T_c - T_s) q_0^{7.5} Q_0^{1.5}} \frac{1 - f_m}{f_m}, \tag{E4}$$

and $\frac{\dot{E}_t}{\dot{Q}_l}$ at $e \to 0$ can be approximated as:

$$\frac{\dot{E}_t}{\dot{Q}_l} \sim 0.000544 \frac{G^2 K_p M_*^3 R_p^4 e^2}{\kappa \mathrm{Nu}' (T_c - T_s) q_0^9} \frac{1 - f_m}{f_m}. \tag{E5}$$

More generally, when κ is a function of temperature, one need to solve:

$$\int \kappa(T) dT = \int \frac{C}{x^2} dx. \tag{E6}$$

For $\kappa = \frac{1}{a+bT}$ (Miao et al., 2014), we have:

$$\begin{aligned} \ln(a + bT) = & \frac{f_m R_p}{x(1-f_m)} \left[\ln(a + bT_c) - \ln(a + bT_s) \right] \\ & + \frac{1}{1-f_m} \left[\ln(a + bT_s) - f_m \ln(a + bT_c) \right], \end{aligned} \tag{E7}$$

The corresponding heat loss rate is:

$$\begin{aligned} \dot{Q}_l &= 4\pi \mathrm{Nu}' \frac{f_m}{(1-f_m)} R_p \frac{1}{b} \left[\ln(a + bT_c) - \ln(a + bT_s) \right] \\ &= 4\pi \mathrm{Nu}' \frac{f_m}{(1-f_m)} R_p \frac{1}{b} \ln \frac{\kappa(T_s)}{\kappa(T_c)}. \end{aligned} \tag{E8}$$

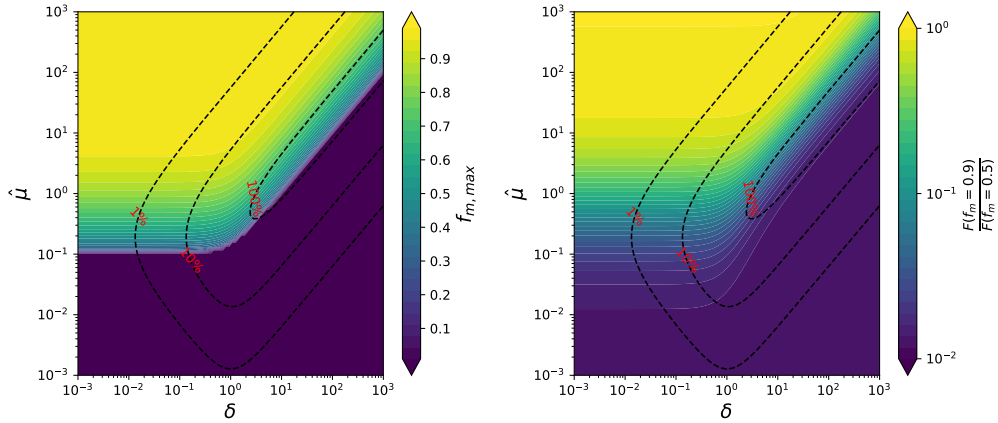

Figure F1: The f_m where $\Im(\tilde{k}_2)$ reaches its maximum (left panel), and the ratio of $F \equiv \Im(\tilde{k}_2)\frac{1-f_m}{f_m}$ at $f_m = 0.9$ to its counterpart at $f_m = 0.5$ (right panel) in δ–$\hat{\mu}$ space. The magnitude of $\Im(\tilde{k}_2)(f_m = 0.5)$ is illustrated by the contour lines normalised with respect to the 100% contour line (corresponding to $\Im(\tilde{k}_2) = 0.6$).

F Depth of magma reservoir

One estimation for the depth of magma reservoir is where the thermal stress reaches the material strength, and the magma tend to accumulate instead of propagating in the absence of excess pressure. The thermal stress is given by (Geller, 1972; Tambovtseva & Shestakova, 1999):

$$\sigma_i(r) = \frac{\alpha E}{1-\nu} T_i, \tag{F1}$$

where $i = r$ or ϕ, with σ_r the radial stress (0 at surface), σ_ϕ the tangential stress, α is the coefficient of linear expansion, E is the Young's modulus, ν is the Poisson ratio, T_i is the temperature representations of thermal stress given by:

$$T_r = \frac{2}{R_p^3}\int_0^{R_p} T(r)r^2 dr - \frac{2}{r^3}\int_0^{r} T(r)r^2 dr, \tag{F2}$$

$$T_\phi = \frac{2}{R_p^3}\int_0^{R_p} T(r)r^2 dr + \frac{1}{r^3}\int_0^{r} T(r)r^2 dr - T(r) \tag{F3}$$

We apply a simplified temperature profile (see Appendix E):

$$T(r) = \begin{cases} T_c, & r < f_m R_p \\ \frac{f_m R_p}{r(1-f_m)}(T_c - T_s) + \frac{T_s - f_m T_c}{1-f_m}, & f_m R_p < r < R_p \end{cases}, \tag{F4}$$

from which we obtain:

$$T_r = 2A - 2B(r), \tag{F5}$$

$$T_\phi = 2A + B(r) - T(r), \tag{F6}$$

where A and B for $f_m R_p \leq r \leq R_p$ are given by:

$$\begin{aligned} A &= \frac{1}{R_p^3}\int_0^{R_p} T(r) r^2 dr \\ &= \frac{1}{2}(f_m^2 + f_m)(T_c - T_s) + \frac{1}{3}(T_s - f_m T_c)(f_m^2 + f_m + 1) + \frac{1}{3} f_m^3 T_c, \end{aligned} \tag{F7}$$

$$\begin{aligned} B &= \frac{1}{r^3}\int_0^{r} T(r) r^2 dr \\ &= \frac{1}{2}\frac{f_m R_p}{(1 - f_m)}(T_c - T_s)\left(\frac{1}{r} - \frac{f_m^2 R_p^2}{r^3}\right) + \frac{1}{3}\frac{T_s - f_m T_c}{1 - f_m}\left(1 - \frac{f_m^3 R_p^3}{r^3}\right) \\ &+ \frac{1}{3}\frac{f_m^3 R_p^3}{r^3} T_c, \end{aligned} \tag{F8}$$

We investigate T_i at $r = f_m R_P$, where $B = \frac{1}{3}T_c$ and $T_r = T_\phi$. We acknowledge that there is a wide range for the free parameters: $\alpha \sim 5 \times 10^{-6}\,\mathrm{K}^{-1}$–$1 \times 10^{-5}\,\mathrm{K}^{-1}$, $\nu \sim 0.1$–0.4, $E \sim 50\,\mathrm{GPa}$–$100\,\mathrm{GPa}$, a compressive strength $-\sigma_- \sim 10\,\mathrm{MPa}$–$1000\,\mathrm{MPa}$ (Bouhifd et al., 1996; Tambovtseva & Shestakova, 1999; Gercek, 2007; Slyuta, 2017; Gouriet et al., 2019; Tanbakouei et al., 2019; Pohl & Britt, 2020; Tang et al., 2023; Shestakova & Serebryanskiy, 2023), allowing f_m to range from 0 to 1. We obtain the fiducial value of f_m using the numerical average of α, ν, E, together with $-\bar{\sigma}_- = 200\,\mathrm{MPa}$ for L chondrites (Pohl & Britt, 2020) (most data available and only data available for dynamic measurements). We obtain $f_m \lesssim 0.9$.

Another estimation for the depth of melt reservoir can be obtained by considering the viscoelastic tidal dissipation as a function of melt fraction. Based on the model in Seligman et al., 2024, we aim to locate the melt fraction corresponding to the maximum of the imaginary part of the love number ($\Im(\tilde{k}_2)$):

$$\Im(\tilde{k}_2) = \frac{3}{2}\frac{Z(f_m)\delta\hat{\mu}}{|1 + Z(f_m)\hat{\mu}|^2 + \delta^2}, \tag{F9}$$

where $\hat{\mu} = \frac{\mu}{\rho_p g R_p}$, with μ the rigidity, δ is the ratio of maxwell frequency to tidal forcing frequency. $Z(f_m)$ is given by:

$$Z(f_m) = 12\left(\frac{19 - 75f_m^3 + 112f_m^5 - 75f_m^7 + 19f_m^{10}}{24 + 40f_m^3 - 45f_m^7 - 19f_m^{10}}\right), \tag{F10}$$

which decreases monotonically with f_m from the maximum, $Z(f_m = 0) = 9.5$, to, e.g., $Z(f_m = 0.99) = 0.055$.

If $\hat{\mu}$ is small, or if δ is large and $\delta \gg \hat{\mu}$, $\Im(\tilde{k}_2)$ is proportional to $Z(f_m)$ where tidal dissipation efficiency monotonically decreases with f_m. If $\hat{\mu}$ is large and $\hat{\mu} \gg \delta$, $\Im(\tilde{k}_2)$ is inversely proportional to $Z(f_m)$ where tidal dissipation efficiency monotonically increases with f_m. In these cases, there is no maximum for $\Im(\tilde{k}_2)$. Furthermore, $\Im(\tilde{k}_2)(f_m)$ is greatly suppressed if: 1. either $\hat{\mu}$ or δ is large and orders of magnitude larger than the other and 2. either $\hat{\mu}$ or δ is small. Hence, we are mainly interested in the cases where $\hat{\mu} \sim \delta \gtrsim 1$ (see Fig.F1 for an example). We consider the special case where $\hat{\mu} = \delta$, finding out that the maximum of $\Im(\tilde{k}_2)$ occurs at $f_m \sim 0.8$, which leads to more optimistic estimation of the parameter space of volcanism compared to $f_m \sim 0.9$ obtained above. The maximum of $\Im(\tilde{k}_2)$ will shift towards larger f_m with the increase in $\frac{\hat{\mu}}{\delta}$ and vice versa, before reaching the monotonic regions.

The ascending rate of the melt frontier is proportional to $\Im(\tilde{k}_2)\frac{1}{f_m^2}$. Meanwhile, the descending rate of the melt frontier is proportional to (using Eq.E3) $\frac{1}{f_m(1-f_m)}$. Therefore, the evolution of $F \equiv \Im(\tilde{k}_2)\frac{1-f_m}{f_m}$ with f_m indicates the evolution towards heating/melting dominated regime or cooling/crystallization dominated regime. In the parameter space of large $\Im(\tilde{k}_2)$, we find order(s) of magnitude decay in F when the melt frontier ascends from $f_m = 0.5$ to $f_m = 0.9$, such that the propagation rate of the melt frontier towards the surface is significantly suppressed.

In summary, we consider $f_m = 0.9$ as a reasonable trial value for the depth of melt frontier.

G The ejection speed of volcanic flow

We estimate the volcanic ejection speed under the 1-D conduit model and choked flow condition (Wilson et al., 1980; Woods & Bower, 1995; Koyaguchi, 2005; Gonnermann & Manga, 2013).

The continuity equation assuming a constant vent cross-sectional area is:

$$\frac{d(\rho u)}{dz} = 0, \tag{G1}$$

where u is magma velocity. By using the fact that $\frac{d\rho}{dz} = \frac{d\rho}{dP}\frac{dP}{dz}$, Eq.G1 can be written as:

$$u\frac{d\rho}{dP}\frac{dP}{dz} + \rho\frac{du}{dz} = 0, \tag{G2}$$

where $\frac{d\rho}{dP} = \frac{1}{c_s^2}$ with c_s the isothermal sound speed.

The momentum equation is:

$$\rho u \frac{du}{dz} = -\frac{dP}{dz} - \rho g - f, \tag{G3}$$

with f the friction force. Eq.G3 can be combined with Eq.G2 to give:

$$(1 - \frac{u^2}{c_s^2})\frac{dP}{dz} = -\rho g - f, \tag{G4}$$

from which one can deduce that $u \leq c_s$ for $\frac{dP}{dz} \leq 0$. Therefore, it is reasonable to approximate the maximum vent exit speed using the sound speed (choked flow condition).

To derive the isothermal speed of sound, we combine Eq.G1 and Eq.G3 as:

$$-u^2 \frac{d\rho}{dz} = -\frac{dP}{dz} - \rho g - f. \tag{G5}$$

The density of gas-magma mixture ρ can be expressed as:

$$\frac{1}{\rho} = \frac{1-n}{\sigma} + \frac{nRT}{P}, \tag{G6}$$

where σ is magma density, P is pressure, R is specific gas constant, n is the gas mass fraction, which can be related to the gas mass fraction at zero pressure n_0 as:

$$n = n_0 - C, \tag{G7}$$

where the mass fraction of dissolved gas C is:

$$C = sP^{\beta} \tag{G8}$$

with s the saturation constant. β and s depends on the type of dissolved gas.

Differentiating Eq.G6 gives:

$$-\frac{1}{\rho^2}\frac{d\rho}{dz} = -\frac{1}{\sigma}\frac{dn}{dz} + \frac{RT}{P}\frac{dn}{dz} - \frac{nRT}{P^2}\frac{dP}{dz}, \tag{G9}$$

where

$$\frac{dn}{dz} = -\frac{dC}{dz} = -\beta\frac{C}{P}\frac{dP}{dz}, \tag{G10}$$

and hence

$$\frac{d\rho}{dz} = -\rho^2 \left(\frac{\beta C}{P\sigma} - \frac{\beta CRT}{P^2} - \frac{nRT}{P^2} \right) \frac{dP}{dz}. \tag{G11}$$

Eq.G5 can be written as:

$$\left[1 - \frac{u^2\rho^2}{P^2} \left(n_0 RT + (\beta - 1)CRT - \frac{\beta CP}{\sigma} \right) \right] \frac{dP}{dz} = -\rho g - f, \tag{G12}$$

which, by comparing with Eq.G4, indicates that the sound speed c_s is:

$$c_s = \sqrt{n_0 RT} \left[1 + \frac{(1-n)P}{nRT\sigma} \right] \frac{n}{\sqrt{n_0}\sqrt{n_0 + (\beta - 1)C - \frac{\beta CP}{\sigma RT}}}. \tag{G13}$$

One may notice that for the last term in the square root, $\frac{\beta CP}{\sigma RT} = \frac{\beta C \rho_{gas}}{\sigma} \ll \beta C \leq \beta n_0$ should generally hold. As we do not expect β to be a large number (where solubility boosts with pressure), $\frac{\beta CP}{\sigma RT} \ll n_0$ should hold and one can neglect this term. We expect that the majority of the gas is exsolved at vent exit ($C \ll n_0$), and hence $\frac{n}{\sqrt{n_0}\sqrt{n_0+(\beta-1)C}} \sim 1$ (vent exit not at high pressure). On the other hand, the term $\frac{(1-n)P}{nRT\sigma}$ is equivalent to $\frac{V_{magma}}{V_{gas}}$, which is supposed to be small at vent exist (Bercovici & Michaut, 2010; La Spina et al., 2022). Therefore, $c_s \sim \sqrt{n_0 RT}$ should generally hold.

After vent exit, the excess pressure of the flow relative to the ambient leads to decompression (Woods & Bower, 1995). The continuity equation implies that:

$$\rho_v u_v A_v = \rho_a u_a A_a, \tag{G14}$$

where the subscript 'v' represents the vent exit and 'a' represents decompression to the ambient, A is the cross-sectional area. The momentum equation becomes:

$$\rho_a u_a^2 A_a - \rho_v u_v^2 A_v = p_v A_v + p_a (A_a - A_v) - p_a A_a. \tag{G15}$$

The speed after decompression can then be expressed as:

$$u_a = u_v + \frac{P_v - P_a}{\rho_v u_v} \sim 2\sqrt{n_0 RT}, \tag{G16}$$

where we apply $u_v \sim c_s \sim \sqrt{n_0 RT}$ and $\rho_v \sim \frac{P_v}{n_0 RT}$ at vent exit.

To sum up, the volcanic ejection speed is of the order of magnitude $\sqrt{n_0 RT}$, or:

$$u_{eject} \sim 3000 \sqrt{\frac{n_0}{\mu_m} \frac{T}{1000\,\mathrm{K}}}\ \mathrm{m/s}, \tag{G17}$$

where μ_m is the (relative) mean molecular mass of gas in the flow.

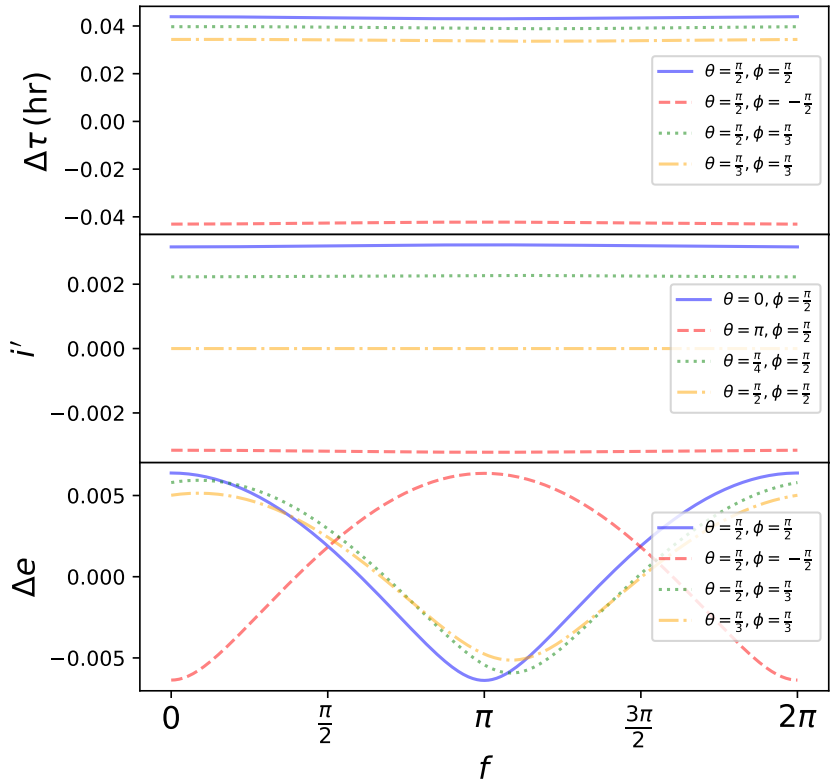

Figure H1: The orbital period (upper panel), orbital inclination (middle panel) and eccentricity dispersion (lower panel) relative to the the planetesimal with $R_p = 100\,\mathrm{km}$ and $\rho_P = 6000\,\mathrm{kg/m^3}$ on a 4.5 hr period with $e = 0.01$ around WD 1145+017, as a function of true anomaly (f) for four sets of ejection angles (note the different choices for i', the middle panel). The ejection speed is assumed to be 1000 m/s.

H Computations of orbit dispersion

An order of magnitude approximation for $\Delta\bar{e} = \bar{e}' - \bar{e}$ assuming a near circular orbit is:

$$\begin{aligned}\Delta\bar{e} \approx \sin\theta &\left[(S+2)\frac{R_p}{a}\cos\phi + \frac{2u_{eject}}{v_{orb}}\sin\phi\right]\hat{i} \\ + \sin\theta &\left[(S-1)\frac{R_p}{a}\sin\phi - \frac{u_{eject}}{v_{orb}}\cos\phi\right]\hat{j},\end{aligned} \tag{H1}$$

which approaches 0 when ejection occurs at the poles of the planetesimal ($\sin\theta = 0$, where only second-order effects remain). We consider the maximum variation in e, $\pm|\Delta\bar{e}|$:

$$|\Delta e|^2 \lesssim \left(\frac{5}{2}S^2 + S + 1\right)\frac{R_p^2}{a^2} + \frac{5}{2}\frac{u_{eject}^2}{v_{orb}^2} + \left\{\left[\left(\frac{3S^2}{2} + 3S\right)\frac{R_p^2}{a^2} - \frac{3}{2}\frac{u_{eject}^2}{v_{orb}^2}\right]^2 + \left[(3S+3)\frac{R_p}{a}\frac{u_{eject}}{v_{orb}}\right]^2\right\}^{\frac{1}{2}}. \tag{H2}$$

Taking WD 1145+017 as an example, and for a planetesimal with $R_p = 100\,\mathrm{km}$, $u_{eject} \lesssim 1000\,\mathrm{m/s}$, we find out that $|\Delta e| \lesssim 0.0064$, such that the ejecta remains on near circular orbit, as is verified in the lower panel of Fig.H1.

More importantly, as is shown in Fig.H1, although Δe is sensitive to the true anomaly f (vector addition), $\Delta\tau$ and i' almost remain constant, nearly equal to their circular-orbit counterparts. Hence, when considering $\Delta\tau$ and i' on a near circular orbit, one can effectively simplify the geometry to a circular orbit.

We generalize the approximations for near circular orbits to moderately eccentric orbits, where the local keplerian speed and semi-major axis, is of the same order of magnitude as the orbital speed and distance, respectively, throughout the orbit, such that we may assume:

- $\frac{v_{spin}}{v_k} \ll 1$,
- $\frac{u_{eject}}{v_k} \ll 1$
- $\frac{v_{orb}}{v_k} \sim 1$
- $\frac{R_p}{r} \ll 1$,
- $\frac{a}{r} \sim 1$,
- $\frac{2M_p a}{M_* R_p} = \frac{v_{esc}^2}{v_k^2} < \frac{u_{eject}^2}{v_k^2}$,

where $v_k = \sqrt{\frac{GM_*}{a}}$ is the keplerian speed.

The first-order approximation for semi-major axis of the ejecta is:

$$\frac{1}{a'} \approx \frac{1}{a} - \frac{1}{a}\frac{2R_p}{r}\frac{a}{r}\sin\theta\cos\phi - \frac{1}{a}\left[2\frac{\omega_p R_p}{v_k}\frac{v_{orb}}{v_k}(-\cos\gamma\sin\theta\sin\phi + \sin\gamma\sin\theta\cos\phi) + 2\frac{u_{eject}}{v_k}\frac{v_{orb}}{v_k}(\cos\gamma\sin\theta\cos\phi + \sin\gamma\sin\theta\sin\phi)\right], \tag{H3}$$

from which we can deduce that:

$$\frac{\Delta\tau}{\tau} \approx 3\sin\theta\left[\frac{R_p}{r}\frac{a}{r}\cos\phi + \frac{\omega_p R_p}{v_k}\frac{v_{orb}}{v_k}(-\cos\gamma\sin\phi + \sin\gamma\cos\phi) + \frac{u_{eject}}{v_k}\frac{v_{orb}}{v_k}(\cos\gamma\cos\phi + \sin\gamma\sin\phi)\right], \tag{H4}$$

which increases with v_{orb} and decreases with r, while further correlated with γ. Since the term $\frac{u_{eject}}{v_k}$ usually dominates for the parameters we consider, $\Delta\tau$ is maximized near the pericentre.

The first-order approximation for the orbital angular momentum is:

$$\begin{aligned}\bar{J}' &= -R_p v_{orb} \sin\gamma \cos\theta \hat{i} \\ &+ (R_p v_{orb} \cos\gamma \cos\theta - u_{eject} r \cos\theta)\hat{j} \\ &+ (r v_{orb} \sin\gamma + \omega_p R_p r \sin\theta \cos\phi + r u_{eject} \sin\theta \sin\phi \\ &+ R_p v_{orb} \sin\gamma \sin\theta \cos\phi - R_p v_{orb} \cos\gamma \sin\theta \sin\phi)\hat{k},\end{aligned} \tag{H5}$$

which gives the inclination:

$$i' \approx \frac{\cos\theta}{\sin\gamma}\sqrt{\frac{R_p^2}{r^2} - 2\frac{R_p}{r}\frac{u_{eject}}{v_{orb}}\cos\gamma + \frac{u_{eject}^2}{v_{orb}^2}}, \tag{H6}$$

whose maximum (although unclear analytically, but can be deduced based on the order of magnitude of the terms) is usually reached when v_{orb} is minimized, i.e., the apocentre.

I Back reaction of volcanic ejecta on the planetesimal

In this section we investigate the effect of non-isotropic volcanism ejection on the orbit of the planetesimal. The induced impulse velocity of the planetesimal $\delta\bar{v}$ due to ejecta mass δm with ejection velocity $\bar{u}_{eject}$ satisfies:

$$\delta\bar{v}(M_p - \sum \delta m) + \sum \left(\bar{u}_{eject}\delta m\right) = 0, \tag{I1}$$

and hence:

$$\delta\bar{v} = -\frac{1}{M_p - \sum \delta m}\sum\left(\delta m u_{eject}\begin{bmatrix}\sin\theta\cos\phi \\ \sin\theta\sin\phi \\ \cos\theta\end{bmatrix}\right). \tag{I2}$$

For simplicity, we consider single ejection case (alternatively, a weighted average), such that the summation can be omitted. The speed of the planetesimal after volcanism ejection is:

$$v_{tot} = \left|\left|\begin{bmatrix}v_{orb}\cos\gamma - \Delta u_{eject}\sin\theta\cos\phi \\ v_{orb}\sin\gamma - \Delta u_{eject}\sin\theta\sin\phi \\ -\Delta u_{eject}\cos\theta\end{bmatrix}\right|\right|, \tag{I3}$$

where $\Delta = \frac{\delta m}{M_p - \delta m}$.

We then solve the equation:

$$\frac{1}{2}v_{tot}^2 - \frac{GM_*}{r} = -\frac{GM_*}{2a'}, \tag{I4}$$

with $\frac{1}{2}v_{orb}^2 - \frac{GM_*}{r} = -\frac{GM_*}{2a}$, and get (to the leading order):

$$\frac{1}{a'} \approx \frac{1}{a} + \frac{2\Delta v_{orb} u_{eject}(\cos\gamma \sin\theta \cos\phi + \sin\gamma \sin\theta \sin\phi)}{GM_*}. \tag{I5}$$

Assuming that $\Delta v_{orb} u_{eject} \ll v_k^2$, Eq.I5 can be approximated as:

$$\frac{\delta a}{a} \approx -2\Delta \frac{v_{orb}}{v_k}\frac{u_{eject}}{v_k}(\cos\gamma \sin\theta \cos\phi + \sin\gamma \sin\theta \sin\phi). \tag{I6}$$

For a near circular orbit Eq.I5 becomes:

$$\frac{\delta a}{a} \approx -2\Delta \frac{u_{eject}}{v_{orb}} \sin\theta \sin\phi, \tag{I7}$$

which, since $\Delta \ll 1$, is much smaller compared to the orbit dispersion of the ejecta and is usually negligible.

The differential form of Eq.I7 can be obtained by substituting $\Delta = -\frac{dM_p}{M_p}$:

$$\frac{\dot{a}}{a} \approx \frac{2\dot{M}_p}{M_p}\frac{u_{eject}}{v_{orb}} \sin\theta \sin\phi, \tag{I8}$$

whose magnitude is negligible over an observational timescale of years ($\frac{\delta a}{a} \lesssim 10^{-8}\,\mathrm{yr}^{-1}$ for a planetesimal with a radius of 100 km, density $6000\,\mathrm{kg/m^3}$ around WD 1145+017 with a mass loss rate of 8×10^9 g/s Vanderburg et al., 2015 and ejection speed of 500 m/s). On the other hand, the maximum orbital perturbations due to the back reactions of non-spherically symmetric volcanism may outweighs the orbital evolution under tide on a near circular orbit. Therefore, there may exist a scenario where volcanism raises orbital eccentricity of the planetesimal and help sustain volcanism.

Similarly, mass loss may exert torque on the planetesimal, altering its spin. The torque $\bar{\tau}$ is given by:

$$\bar{\tau} = \frac{d(I_p \bar{\omega}_p)}{dt} = \sum \dot{M}_p \bar{r} \times \bar{u}_{eject}, \tag{I9}$$

where $\bar{r}$ is the position vector of the ejection relative to the planetesimal's centre of mass. Meanwhile, the spin of the planetesimal is also altered by tidal evolution (Hut, 1981; Levrard et al., 2007; Leconte et al., 2010; Matsumura et al., 2010; Bolmont et al., 2011; Heller et al.,

2011; Beaugé & Nesvorný, 2012; Hansen, 2012; Glanz et al., 2022; Rozner et al., 2022; Lu et al., 2023):

$$\begin{aligned}\frac{d\omega_p}{dt}|_{tide} &= K_p n^2 \frac{M_*^2}{(M_p+M_*)M_p}\frac{R_p^3}{a^3}\frac{1}{C_p}(1-e^2)^{-6} \\ &\times\left[f_2(e)n\cos\epsilon_p - \frac{1}{2}(1+\cos^2\epsilon_p)(1-e^2)^{\frac{3}{2}}f_5(e)\omega_p\right],\end{aligned} \tag{I10}$$

where ϵ_p is obliquity, which evolves towards 0 over a timescale similar to the pseudo-synchronization timescale. f_2 and f_5 are given by:

$$\begin{aligned}f_2(e) &= 1+\frac{15}{2}e^2+\frac{45}{8}e^4+\frac{5}{16}e^6, \\ f_5(e) &= 1+3e^2+\frac{3}{8}e^4.\end{aligned} \tag{I11}$$

Assuming that the surface of the planetesimal is strength-less, the breakup limit is:

$$\omega_{break} = \sqrt{\frac{GM_p}{R_p^3} - \frac{2GM_*}{q_0^3}}, \tag{I12}$$

The maximum spin-up rate due to volcanism can be approximated as:

$$\frac{d\omega_p}{dt}|_{volc} = -\frac{\dot{M}_p u_{eject}}{M_p R_p C_p}, \tag{I13}$$

And the equilibrium spin rate (volcanism-induced spin-up rate matches the tidally induced spin-down rate) is determined by setting $\frac{d\omega_p}{dt}|_{volc} + \frac{d\omega_p}{dt}|_{tide} = 0$:

$$\omega_{eq} = \frac{2f_2(e)n\cos\epsilon_p - 2\frac{\dot{M}_p u_{eject}}{GK_p M_*^2 R_p^4}\left(\frac{2q_0 Q_0}{q_0+Q_0}\right)^6}{(1+\cos^2\epsilon_p)(1-e^2)^{\frac{3}{2}}f_5(e)}, \tag{I14}$$

which for circular orbit and spin-orbit alignment is:

$$\omega_{eq} = n - \frac{\dot{M}_p u_{eject} a^3 (M_p+M_*)}{K_p n^2 M_*^2 R_p^4}, \tag{I15}$$

and is effectively identical to the synchronous rotation rate (n) for a planetesimal around WD 1145+017 assuming a mass loss rate of 8×10^9 g/s (Vanderburg et al., 2015) (volcanism-induced break-up timescale $\gtrsim$ 3000 yr). One can show that this is also true for eccentric orbits. Therefore, under the CTL model, volcanism-induced break-up is rare.

J Energy for fracture

To cause fracture in the solid mantle for volcanic eruption, tidal energy needs to support the strain energy corresponding to the strength of the planetesimal, leading to an additional energy loss Q_s:

$$Q_s = \frac{1}{2}\frac{V\sigma_-^2}{E}, \tag{J1}$$

where V is the conduit volume, E is the Young's modulus of the solid layer and we consider the compressive strength σ_-. We estimate Q_s assuming $V = \frac{4}{3}\pi R_p^3(1-f_m^3)$, $\sigma_- \sim -100\,\mathrm{MPa}$, $E \sim 100\,\mathrm{GPa}$ (Slyuta, 2017; Gouriet et al., 2019; Tanbakouei et al., 2019; Pohl & Britt, 2020; Tang et al., 2023). We find out that $\frac{Q_s}{c_p M_p} \sim 0.005\,\mathrm{K} \ll \Delta T_c$ and can hence be neglected.

Furthermore, the conduit is not necessarily in the radial direction, hence inducing additional compressive stress due to gravity (hydrostatic stress) and friction (deviatoric stress) (Turcotte & Schubert, 2014):

$$\begin{aligned} \sigma_x &= -\rho_p g h \left[1 \pm \frac{2f_s}{(1+f_s^2)^{\frac{1}{2}} \mp f_s}\right], \\ \sigma_y &= -\rho_p g h, \end{aligned} \tag{J2}$$

where we assume $g = \frac{GM_p}{R_p^2}$, $h = (1-f_m)R_p$, $f_s \sim 0.85$ (coefficient of friction Byerlee, 1978; Turcotte & Schubert, 2014). We find out that $\sigma = \sqrt{\sigma_x^2 + \sigma_y^2} \sim \rho_p g h \lesssim 10\,\mathrm{MPa} \ll \sigma_-$. The corresponding strain energy is negligible compared to that corresponds to the compressive strength and can hence be neglected.

Finally, additional thermal energy is lost to the planetesimal's interior cooler than the magma before eruption (Abrahams & Nimmo, 2019). For a magma refilling timescale of t_{refill} and assuming that the magma chamber diffuses heat to its ambient from a semi-sphere with radius $\frac{1}{2}(1-f_m)R_p$, the ratio of heat lost to the ambient to the thermal energy of the magma can be estimated as:

$$\frac{Q_{diff}}{E_{magma}} \sim \frac{6\pi\sqrt{t_{refill}\alpha_t}}{(1-f_m)R_p}. \tag{J3}$$

Assuming $t_{refill} \sim 1$ yr (constrained by WD 1145+017 observational time span), we have $\frac{Q_{diff}}{E_{magma}} \sim 0.06$. Hence, the majority of the thermal energy is retained in the magma.

K Thermal properties of planetesimal

In this section, we examine the variations in the conditions for melting and volcanism using the temperature dependent thermal properties for different types of rocks.

Type	T_c (K)	T_0 (K)	$\left(\Delta T_c - \frac{\Delta h_f}{c_p}\right)$ (K)	f_Q
Forsterite	2000	50	2296	0.73
	2000	500	1921	0.62
	1500	50	1607	0.81
	1500	500	1231	0.69
	1000	50	961	0.92
	1000	500	586	0.78
Granite	2000	50	2009	0.55
	2000	500	1784	0.44
	1500	50	1406	0.63
	1500	500	1180	0.49
	1000	50	802	0.74
	1000	500	577	0.58
Granodiorite	2000	50	2165	0.46
	2000	500	1791	0.40
	1500	50	1559	0.51
	1500	500	1185	0.44
	1000	50	953	0.57
	1000	500	580	0.49
Gabbro	2000	50	2046	0.57
	2000	500	1696	0.50
	1500	50	1417	0.63
	1500	500	1067	0.55
	1000	50	856	0.70
	1000	500	507	0.61
Garnet amphibolite	2000	100	2388	0.56
	2000	500	2011	0.50
	1500	50	1631	0.61
	1500	500	1255	0.55
	1000	50	943	0.67
	1000	500	567	0.60

Table 1: The temperature representation of critical energy of melting excluding the contributions from the enthalpy of fusion, $\Delta T_c - \frac{\Delta h_f}{c_p}$, as well as the ratio of steady state heat loss rate under time dependent $\kappa(T)$ to its counterpart of fixed κ, f_Q, for different types of rocks, different critical temperature of melting T_c and different initial temperature T_0. The data for forsterite is from Gillet et al., 1991; Lesher & Spera, 2015, with the remaining from Miao et al., 2014.

We investigate the empirical relations of $c_p(T)$ for different types of rocks (Miao et al., 2014), assuming that below/above the numerical minimum/maximum of the empirical relations, c_p stays constant, equal to the minimum/maximum. The empirical relations are of the form of:

$$c_p = a + \frac{b}{T^{\frac{1}{2}}} + \frac{c}{T} + \frac{d}{T^2} + \frac{e}{T^3}, \tag{K1}$$

with the constants a–e dependent on the types of rocks. We consider three critical temperature of melting $T_c \sim 1000\,\mathrm{K}$, $1500\,\mathrm{K}$ and $2000\,\mathrm{K}$, accounting for the values of different substances (Lesher & Spera, 2015; Scheinberg et al., 2015; Johansen et al., 2023) together with two initial temperatures, $T_0 \sim 50\,\mathrm{K}$ and $500\,\mathrm{K}$, corresponding to the equilibrium temperature of a planetesimal on a highly eccentric orbit when the host star enters its white dwarf phase, and with a cooling age of $\sim 100\,\mathrm{Myr}$, respectively. The corresponding ΔT_c excluding the contributions of the heat of fusion is shown in Table 1. The range of the enthalpy of fusion, is $\sim 300\,\mathrm{kJ/kg}$–$1000\,\mathrm{kJ/kg}$ (Fukuyama, 1985; Lesher & Spera, 2015). In this case, ΔT_c ranges from $\sim 800\,\mathrm{K}$ to $\sim 3000\,\mathrm{K}$. Compared to the results obtained using the fiducial values, melting is possible with a lower tidal evolution rate. For instance, $q_{0,crit}$ (Eq.11 in the main text) may maximally increase by $\sim 20\%$.

We consider the empirical relation in Miao et al., 2014 for $\kappa(T)$:

$$\kappa = \frac{1}{a + bT}, \tag{K2}$$

with a and b compositional dependent constants. The corresponding heat loss rate is given by Eq.E8.

With other parameters remain identical, the ratio of heat loss rate under time dependent $\kappa(T)$ to its counterpart of fixed κ, f_Q (the ratio of Eq.E8 to Eq.E3) is:

$$f_Q = \frac{\ln \frac{\kappa(T_s)}{\kappa(T_c)}}{b\kappa(T_c - T_s)}, \tag{K3}$$

As is shown in Table 1, we find out that $f_Q \lesssim 1$. Melt can hence be maintained at a smaller tidal power than the case of constant κ. For instance, $q'_{0,crit}$ (Eq.15 in the main text) may maximally increase by $\sim 10\%$.

L Surface heating of the planetesimal

We investigate the case where the sum of tidal power and stellar irradiation balances the radiative cooling:

$$4\pi R_p^2 \sigma < T_s^4 >= \dot{E}_t + \frac{R_p^2 L_*}{4a^2 \beta_r \sqrt{1 - e^2}} \tag{L1}$$

where the factor $\frac{1}{\sqrt{1-e^2}}$ originates from temporal average of stellar irradiation and $< T_s^4 >^{\frac{1}{4}} \neq < T_s >$ (Eq.13 in the main text) is an radiative power related time-averaged equilibrium temperature and β_r accounts for the fraction of re-radiation (1 for a fast rotator and 0.5 for a tidally-locked body).

Numerical simulations show that the maximum T_s is usually dominated by either tidal power or stellar flux, with cases with comparable contributions from both simultaneously being rare (because of their distinct dependence on orbital eccentricity). Hence, we may consider tidal heating and stellar irradiation dominated cases separately. In the cases where tidal power dominates, the maximum surface temperature of the planetesimal is reached at the maximum of tidal power, $e \approx 0.735$:

$$(< T_s^4 >)^{\frac{1}{4}}_{max,tide} \sim 800\,\mathrm{K} \left(\frac{R_p}{100\,\mathrm{km}}\right)^{\frac{3}{4}} \left(\frac{M_*}{0.6\,M_\odot}\right)^{\frac{3}{4}} \left(\frac{0.005\,\mathrm{AU}}{q_0}\right)^{\frac{9}{4}}, \tag{L2}$$

which, assuming a planetesimal with a radius of 100 km, density and tensile strength being the average of the measured Solar System ordinary chondrites, $\rho_p = 3500\,\mathrm{kg/m^3}$, $\sigma_+ = 25\,\mathrm{MPa}$ (Pohl & Britt, 2020), can only exceed 1400 K (solidus temperature of silicates Scheinberg et al., 2015; Johansen et al., 2023) if the planetesimal is perturbed near/within its Roche limit ($q_0 \lesssim 0.004\,\mathrm{AU} \approx \mathrm{r}_{Roche}$).

Meanwhile, the irradiation dominated surface temperature given by:

$$(< T_s^4 >)^{\frac{1}{4}}_{irr} \sim 900\,\mathrm{K} \left(\frac{L_*}{0.01\,L_\odot}\right)^{\frac{1}{4}} \left(\frac{0.005\,\mathrm{AU}}{q_0}\right)^{\frac{1}{2}} \frac{(1-e^2)^{\frac{3}{8}}}{\beta_r^{\frac{1}{4}}}, \tag{L3}$$

where we assume that $q_0 \ll Q_0$. Surface melting/sublimation usually occurs in the rapid circularization case where the planetesimal is tidally locked on a close-in near circular orbit with the white dwarf remaining hot. In this case, for T_s to exceed 1400 K, we require (using Eq.14 in the main text):

$$\left(\frac{M_*}{0.6\,M_\odot}\right)^{\frac{1}{4}} \left(\frac{0.005\,\mathrm{AU}}{q_0}\right)^{\frac{1}{2}} \left(0.1 + \frac{t_{cooling-age}}{\mathrm{Myr}}\right)^{-0.295} \gtrsim 0.3. \tag{L4}$$

Taking $M_* = 0.6\,\mathrm{M}_\odot$ and using the fact that white dwarf with observed transits all have cooling ages above 100 Myr, we obtain $q_0 \lesssim 0.004$ AU.

M Orbit dispersion under additional perturbations

We investigate the effects of the planetesimal on the ejecta using Rebound (Rein & Liu, 2012). For identical parameters as Fig.4 in the main text, we plot the predicted orbital period dispersion and inclination accounting for the planetesimal after 1 orbital period in Fig.M1. The black pixels indicate the collisions of the ejecta with the planetesimal. In general, the

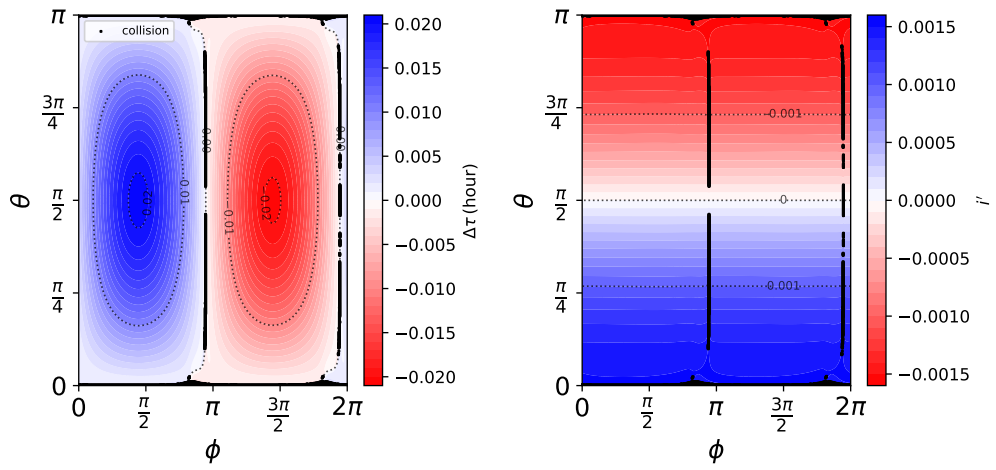

Figure M1: Same plot as Fig.4 in the main text, but simulated using Rebound (Rein & Liu, 2012) for an integration time of one orbital period, including the gravitational force from the planetesimal and general relativistic effect. The black pixels represent where collisions between the ejecta and the planetesimal occur.

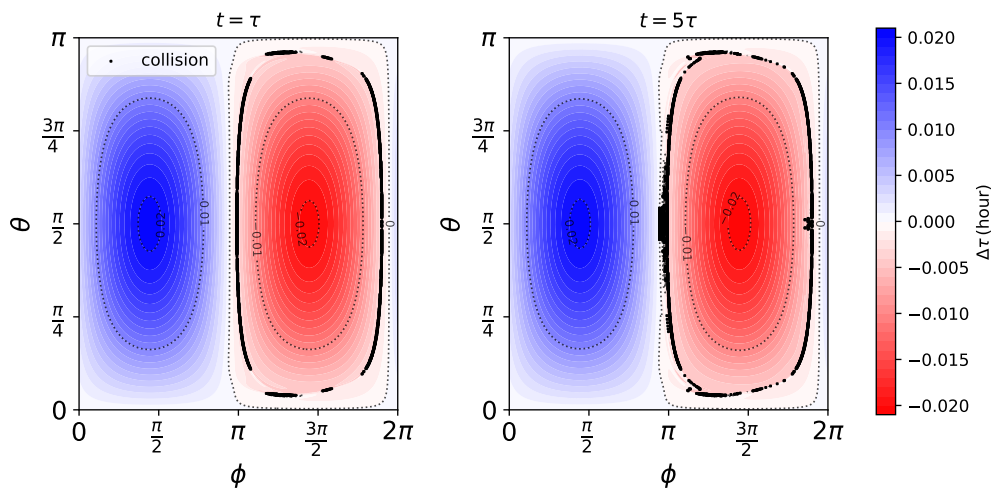

Figure M2: Same plot as the left panel of Fig.4 in the main text (period dispersion), but simulated using Rebound (Rein & Liu, 2012) for an integration time of 1 (left panel) and 5 (right panel) orbital periods, including the gravitational force from the planetesimal, general relativistic effect and radiation perturbations. The ejected dust is assumed to have a radius of 10^{-5} m and a density of $3000\,\mathrm{kg/m^3}$. The black pixels represent where collisions between the ejecta and the planetesimal occur.

simulations show consistency with the analytical results, both qualitatively (the dependence on θ and ϕ) and qualitatively (fractional error $\lesssim 5\%$ for $u_{eject} = 500\,\mathrm{m/s}$, which decreases with the increase in u_{eject}). The exceptions occur around the regions where $\Delta\tau \to 0$ under the analytical model, where the ejecta remains close to the planetesimal, with their orbits strongly torqued by the planetesimal and a higher risk of collision with the planetesimal. The analytical model remains a reasonable approximation in the majority of the parameter space, for instance, when considering the maximum orbital period dispersion.

We further include the radiation force. Analytically, the inclusion of radiation pressure is equivalent to a reduced mass of the host star ($(1-\beta)M_*$ with β the ratio of radiation to gravitational force), with the semi-major axis perturbation for a near circular orbit given by:

$$\begin{aligned}\frac{\Delta a}{a} \approx\, & 2\frac{R_p}{a}\sin\theta\cos\phi + \frac{\beta}{1-\beta} + 2\frac{\omega_p R_p}{v_{orb}(1-\beta)}\sin\theta\cos\phi \\ & + 2\frac{u_{eject}}{v_{orb}(1-\beta)}\sin\theta\sin\phi,\end{aligned} \tag{M1}$$

where the term $\frac{\beta}{1-\beta}$ corresponds to the expanding semi-major axis under radiation pressure, and the contributions of spin and ejection velocities to $\frac{\Delta a}{a}$ are enlarged by a factor of $\frac{1}{1-\beta}$.

We simulate the orbital period dispersion ($\Delta\tau$) including both PR drag and radiation pressure, as is shown in Fig.M2, where we plot the resultant period dispersion after 1 (left panel) and 5 (right panel) orbital periods together with the parameter space where collisions occur (black pixels). In general, by comparing Fig.M2 to Fig.M1/Fig.4 in the main text the inclusion of radiation perturbations does not alter the orbit dispersion qualitatively shortly after ejection. Two major effects of radiation force are: 1. the parameter space of collisions and the behaviours of the ejecta with small $\Delta\tau$ are altered and 2. the ejecta is drifted towards shorter periods with time.

N Maximum dust production rate on a near circular orbit

We compute the mass loss rate for a sample planetesimal under our fiducial parameters in Table 1 in the main text at $e = 0.01$ in Fig.N1, assuming a fixed volcanic ejection speed of 500 m/s (excluding the planetesimal with a radius larger than $\sim$ 400 km where the escape speed exceeds 500 m/s). To reach the mass loss rate of 8×10^9 g/s (4.3×10^{10} g/s), the sample planetesimal should be larger than $\sim$ 170 km (260 km) and starts at a pericentre distance below 0.007 AU/orbital period after circularization $\tau_{cir} \lesssim 20$ hr ($q_0 \lesssim 0.006$ AU, $\tau_{cir} \lesssim 17$ hr). Hence, rocky planetesimals on short-period near circular orbits are able to produce the mass loss rate at the same level as that required to explain the transits around WD 1145+017 provided that they are large and perturbed close enough to the white dwarf. These rocky planetesimal, potentially associated with large mass loss rate and deep transit depth, should circularize to an orbital period $\lesssim 20$ hr.

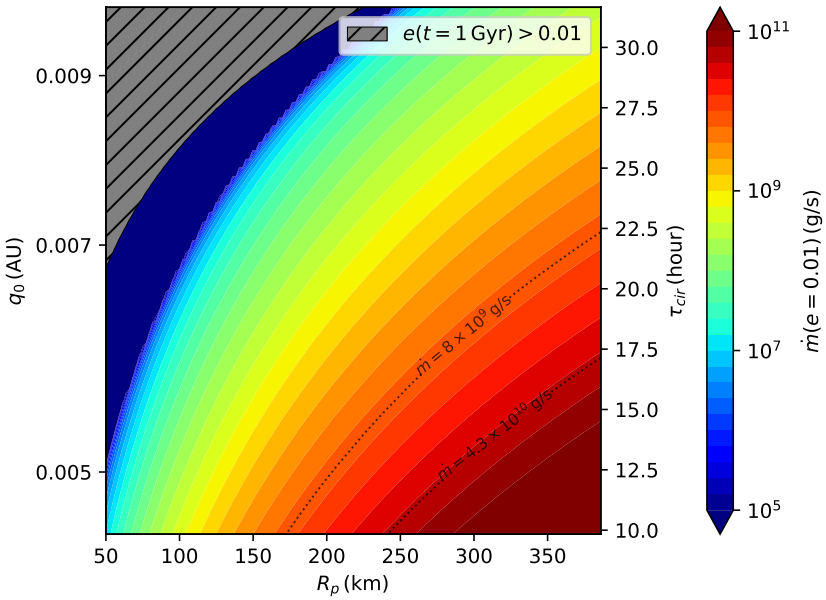

Figure N1: The numerically computed maximum mass loss rate allowed by tidal heating for different-sized planetesimals starting at different pericentre distances when the planetesimal reaches $e = 0.01$ (other free parameters identical to those in Table 1 in the main text, Roche limit 0.00456 AU) for a volcanism ejection speed of 500 m/s. The contour lines are the predicted mass loss rate to explain the transit around WD 1145+017 (Vanderburg et al., 2015) and the accretion rate (Xu et al., 2016).

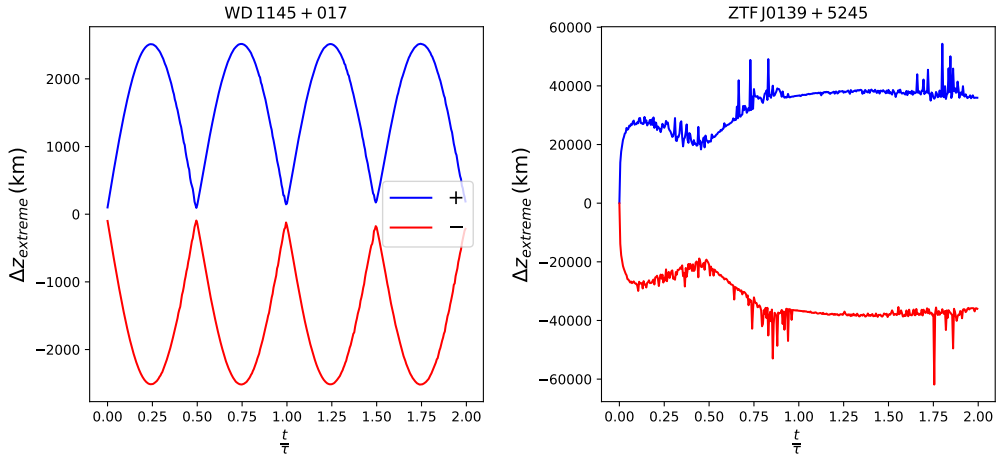

Figure O1: The maximum z-span of volcanism ejecta for two systems, WD 1145+017 ($0.6\,M_\odot$, $\rho_p = 6000\,\mathrm{kg/m^3}$, $\tau = 4.5\,\mathrm{hr}$, $e = 0.01$) and ZTF J0139+5245 ($0.52\,M_\odot$, $\rho_p = 3000\,\mathrm{kg/m^3}$, $\tau = 107.2\,\mathrm{day}$, $e = 0.98$) at two different true anomalies ($f = \frac{\pi}{2}$ and $f = \pi$). Other free parameters are identical to those in Table 1 in the main text.

O Orbital evolution of the ejecta

We simulate the position of volcanic ejecta for 10000 particles erupted at the same time that avoid collision with the planetesimal. We focus on the span of the ejecta. The direction of the ejection velocity is assumed to follow a normal distribution with the mean at θ and ϕ and a standard deviation of $\frac{\pi}{10}$.

The maximum z span ($\Delta z_{extreme}$) of the volcanism ejecta which corresponds to the maximum transit depth is shown in Fig.O1 for two systems, planetesimal on a near circular orbit around WD 1145+017 and planetesimal on a highly eccentric orbit around ZTF J0139+5245. $\Delta z_{extreme}$ for WD 1145+017 is almost periodic for single ejection, with $\Delta z_{extreme}$ maximized at $\frac{(2n+1)}{4}\tau$. For a highly eccentric orbit, $\Delta z_{extreme}$ is dependent on the true anomaly and can be orders of magnitude larger than its counterpart for a near circular orbit, corresponding to the possibility of a much larger transit depth (but note a higher probability of optically thin ejecta).

In Fig.O2, we plot the orbital evolution of the ejecta's span for the planetesimal around WD 1145+017. We assume that the volcanism ejection occurs at $x = 0$ (cyan plus) while we always observe the ejecta at $y = 0$ (to illustrate the maximum span along the z axis). Due to the orbital period dispersion, the leading (ejecta with shorter orbital period) and trailing tails (ejecta with longer orbital period) diffuse away from the planetesimal with time. The leading tail will catch up the trailing tail at $\sim 50\tau$.

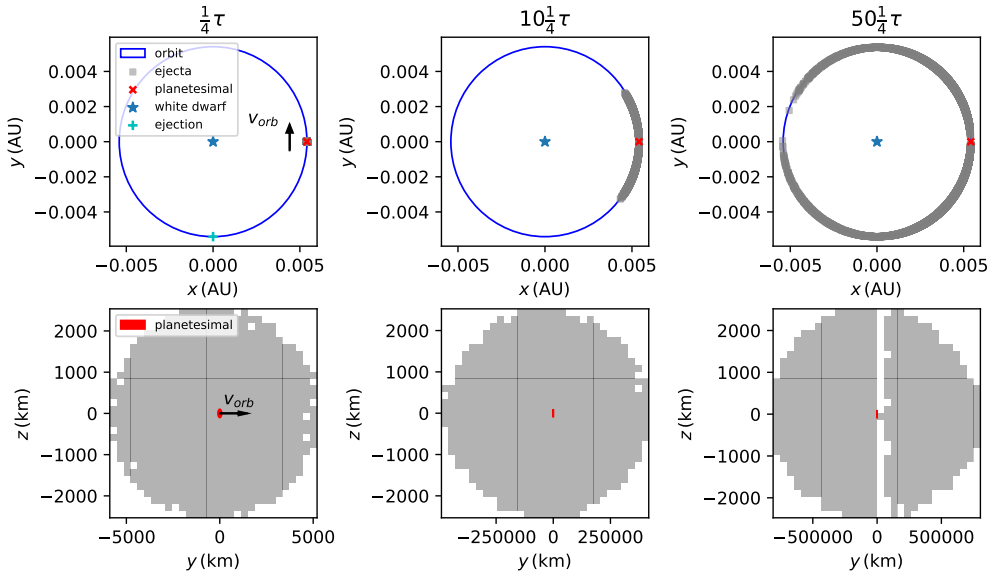

Figure O2: Rebound simulation of the positions of 10000 ejected particles (not colliding with the planetesimal) with size 10^{-5} m and density of $3000\,\mathrm{kg/m^3}$ in the orbital plane (upper panels) and along the x-axis (lower panels) when the planetesimal is at $y = 0$. See the text for other settings.

P Tidal and PR escape timescale

One can show that for a planetesimal/disk starting on an extremely eccentric orbit, when the apocentre decays by one Hill radius (r_H) of the planet (defined as the condition for escape), the planetesimal/disk remains on a highly eccentric orbit with little circularization. Hence, the tidal escaping timescale is:

$$\tau_{e,tide} \approx 5\frac{r_H M_p q_0^{7.5}}{G K_p M_*^2 R_p^5 Q_0^{0.5}}, \tag{P1}$$

The PR escaping timescale is:

$$\tau_{e,PR} \approx 7\frac{r_H c^2 D \rho q_0^{1.5}}{L_* Q_0^{0.5}}. \tag{P2}$$

Q General relativistic precession

The GR precession of a disk may mimic periodic signals. The period of this signal is given by the precession period (Pál & Kocsis, 2008; Yahalom, 2022; Childs et al., 2024):

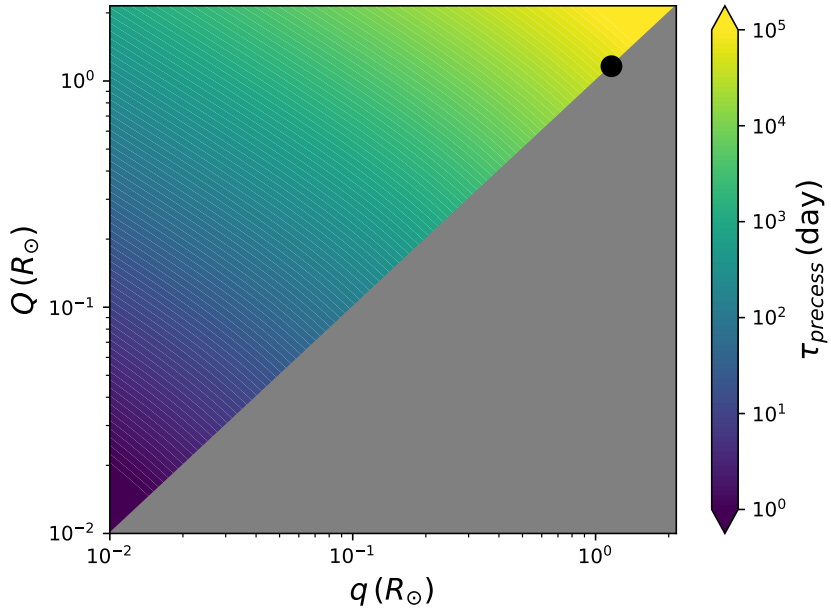

Figure Q1: The precession period as a function of pericentre distance and apocentre distance. The black dot is the position of the transiting body on a 4.5 hr near circular orbit around WD 1145+017.

$$\tau_{precess} = \frac{2^{\frac{1}{2}}\pi c^2 qQ(q+Q)^{\frac{1}{2}}}{3(1-\beta)(GM_*)^{\frac{3}{2}}}, \tag{Q1}$$

where the factor $1-\beta$ accounts for radiation pressure (Wyatt & Whipple, 1950). We estimate $\tau_{precess}$ (with $\beta \sim 0$) in q–Q space, which is shown in Fig.Q1. The precession period of the transiting body on a 4.5 hr near circular orbit around WD 1145+017, $\sim$ 150 yr is represented by the black dot.

R Collisions among tidally evolved planetesimals

For a spherical shell of tidally circularized planetesimals, the collision rate between the circularized planetesimals (which are assumed to not collide with each other) and partially circularized planetesimals $r_{collision}$ can be estimated as:

$$r_{collision} \sim n_{cir} \sum_i w_i P_i \sigma_i v_i, \tag{R1}$$

where n_{cir} is the number density of (nearly) circularized planetesimals (with $e \leq 0.01$), σ_i is the collisional cross-section of partially circularized planetesimal i with the circularized planetesimals:

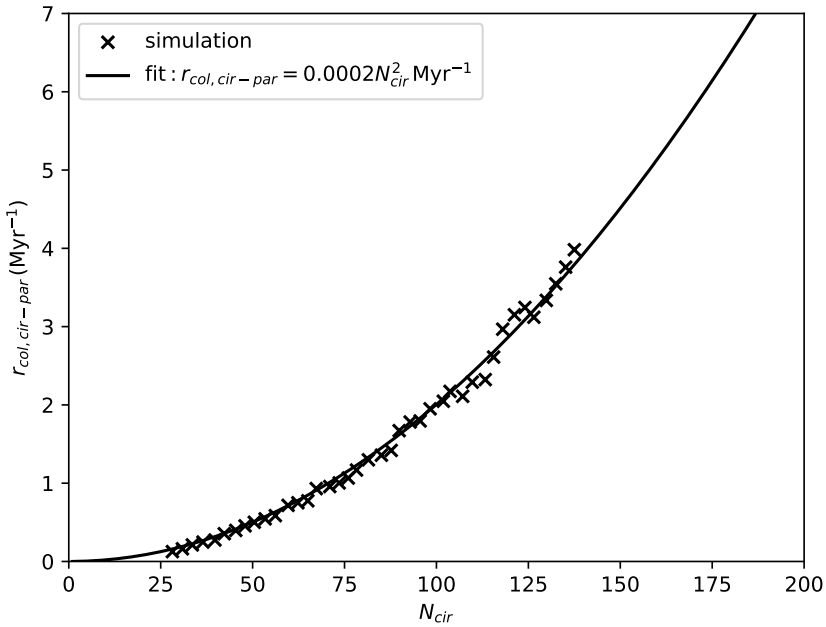

Figure R1: The predicted collision rate between nearly circularized planetesimals $e \leq 0.01$ with their partially circularized counterpart as a function of the number of circularized planetesimals based on the same orbit distribution used for Fig.11 of Li et al., 2025. We assume a truncated planetesimal size distribution of $P(R_p) \propto R_p^{-4}$ from 50 km to 1000 km, together with a uniform size distribution between $3000\,\mathrm{kg/m^3}$ to $6000\,\mathrm{kg/m^3}$.

$$\sigma_i = \pi(R_i + R_{cir})^2 \left(1 + \frac{v_\infty^2}{v_i^2}\right), \tag{R2}$$

with the term $\frac{v_\infty^2}{v_i^2}$ accounting for the gravitational focusing effect. v_∞ is given by:

$$v_\infty = \sqrt{\frac{2G(M_i + M_{cir})}{R_i + R_{cir}}}. \tag{R3}$$

v_i is the encounter speed of the partially circularized planetesimal i with the circularized planetesimal:

$$v_i = \left| v_{orb}(r) \begin{bmatrix} \cos\gamma \\ \sin\gamma \\ 0 \end{bmatrix} - v_k(r) \begin{bmatrix} 0 \\ \cos\theta' \\ \sin\theta' \end{bmatrix} \right|, \tag{R4}$$

where $v_{orb}(r) = \sqrt{G(M_* + M_i)(\frac{2}{r} - \frac{1}{a_i})}$ is the speed of the partially circularized planetesimal i during orbital crossing with a circularized planetesimal with keplerian speed $v_k = \sqrt{\frac{G(M_* + M_p)}{r}}$. θ' ($0 \leq \theta' \leq \pi$) is the angle between the two orbital planes (the angle between the orbital angular momentum of the partially circularized planetesimal i and the circularized planetesimal it collides with). γ is the angle between the radial vector and velocity vector of the partially circularized planetesimal. P_i accounts for the fact that not all circular orbits within the spherical shell will intersect the orbit of the partially circularized planetesimal, leading to a reduced n_{cir}. Consider a random point on a circle with radius r' and a random point on a sphere with radius r. We define the coordinate system such that they are described by $(r'\cos\phi, r'\sin\phi, 0)$ and $(r\sin\theta, 0, r\cos\theta)$, respectively. The distance squared between these two points is given by:

$$d^2 = r^2 + r'^2 - 2rr'\sin\theta\cos\phi. \tag{R5}$$

And hence:

$$\theta = \sin^{-1}\left(\frac{r^2 + r'^2 - d^2}{2rr'\cos\phi}\right), \tag{R6}$$

where θ only has solution if $\frac{r^2 + r'^2 - d^2}{2r'r} \leq 1$. As $d \ll r'$ and $d \ll r$, this condition is only fulfilled as $r' \to r$, where $\theta \to \frac{\pi}{2}$. Then, we aim to minimize θ for $0 < \theta < \frac{\pi}{2}$, which is reached at the maximum of d, $d = R_i + R_{cir}$ (the gravitational focusing term is negligible due to the high encounter speed), the maximum of $\cos\phi$ ($\cos\phi = 1$, $\phi = 0$), and $r' = \sqrt{r^2 - d^2}$. And hence:

$$\theta \approx \sin^{-1}\left(1 - \frac{d^2}{2r^2}\right) \approx \frac{\pi}{2} - \frac{d}{r} \tag{R7}$$

For a random θ between 0 and $\frac{\pi}{2}$, the probability of lying in an interval between $\frac{\pi}{2} - \frac{d}{r}$ and $\frac{\pi}{2}$ is:

$$P_i \sim \frac{2\,(R_i + R_{cir})}{\pi r}, \tag{R8}$$

which leads to a significant reduction in the effective number density of circularized planetesimals. w_i is the effective number of the partially circularized planetesimal i, describing the fraction of time that the partially circularized planetesimal spends in the spherical shell containing the circularized planetesimals. w is given by:

$$w = \frac{2}{\tau}\int_{\max(r_{min},q)}^{\min(r_{max},Q)} \frac{dt}{dr}dr = \frac{(1-e^2)^{\frac{1}{2}}}{\pi a e}\int_{\max(r_{min},q)}^{\min(r_{max},Q)} \frac{dr}{\sin f}, \tag{R9}$$

with $\sin f$ being $\sqrt{1 - \left[\frac{a(1-e^2)}{re} - \frac{1}{e}\right]^2}$, the factor of 2 representing entering and exiting the shell. For a narrow shell, Eq.R9 reduces to:

$$w(r|q < r < Q) = \frac{2}{\tau}\frac{\delta r}{v_r} = \frac{(1-e^2)^{\frac{1}{2}}\delta r}{\pi a e \sin f} = \frac{\delta r r}{\pi a\sqrt{(r-q)(Q-r)}}, \tag{R10}$$

where $v_r = \frac{dr}{dt} = v_{orb}\cos\gamma$.

If the probability ratio of being on a (nearly) circularized orbit to that of being on a partially circularized orbit is fixed, we have $\sum_i \propto n_{cir} \propto N \propto N_{cir}$ and $r_{collision} \propto N^2 \propto N_{cir}^2$. Hence, as is verified in Fig.R1, the collision rate between partially circularized planetesimals and circularized planetesimals can be fitted to the relation (assuming a fixed orbit distribution):

$$r_{collision} = AN_{cir}^2\,\mathrm{Myr}^{-1}, \tag{R11}$$

with A a fitting constant. Assuming all collisions are catastrophic (see below for a justification of this assumption), a constant rate of replenishment for circularized planetesimals r_{rep}, and neglecting the potential variations of Eq.R11 due to collisions, the number of circularized planetesimals can be approximated as:

$$\begin{aligned} \frac{dN_{cir}}{dt} &= r_{rep} - \frac{AN_{cir}^2}{\mathrm{Myr}}, \\ N_{cir}(t) &= \sqrt{\frac{r_{rep}}{A}}\tanh\left(\sqrt{Ar_{rep}}\frac{t}{\mathrm{Myr}}\right), \end{aligned} \tag{R12}$$

which converges to $\sqrt{\frac{r_{rep}}{2A}}$ at $t \gtrsim \frac{1}{\sqrt{2Ar_{rep}}}$. We estimate A numerically, finding out that $A \sim 0.0002\,\mathrm{Myr}^{-1}$ (Fig.R1). Assuming a mass reservoir for potentially tidally circularized planetesimals each with $R_p = 100\,\mathrm{km}$ and $\rho_p = 3500\,\mathrm{kg/m^3}$ comparable to the mass of Solar System main asteroid belt, the number of potentially circularized planetesimals is approximately 100. Assuming that these circularized planetesimals arrive at a constant rate within 1 Gyr such that $r_{rep} = 0.1\,\mathrm{Myr}^{-1}$, the number of circularized planetesimals converge to 15 at $t \gtrsim 150\,\mathrm{Myr}$, where 1 collision occurs every 20 Myr on average, indicating a low probability of observing collisions.

Similarly, one can estimate the collision rate among partially circularized planetesimals by accounting for orbital crossing probability at r ($P \sim \frac{\Sigma\sigma}{4\pi r^2}$) as:

$$r_{collision} \sim \sum_i \int_{q_i}^{Q_i} n_i \sigma_i^2 v_i \sum_{i \neq j} n_j dr, \tag{R13}$$

where the effective number density n is 0 for $r \leq q$ or $r \geq Q$ and otherwise given by:

$$n(r) = \frac{w(r)}{4\pi r^2 dr} = \frac{1}{4\pi^2 ra\sqrt{(r-q)(Q-r)}}. \tag{R14}$$

We find out that the collision rate among partially circularized planetesimals is much smaller than their counterpart between circularized and partially circularized planetesimals. This is expected as the partially circularized planetesimals are much more dispersed in space and orbital crossings have stricter constraint on the orientations of orbits.

Collisional outcomes are investigated in Stewart & Leinhardt, 2009; Leinhardt & Stewart, 2012; Kenyon & Bromley, 2017; Löhne et al., 2017. We summarize the scenarios relevant to this study below:

- dust production (mass ejection),
- merge/accretion
- triggering of volcanism (weakening stress, providing heat),
- remove close-in planetesimals (catastrophic collisions).

We apply the model and the free parameters in Kenyon & Bromley, 2017 and Löhne et al., 2017, where the specific impact energy Q_c and the specific binding energy Q_B are given by:

$$Q_C = \frac{1}{2}\frac{M_i M_j}{(M_i + M_j)^2} v_{ij}^2, \tag{R15}$$

$$Q_B = 500\,\mathrm{J/kg}\left[\left(\frac{s_{ij}}{\mathrm{m}}\right)^{-0.37} + \left(\frac{s_{ij}}{\mathrm{km}}\right)^{1.38}\right]\left(\frac{v_{ij}}{3\,\mathrm{km/s}}\right)^{0.5} + \frac{3G(M_i + M_j)}{5s_{ij}}, \tag{R16}$$

where $s_{ij} = \left(R_i^3 + R_j^3\right)^{\frac{1}{3}}$. The mass escaping from the colliding planetesimals can be estimated via:

$$M_{esc} = \frac{1}{2}\left(M_i + M_j\right)\frac{Q_C}{Q_B}. \tag{R17}$$

Catastrophic collisions are defined as $\frac{Q_C}{Q_B} \geq 1$ (Leinhardt & Stewart, 2012). We compute $\frac{Q_C}{Q_B}$ numerically, finding out that collisions among partially circularized and circularized planetesimals are predominantly catastrophic. The dominance of catastrophic outcomes is expected due to the high local keplerian speed of circularized planetesimals ($\sim 100\,\mathrm{km/s}$) and hence the impact speed/energy. Non-catastrophic collisions require that the partially circularized planetesimals to be small ($R_p \lesssim 10\,\mathrm{km}$ for a target circularized planetesimal with radius $R_p \sim 100\,\mathrm{km}$), whose orbital evolution is usually dominated by gravitational instability instead of tidal evolution.

S Dynamical tide

Under the assumption that dynamical tidal theory applied to gas giants/stars equivalently applies to rocky planetesimals, for the dominant mode of (non-chaotic) dynamical tide, the quadrupole fundamental mode ($l = 2$ f-mode), the orbital energy damped in forced oscillations excited during each pericentre cross can be approximated as (Press & Teukolsky, 1977; Moe & Kratter, 2018; Rozner et al., 2022; Glanz et al., 2022):

$$\Delta E = f_{dyn}\frac{G(M_p + M_*)M_*^2}{M_p}R_p^8 q^{-9}, \tag{S1}$$

where f_{dyn} is a constant quantifying the dissipation efficiency (unconstrained despite using the assumption that tidal dissipation under dynamical tide is usually more efficient than its counterpart under equilibrium tide). The corresponding tidal power is:

$$\frac{dE}{dt} = \frac{\Delta E}{\tau} = \frac{n}{2\pi}\Delta E. \tag{S2}$$

Expanding Eq.S2 at highly eccentric orbit, where dynamical tidal evolution is usually relevant (if triggered) we have:

$$\frac{dE_t}{dt}(e \to 1) \approx 0.45 f_{dyn} G^{1.5} M_*^{3.5} M_p^{-1} R_p^8 q_0^{-9} Q_0^{-1.5}, \tag{S3}$$

which has a steeper dependence on q_0 compared to Eq.A1.

The corresponding semi-major axis evolution is:

$$\frac{da}{dt} = \frac{a}{E}\frac{dE}{dt} = -\frac{na^2}{\pi}\frac{\Delta E}{GM_p M_*}, \tag{S4}$$

with the eccentricity evolution constrained by conservation of orbital angular momentum ($\frac{de}{dt} = \frac{(1-e^2)}{2ae}\frac{da}{dt}$).

We then consider the point where the transition from dynamical to equilibrium tidal evolution occurs. Rozner et al., 2022 and Glanz et al., 2022, despite using the criteria that the transition between dynamical and equilibrium tide happens at the eccentricity where the ratio $\frac{\dot{a}_{dynamical}}{\dot{a}_{equilibrium}} \equiv \beta = 1$, also introduce an artificial cut-off at e_{cut} at the minimum of β to avoid the divergence of dynamical tidal evolution towards circularization, with β given by:

$$\begin{aligned} \beta &= \frac{R_p^3}{7\pi G M_p}\frac{f_{dyn}}{K_p} n \frac{(1-e^2)^{\frac{15}{2}}}{e^2(1-e)^9 F(e)}, \\ F(e) &= \frac{1 + \frac{45}{14}e^2 + 8e^4 + \frac{685}{224}e^6 + \frac{255}{448}e^8 + \frac{25}{1792}e^{10}}{1 + 3e^2 + \frac{3}{8}e^4}, \end{aligned} \tag{S5}$$

where we assume pseudo-synchronization and spin-orbit alignment.

β can be further split into physical property part and orbital parameter part as:

$$\begin{aligned} \beta &= \tilde{T}_p \tilde{F}(e|q_0, Q_0), \\ \tilde{T}_p &= \frac{R_p^3\sqrt{GM_*}}{7\pi G M_p}\frac{f_{dyn}}{K_p}, \\ \tilde{F}(e|q_0, Q_0) &= \left(\frac{2q_0 Q_0}{q_0 + Q_0}\right)^{-\frac{3}{2}} \frac{(1+e)^9}{e^2 F(e)}, \end{aligned} \tag{S6}$$

where the minimum of $\tilde{F}(e|q_0, Q_0)$ is at $e \approx 0.34$ (note that this is a mathematical cut-off instead of a physical cut-off; see Moe & Kratter, 2018 for a different cutoff $e_{cut} \sim 0.8$).

References

Abrahams, J. N. H., & Nimmo, F. 2019, Geophys. Res. Lett., 46, 5055, doi: 10.1029/2019GL082542

Beaugé, C., & Nesvorný, D. 2012, ApJ, 751, 119, doi: 10.1088/0004-637X/751/2/119

Bercovici, D., & Michaut, C. 2010, Geophysical Journal International, 182, 843, doi: 10.1111/j.1365-246X.2010.04674.x

Bolmont, E., Raymond, S. N., & Leconte, J. 2011, A&A, 535, A94, doi: 10.1051/0004-6361/201117734

Bouhifd, M. A., Andrault, D., Fiquet, G., & Richet, P. 1996, Geophys. Res. Lett., 23, 1143, doi: 10.1029/96GL01118

Byerlee, J. D. 1978, pure and applied geophysics, 116, 615. https://api.semanticscholar.org/CorpusID:128666327

Childs, A. C., Martin, R. G., Nixon, C. J., et al. 2024, ApJ, 962, 77, doi: 10.3847/1538-4357/ad1a11

Clausen, N., & Tilgner, A. 2015, A&A, 584, A60, doi: 10.1051/0004-6361/201526082

Fukuyama, H. 1985, Earth and Planetary Science Letters, 73, 407, doi: 10.1016/0012-821X(85)90088-3

Geller, L. 1972, International Journal of Rock Mechanics and Mining Sciences & Geomechanics Abstracts, 9, 213, doi: https://doi.org/10.1016/0148-9062(72)90024-1

Gercek, H. 2007, International Journal of Rock Mechanics and Mining Sciences, 44, 1, doi: https://doi.org/10.1016/j.ijrmms.2006.04.011

Gillet, P., Richet, P., Guyot, F., & Fiquet, G. 1991, Journal of Geophysical Research, 961, 11805, doi: 10.1029/91JB00680

Glanz, H., Rozner, M., Perets, H. B., & Grishin, E. 2022, ApJ, 931, 11, doi: 10.3847/1538-4357/ac6807

Gonnermann, H. M., & Manga, M. 2013, Dynamics of magma ascent in the volcanic conduit (Cambridge University Press), 55–84

Gouriet, K., Carrez, P., & Cordier, P. 2019, Minerals, 9, doi: 10.3390/min9120787

Hansen, B. M. S. 2012, ApJ, 757, 6, doi: 10.1088/0004-637X/757/1/6

Heller, R., Leconte, J., & Barnes, R. 2011, A&A, 528, A27, doi: 10.1051/0004-6361/201015809

Hut, P. 1981, A&A, 99, 126

Johansen, A., Ronnet, T., Schiller, M., Deng, Z., & Bizzarro, M. 2023, A&A, 671, A74, doi: 10.1051/0004-6361/202142141

Kenyon, S. J., & Bromley, B. C. 2017, ApJ, 844, 116, doi: 10.3847/1538-4357/aa7b85

Koyaguchi, T. 2005, Journal of Volcanology and Geothermal Research, 143, 29, doi: https://doi.org/10.1016/j.jvolgeores.2004.09.009

La Spina, G., Arzilli, F., Burton, M., Polacci, M., & Clarke, A. 2022, Communications Earth & Environment, doi: 10.1038/s43247-022-00479-6

Lebrun, T., Massol, H., Chassefiere, E., et al. 2013, in EGU General Assembly Conference Abstracts, EGU General Assembly Conference Abstracts, EGU2013–4653

Leconte, J., Chabrier, G., Baraffe, I., & Levrard, B. 2010, A&A, 516, A64, doi: 10.1051/0004-6361/201014337

Leinhardt, Z. M., & Stewart, S. T. 2012, ApJ, 745, 79, doi: 10.1088/0004-637X/745/1/79

Lesher, C. E., & Spera, F. J. 2015, in The Encyclopedia of Volcanoes (Second Edition), second edition edn., ed. H. Sigurdsson (Amsterdam: Academic Press), 113–141, doi: https://doi.org/10.1016/B978-0-12-385938-9.00005-5

Levrard, B., Correia, A. C. M., Chabrier, G., et al. 2007, A&A, 462, L5, doi: 10.1051/0004-6361:20066487

Li, Y., Bonsor, A., Shorttle, O., & Rogers, L. K. 2025, Monthly Notices of the Royal Astronomical Society, 537, 2214, doi: 10.1093/mnras/staf182

Löhne, T., Krivov, A. V., Kirchschlager, F., Sende, J. A., & Wolf, S. 2017, A&A, 605, A7, doi: 10.1051/0004-6361/201630297

Lu, T., Rein, H., Tamayo, D., et al. 2023, ApJ, 948, 41, doi: 10.3847/1538-4357/acc06d

Matsumura, S., Peale, S. J., & Rasio, F. A. 2010, ApJ, 725, 1995, doi: 10.1088/0004-637X/725/2/1995

Miao, S., Li, H., & Chen, G. 2014, Journal of Thermal Analysis and Calorimetry, 115, 1057, doi: 10.1007/s10973-013-3427-2

Moe, M., & Kratter, K. M. 2018, ApJ, 854, 44, doi: 10.3847/1538-4357/aaa6d2

Pál, A., & Kocsis, B. 2008, MNRAS, 389, 191, doi: 10.1111/j.1365-2966.2008.13512.x

Pohl, L., & Britt, D. T. 2020, Meteoritics & Planetary Science, 55, 962, doi: https://doi.org/10.1111/maps.13449

Press, W. H., & Teukolsky, S. A. 1977, ApJ, 213, 183, doi: 10.1086/155143

Reese, C. C., Solomatov, V. S., & Baumgardner, J. R. 2005, Physics of the Earth and Planetary Interiors, 149, 361, doi: 10.1016/j.pepi.2004.11.004

Reese, C. C., Solomatov, V. S., Baumgardner, J. R., & Yang, W. S. 1999, Physics of the Earth and Planetary Interiors, 116, 1, doi: 10.1016/S0031-9201(99)00115-6

Rein, H., & Liu, S. F. 2012, A&A, 537, A128, doi: 10.1051/0004-6361/201118085

Rozner, M., Glanz, H., Perets, H. B., & Grishin, E. 2022, ApJ, 931, 10, doi: 10.3847/1538-4357/ac6808

Scheinberg, A., Fu, R. R., Elkins-Tanton, L. T., & Weiss, B. P. 2015, in Asteroids IV, ed. P. Michel, F. E. DeMeo, & W. F. Bottke (University of Arizona Press), 533–552, doi: 10.2458/azu_uapress_9780816532131-ch028

Seligman, D. Z., Feinstein, A. D., Lai, D., et al. 2024, ApJ, 961, 22, doi: 10.3847/1538-4357/ad0b82

Shestakova, L. I., & Serebryanskiy, A. V. 2023, Monthly Notices of the Royal Astronomical Society, 524, 4506, doi: 10.1093/mnras/stad2006

Slyuta, E. N. 2017, Solar System Research, 51, 64, doi: 10.1134/S0038094617010051

Solomatov, V. 2007, in Treatise on Geophysics, ed. G. Schubert (Amsterdam: Elsevier), 91–119, doi: https://doi.org/10.1016/B978-044452748-6.00141-3

Stewart, S. T., & Leinhardt, Z. M. 2009, ApJ, 691, L133, doi: 10.1088/0004-637X/691/2/L133

Tambovtseva, L., & Shestakova, L. 1999, Planetary and Space Science, 47, 319, doi: https://doi.org/10.1016/S0032-0633(98)00143-3

Tanbakouei, S., Trigo-Rodríguez, J. M., Sort, J., et al. 2019, A&A, 629, A119, doi: 10.1051/0004-6361/201935380

Tang, X., Xu, J., Zhang, Y., et al. 2023, Engineering Geology, 321, 107154, doi: https://doi.org/10.1016/j.enggeo.2023.107154

Turcotte, D., & Schubert, G. 2014, Faulting (Cambridge University Press), 386–424

Vanderburg, A., Johnson, J. A., Rappaport, S., et al. 2015, Nature, 526, 546, doi: 10.1038/nature15527

Wilson, L., Sparks, R. S. J., & Walker, G. P. L. 1980, Geophysical Journal, 63, 117, doi: 10.1111/j.1365-246X.1980.tb02613.x

Woods, A. W., & Bower, S. M. 1995, Earth and Planetary Science Letters, 131, 189, doi: https://doi.org/10.1016/0012-821X(95)00012-2

Wyatt, S. P., & Whipple, F. L. 1950, ApJ, 111, 134, doi: 10.1086/145244

Xu, S., Jura, M., Dufour, P., & Zuckerman, B. 2016, ApJ, 816, L22, doi: 10.3847/2041-8205/816/2/L22

Yahalom, A. 2022, Symmetry, 15, 39, doi: 10.3390/sym15010039

Zahnle, K. J., Lupu, R., Dobrovolskis, A., & Sleep, N. H. 2015, Earth and Planetary Science Letters, 427, 74, doi: 10.1016/j.epsl.2015.06.058